Exploiting Ultrasound Harmonics

The financial support for the printing of this thesis was kindly provided by

©2010 by G. Matte, except for the following chapters
Chapter 2, 4, 6, 11 : ©2008, 2009, 2010 Elsevier B.V.
Chapter 5, 7, 12 : ©2008, 2010, 2007 IEEE
Chapter 10 : ©2010, Acoustical society of America

All rights reserved. No part of this publication may be reproduced, stored in a retrieval system, or transmitted, in any form, or by any means, electronic, mechanical, photocopying, recording, or otherwise, without the prior consent from the author.

Printed in the Netherlands by Optima Grafische Communicatie, Rotterdam.
ISBN 978-90-8559-140-5

Exploiting Ultrasound Harmonics

Ultrageluid harmonischen maximaal benut

Proefschrift

ter verkrijging van de graad van doctor aan de
Erasmus Universiteit Rotterdam
op gezag van de
rector magnificus

Prof.dr. H.G. Schmidt

en volgens besluit van het College voor Promoties.

De openbare verdediging zal plaatsvinden op
donderdag 25 november 2010 om 9.30 door

Guillaume Matthieu Matte
geboren te Martigues, Frankrijk

Promotiecommissie

Promotoren:	Prof.dr.ir. N. de Jong Prof.dr.ir. A.F.W. van der Steen
Overige Leden:	Prof.dr. D.J.G.M. Duncker Dr.ir. M.D. Verweij Dr.ir. A. Bouakaz

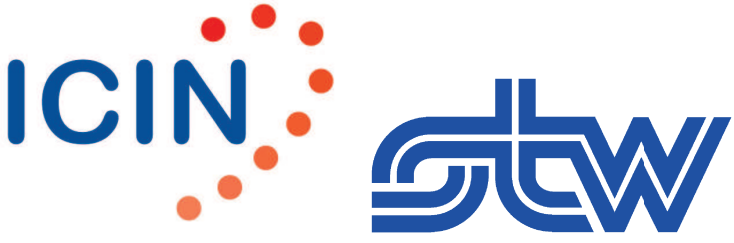

The research described in this thesis was financially supported by :

- The Interuniversity Cardiology Institute of the Netherlands, an institute of the Royal Dutch Academia of Sciences
- the Dutch Technology Foundation (STW)
- the Dutch National Computing Facilities Foundation (NCF)

It was carried out at the department of Biomedical Engineering of the Erasmus Medical Center in Rotterdam, the Netherlands.

Contents

Part 1 : General introduction

CHAPTER 1

Introduction to ultrasound imaging

1.1 General principles of imaging

An image is a visual representation of a physical phenomenon. There are several steps in building an image. The first step is the quantification of the level of every point constituting an image. This quantification is translated into a certain intensity, shade of colors or both. In the case of passive imaging, the object to image is active and produces a signal that can be caught by an appropriate sensor.
An active imaging system involves a primary source that "illuminates"an object of interest and a sensor that converts the scattered signal to built an image. The resolution is the ability of a system to resolve or distinguish punctual objects next to each other. The smallest distance between those two punctual objects that a system can distinguish gives the best resolution that this system can provide. This is why, the resolution of any imaging system is defined by its point spread function (PSF). The PSF corresponds to the response of the imaging system to a point scatterer. In ultrasonic imaging the point spread function depends mostly on the transducer aperture and the frequency. The point spread function has a fundamental influence on the image quality. Another more general example is depicted figure 1.1 where the original photography is degraded by a simulated PSF.

Here is a list of some of the most commonly-used imaging systems which all have specific applications.

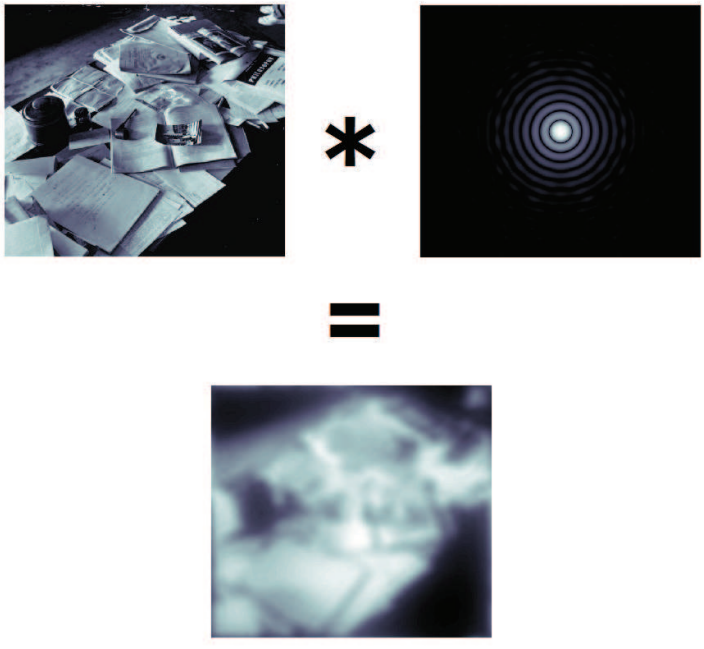

Figure 1.1: Influence of a PSF on a photography of a famous character's desk

The eye is a light-sensitive sensor. It will convert light from reflecting objects, and moderately bright objects into electrical signals that the brain can process. Degradation of the eye leads to common visual impairments. If the focus of the eye is misplaced, it can lead to trouble such as to myopia, hyperopia. In those cases, the point spread function at the focal point is larger than expected, and vision is blurred.

The telescope is a passive system able to receive electromagnetic waves from objects far away. A multitude of telescopes exist, for a broad spectrum of wavelengths, which enable studies of a great diversity of stellar objects in the universe.

The electron microscope uses electrons as the primary source. They are extracted by several means from metals and accelerated to the target object to image.

Magnetic Resonance Imaging (MRI) systems use the magnetic waves emitted from nucleus relaxation. The induced current is measured using coils, which are the sensor of this type of imaging system. A strong magnetic field orientates the spin of all nuclei, and when this field is shut down, magnetic wave are emitted from the

nucleus relaxation. MRI is an imaging technique widely used for medical applications.

This thesis focuses on one particular kind of imaging : Medical Ultrasound Imaging. In medical ultrasound imaging, the PSF depends on the dimensions and topology of the transmitting probe and the frequency of the generated pulse. An example of ultrasonic PSF produced by a phased array transducer is simulated figure 1.2.

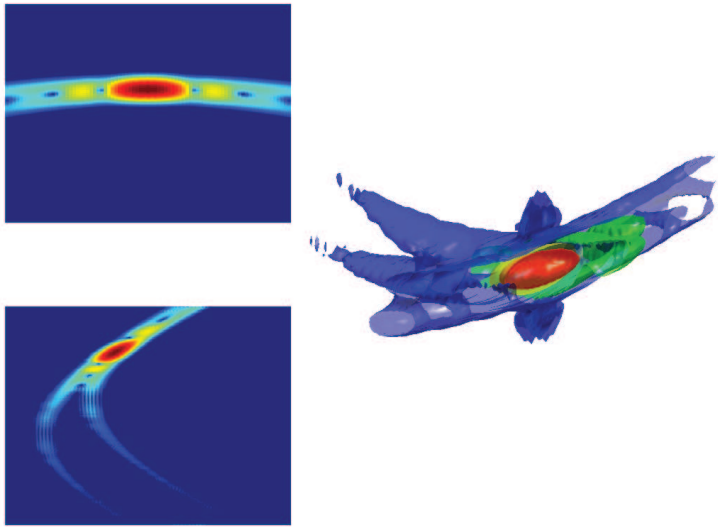

Figure 1.2: lateral, elevation and 3D ultrasonic PSF

1.2 Ultrasound imaging

1.2.1 Sensors

The sensor used to convert sound into electrical signal and inversely is a transducer. The most common transducers are used the audio range. Microphones and loud speakers are the most common transducers. On a wide frequency range, moving coil technology is used for sound transmission and recording in air. Electrostatic transducers are also widely used in air up to 100 kHz for detection and positioning. Electrostatic transducers are also used for medical applications since few years with the apparition of cMUT's [Mills, 2004, Zhou et al., 2005]. There are many types of transducers : electrostatic, variable reluctance, moving coils, magnetostrictive, electrostrictive and piezoelectric transducers. Transducer development was initiated as far back as 180 years ago, when Joseph

Henry, who had already used electromechanical and magneto-mechanical transducers, introduced electro-acoustic transducers for telegraphy.

The most commonly used technology in manufacturing ultrasound medical imaging transducers is based on piezoelectric ceramics. This material was initially used in underwater ultrasound and their development benefited from wars of the past century. The first piezoelectric transducers were made out of quartz crystal by Langevin in 1917 for underwater application, almost forty years after the discovery of piezoelectricity by Pierre and Jacques Curie [Curie and Curie, 1881]. Piezoelectricity occurs only in crystal structures and exhibits a linear relationship between the electric field and the mechanical strain, at low amplitude. The so called electrostrictive materials, however, do not behave as linearly as piezoelectric crystals (see Fig 1.3).

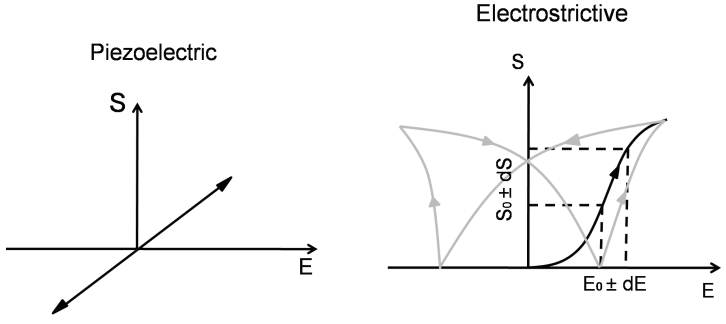

Figure 1.3: strain vs. electric field for piezoelectric and electrostrictive materials. $E_0 \pm dE$ represents range of voltage amplitude used in medical applications

The problem stands in the scarcity of piezoelectric crystal. Despite Quartz and Rochelle salt, the availability of this variety of crystal remains poor. An industrial solution comes from the ability to manufacture electrostrictive ceramics based on various kinds of lead zirconate titanate (PZT) or Barium Titanate ($BaTiO_3$). Manufacturing such ceramics consists in aggregating powders of the above-mentioned components at very high pressure and temperature. To achieve a linear response to an alternating electric drive, those electrostrictive ceramics must be polarized. In this case, a very intense steady electric field aligns the polarization of the microscopic crystals that constitute the ceramic in the same direction. This process is often done at high temperature. When this intense electric field is released, those ceramics have a high coercive force that retain a strong remanent polarization E_0. After this polarization step, these ceramics behave linearly in the range of electric field used in medical applications, and are called piezoelectric ceramics [Sherman and Butler, 2007]. Recently, new techniques were developed to grow PZT crystal from small mono-crystal seed. Those single crystal ceramics present a higher coupling compared to conventional ceramics.

1.2.2 System

Various ultrasound imaging systems have been developed for medical applications depending on the needed penetration depth, size of the region of interest and resolution. Fig 1.4 depicts a simplified block diagram representing a phased array imaging system,

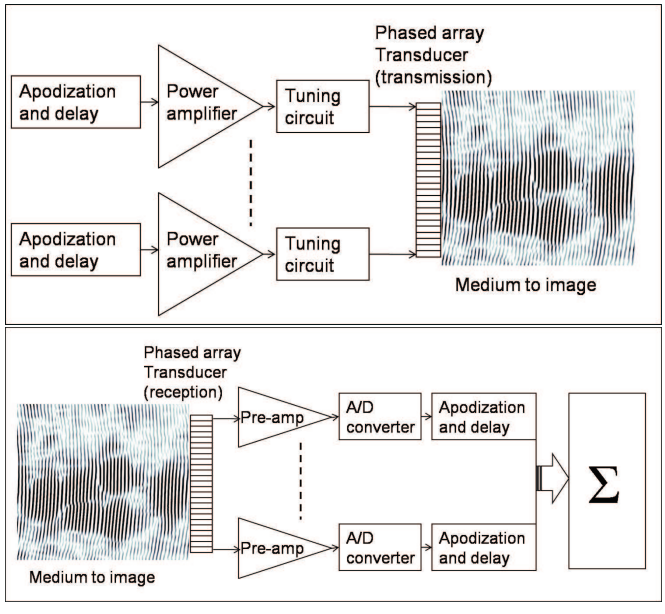

Figure 1.4: Schematic description of the generic simplest system used for ultrasound imaging. Top : transmission, Bottom : reception

which is widely used for cardiovascular imaging. The top part of this diagram represents the transmission part. From left to right, the exciting pulse is electronically delayed in order to focus or steer the transmitting pulse. This initial excitation is then amplified to produce a sufficient level of voltage be applied to the transducer. A tuning circuit adapts the electrical impedance of the output amplifier to the transducer. The propagation of the acoustic wave in the medium is represented in black and white. Most of the systems are used in pulse-echo mode, however for more clarity, the reception is represented in the lower part of figure 1.4. Again, from left to right, the acoustic pressure is converted into an electric signal by the receiving transducers. This signal is pre-amplified in order to achieve sufficient dynamic range before its digitization. The resulting numeric signal is synthetically focused in reception. The last step of this process is not represented on this figure, but is the final goal of the whole chain, and it consist in displaying an image out of the the processed signal.

1.3 Speckle

If the medium to image is constituted of a random distribution of sub-resolution scatterers, the interferences of the scattered waves provoke a granular aspect of the image called speckle. It is an inherent characteristic of coherent imaging. Its texture does not correspond to the underlying structure of the tissue. Like most coherent imaging techniques, medical ultrasound imaging is affected by this phenomenon. An example of speckle in an ultrasound image is depicted on figure 1.5. Because it is the result of interferences,

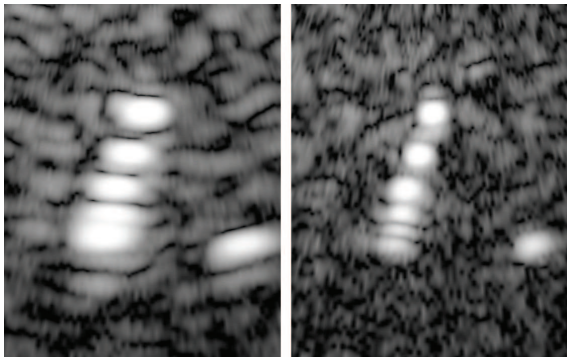

Figure 1.5: Ultrasound image of a tissue mimicking phantom containing wire scatterers. Left : fundamental frequency (1 MHz), Right : second harmonic frequency (2 MHz)

the speckle depends on the frequency of the incident wave. This is why some speckle reduction techniques are based on frequency compounding [Trahey et al., 1986]. On fig 1.5, the frequency dependency of the speckle is clear.

1.4 Contrast agents

Ultrasound contrast agents exhibits various properties that are used to make better images and measurement of great importance regarding diagnosis. For instance measurement of the left ventricle volume or, of blood perfusion in kidneys and capillaries provide valuable information to clinicians. The use of gas-filled microspheres with a shell as contrast agent for medical echography is the result of more than forty years of research. Potential risks were researched, such as the sustainability of the agents and the safety of the patient. This research has lead to the current use of contrast echocardiography with safe contrast agents for the clinic. Several types of gas filled microbubbles exist and are currently used in clinic. Their constitution differs mainly by the composition of their shell, which can be made of phospholipids or polymers.
The detection of ultrasound contrast agents (UCAs) and its discrimination from tissue scattering is based on several approaches. One of the most fundamental aspects of

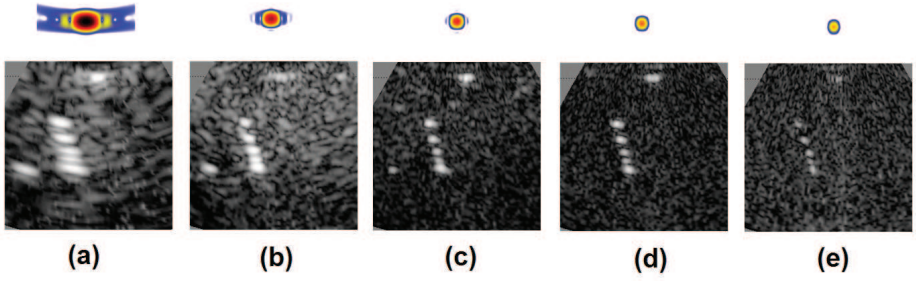

Figure 1.6: Simulated PSF and experimental images of a phantom containing wires. The images were made using the programmable ultrasound system from Lecoeur Electronique and a dual frequency probe developed by Oldelft Ultrasound. (a) fundamental. (b) Second harmonic. (c) Third harmonic. (d) Fourth harmonic. (e) Fifth harmonic

UCAs is their inherent non linear response to acoustic waves in the Megahertz range. The advantage of their non linear behavior was first explored by Shrope and Newhouse [1993]. Soon after the use of second harmonic to enhance contrast signal, several dual pulse schemes were developed to exploit the non linear behavior of microbubbles such as pulse inversion [Simpson et al., 1999, Verbeek et al., 2000] and power modulation [Brock-Fisher et al., 1996]. Those two methods are actually analogous, and they consist in a dual pulse scheme, sent consecutively, so that the sum of the backscattered signal cancels out if the medium is linear. If the entity that scatters back the acoustic pressure distorts the pulse, this cancellation is compromised. Microbubbles exhibiting a stronger non linear behavior than tissue are discriminated by these techniques.
Another approach plays on the high mechanical quality factor of UCAs. Time delay pulse subtraction [Borsboom et al., 2009] uses the advantage of short pulses to detect the extra ringing produced by microbubbles vibrating in the path of the sound pulse. All these phenomena are exploited to provide additional tools for physicians.

1.5 Harmonic imaging

In ultrasound imaging the resolution is given by the frequency and the length of the transmitted sine burst. The length of the transmitted burst defines the axial resolution, and the frequency is directly related to the lateral and elevation resolution. The combination of those resolutions in space and time defines the actual point spread function (PSF) of the imaging system. The higher the frequency, the thinner the beam width. However, the attenuation of sound increases linearly with the frequency in most tissues. In echography, a compromise exists between penetration and resolution. It is on this basis that were developed echographic system until the late nineties. In fact, in the range of acoustic pressure of ultrasound medical imaging, the acoustic wave propagates in a non linear manner. This phenomenon can be interpreted by looking at the pressure wave : the high pressure

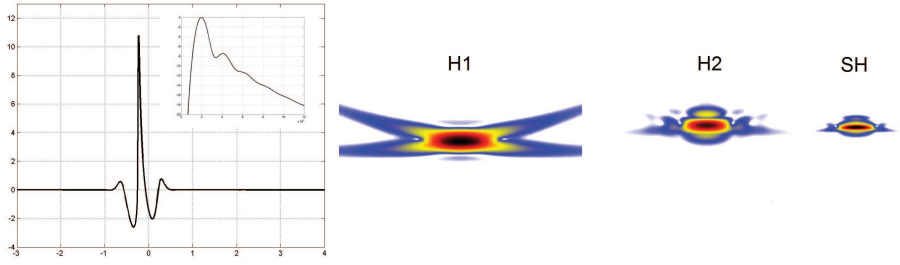

Figure 1.7: Acoustic pulse, associated spectrum and PSF. H1, fundamental, H2 second hamonic, SH superharmonic

part of the wave would travel a little faster than the low pressure part. This phenomenon is analogous to the sea waves in shallow water arriving on the shore. It is possible to better visualize the phenomenon by considering the pressure of the medium at rest as the average water level of the sea (or a sea without waves). Then, a high amplitude wave spreads on this calm sea (or through this medium). After a certain distance, the wave is getting closer to the shore, the bottom of the sea rises, the speed of the crest remains constant, while the trough slows down. An analogous shock appears in the acoustic wave, as it is just before the water wave breaks onto the shore. If this non linear behavior of the acoustic propagation is decomposed in frequency domain, harmonics appear in the spectrum 1.7. The ability to exploit these harmonics entails great perspectives in the improvement of echographic pictures. Harmonic imaging presents the advantage of producing increasingly smaller PSF with the harmonic number fig. 1.6.
Because of their strong non-linear behavior, contrast agents were initially targeted to respond better to second harmonic imaging, rather that fundamental imaging. However, it was demonstrated in 1997 that tissue second harmonic display excellent image quality as soon as the receiving transducer is sensitive enough [Averkiou et al., 1997]. This method opened new possibilities for improving the penetration/resolution compromise. As can be seen on figure 1.7, the higher harmonics that develop after a certain propagation distance from the transducer have an increasingly lower amplitude. It becomes challenging to use individual harmonics above the second to make an image fig. 1.6. The speckle pattern in this tissue phantom can still be distinguished for the third harmonic (fig. 1.6c) but only hard scatterers appear in fourth and fifth harmonic images (fig. 1.6 d and e). The speckle pattern at those frequencies remains bellow the electronic noise floor of the system. For this reason and to go one step further in harmonic imaging, a method was introduced by Bouakaz and de Jong [2003]. Superharmonic imaging consists in integrating the energy present in third to fifth harmonic in order to take full benefit of the available information. The increasingly smaller size of the PSFs with the harmonic number has a direct consequence on the beam width. In transthoracic echocardiography, the transducer is placed on the chest aiming for the heart. The sound beam has to go in between the ribs before reaching the area of interest. Sound reverberation on the ribs can

induce artifacts on the echographic image. Harmonic imaging presents a narrower beam, and the aberration of the main beam have less effect on the final image. Fig 1.7 depicts PSF simulation of a distorted sound pulse in water. The increasingly smaller size of the PSF mirrors great improvement in resolution. Furthermore, if the receiving transducer is equipped with the appropriate frequency band and sensitivity, the superharmonic signal intensity is comparable to the level of the second harmonic beam.

1.6 Outline

This thesis depicts several steps in the development of new ultrasound imaging technique for medical applications. At first, the development of new acoustic measurement methods are described. A technique for indirectly measuring the acoustic pressure based on the acoustic distortion is introduced (chapter 2). Hereafter, an acousto-optic method to measure harmonic beam profiles is detailed (chapter 3), which could be use in combination with the previous method to measure absolute pressure. After these descriptions of acoustic field measurement, a work on transducer characterization is presented. This part is divided in three chapters : the first one is referred to as a basis for transfer function measurement (chapter 4), the second is a comparison between modeling and measurement of the surface vibration of a phased array transducer (chapter 5), and the last one translates the efforts of manufacturing transducers in a practical application of a new phased array transducer for newborns (chapter 6). The third part is dedicated to superharmonic imaging, from the design of the transducer (chapters 7 and 8), to signal processing (chapters 9 and 10). The last part is composed of two studies on ultrasound contrast agents. The goal of the first study on UCAs is to propose a technique to reduce the intensity of the second harmonic beam in tissue, to further enhance contrast-to-tissue ratio. The second study on UCAs focuses on the implementation of threshold behavior of microbubbles for a direct application in clinical settings [Emmer et al., 2007a,c]. The chapter closing this thesis consists in a general discussion and conclusion about the work previously described.

Part 1 : Beam profiles measurements

CHAPTER 2

Estimating acoustic peak pressure generated by ultrasound transducers from harmonic distortion level measurement

Guillaume Matte, Jerome M.G. Borsboom, Paul L.M.J. van Neer, Nico de Jong

Based on: Ultrasound in Medicine and Biology, 2008, 34:1528-1532

Abstract Pressure amplitude measurement is important for general research on ultrasound. Because it requires high accuracy, it is usually done using a hydrophone calibrated by an accredited laboratory. In this paper, a method is proposed for estimating the pressure amplitude in the ultrasound field using an uncalibrated single-element transducer and Khokhlov-Zabolotskaya-Kuznetsov simulations of the ultrasound field. The accuracy of the method is shown to be better than 20% for slightly focused and nonfocused transducers. Extending the method to a pulseecho setup enables pressure measurement of a transducer without the need for an extra transducer or hydrophone.

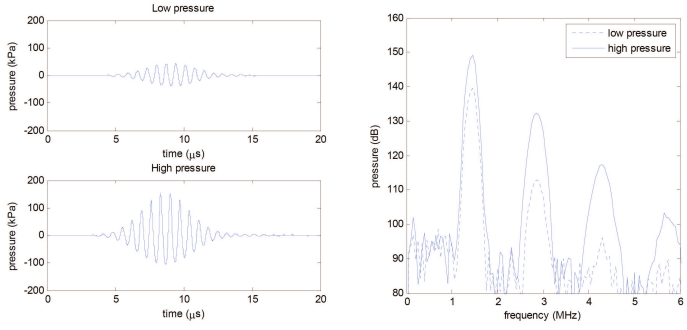

Figure 2.1: Harmonics of an ultrasound wave after propagation of 10 cm in water for two different pressures (transducer diameter 12.7 mm). Left : time trace. Right : corresponding spectra

2.1 Introduction

The pressure amplitude of an ultrasound wave is, together with centre frequency and bandwidth, the most important descriptor of an ultrasound field. The standard method for measuring the pressure amplitude uses a calibrated hydrophone. Several methods can be used to calibrate a hydrophone. The simplest method is to calibrate against an ultrasound field with known amplitude. Although this is a convenient method, it introduces recursion in the problem as the ultrasound field needs to be calibrated first. The recursion problem can be solved by a method that is based on a reciprocity technique [Foldy and Primakoff, 1945] in which the ultrasound field to calibrate against is first self calibrated. Calibration of a hydrophone is an expensive operation which is preferably performed at a special accredited laboratory. In this paper, we propose a calibration method that is based on the observation that the generation of harmonics in a non-linear medium is related to the pressure amplitude of the ultrasound wave. The absolute pressure amplitude at the tip of the uncalibrated hydrophone can be deduced by iteratively matching the measured levels of harmonics with a model of non linear wave propagation. Radulescu et al. [2003] proposed a method in which a calibrated hydrophone for a frequency range $[f_1; f_2]$ can be extended to $[f_1; 2f_2]$ using the second harmonic. His method, however, still requires pre-calibration of the transmitted ultrasound field and directly calculates the absolute level of the second harmonic. This paper starts with the introduction of a harmonic distortion coefficient to describe the relative levels of harmonics in a single number. Subsequently, the procedure used to match the simulated harmonic levels to the measured harmonic levels is described. This procedure enables to estimate the absolute pressure amplitude of the pulse. Finally, the method is validated by comparing the pressure amplitude obtained to direct measurements of the pressure amplitude with a calibrated hydrophone.

2.2 Theory

When a sound wave is propagating in a thermoviscous medium, the compression part of the wave travels faster than the rarefaction part. Although the difference in wave speed is usually small, the effect accumulates over distance and, hence, induces a noticeable distortion of the original wave shape. The distortion is strongly dependent on the pressure amplitude and distance travelled and is, for band limited signals, visible in Fourier domain as additionally generated harmonic components as shown in figure 2.1. Depicted are the pressure-time waveforms and corresponding Fourier transforms of two waves that originally had equal sinusoid wave shape but were scaled to different amplitudes that have propagated over the same distance. The figure shows a strong distortion from the original sinusoid wave shape for the high amplitude wave resulting in high value of the harmonics. The low amplitude wave is less distorted and, consequently, contains lower levels of harmonics. To quantify the amount of distortion of a sinusoid pulse and the progressive formation of a weak shock, the harmonic distortion coefficient (HDC) [Couch, 1997] which relates the total energy in the harmonic components to the energy at the fundamental frequency for a continuous signal shown in (1) has been adapted for pulse signals (2).

$$HDC_{cw} = \sqrt{\frac{\sum_{i=2}^{\infty} H_i^2}{H_1^2}} \tag{2.1}$$

H_i is the amplitude of the i^{th} harmonic component and H_1 is the amplitude of the fundamental. For pulsed waves, the HDC can be calculated by integrating the spectral density over the frequency band of the pulse as shown in (2)

$$HDC_{pulse} = \sqrt{\frac{\sum_{i=2}^{\infty} \int_{\Delta f_i} \mid H_i \mid^2 df}{\int_{\Delta f_i} \mid H_1 \mid^2 df}} \tag{2.2}$$

where $H_i(f)$ and $H_1(f)$ are the spectral densities of the harmonic and fundamental frequency bands and Δf_i the limits of integration for each harmonic component. Equations 1 and 2 both include an infinite number of harmonics in their calculation. However, due to the limited bandwidth of an ultrasound transducer we can ignore any harmonics that lie outside the sensitive bandwidth of the transducer. Therefore in this paper, we will limit our calculations of the HDC to the second harmonic component of the received signal. The KZK (Khokhlov-Zabolotskaya-Kuznetsov) wave equation can be efficiently solved in time domain using finite differences to obtain the resulting ultrasound wave at a certain distance of propagation from a transducer [Lee and Hamilton, 1995]. Subsequently, the HDC can be calculated from the calculated time waveform. Figure 2.2 shows an example of a HDC as function of the pressure for three single element transducers of 5, 10 and 15 mm diameter and a frequency of 5 MHz. Each curve was calculated for a propagation distance, which equaled the Rayleigh distance ($d^2/4\lambda$) of the transmitting transducer. All curves are monotonically increasing which means that a given peak pressure can be

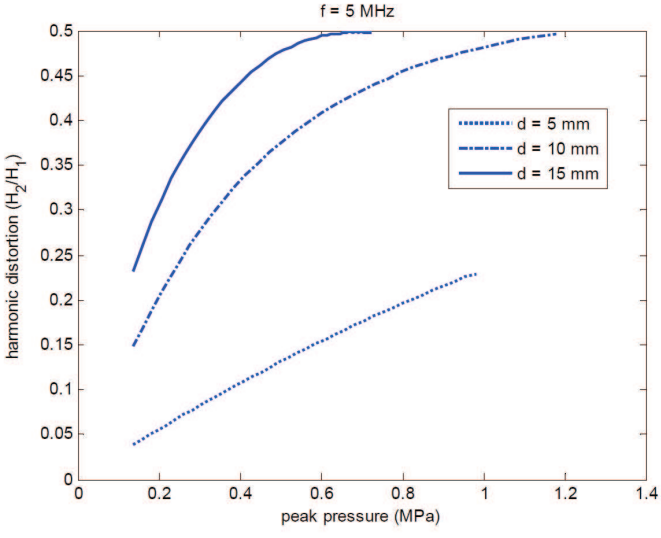

Figure 2.2: Simulated harmonic distorsion $vs.$ pressure peak at 5 MHz calculated at Rayleigh distance (defined as $z_0 = \omega_0 d^2/2c_0$) for different transducer diameters

uniquely mapped into an HDC value and, more importantly, that we can reverse map the HDC to the peak pressure. At high pressure levels, the HDC asymptotically approaches 0.5. That reflects the wave evolution to a saw-tooth shaped wave [Hamilton and Blackstock, 1998]. The inclusion of only the second harmonic in the calculation of the HDC results then in this limit of 0.5. Inclusion of higher order harmonics would increase the range of the HDC.

2.3 Method

We compared axial beam profiles and the corresponding HDCs at different pressures for a commercially available single element ultrasound transducer (Panametrics V306, Panametrics NDT, Waltham, MA, USA). The transducer was mounted in a water tank and excited with a Gaussian apodised 7 cycle burst at 1.5 MHz centre frequency generated by an arbitrary waveform generator (Agilent 33250A, Santa Clara, CA, USA) and amplified by an RF amplifier (AR model 150A100B, Souderton, PA, USA). To suppress any harmonics generated by the amplifier the output was filtered with a 9th order Butterworth low pass filter. The generated acoustic pressure on the axis of the transducer was measured with a calibrated needle hydrophone (Precision Acoustics, Teddington Middlesex,

UK) of which the position was controlled by a computer controlled X-Y-Z system (6K4, Parker Hannifin corporation, Rohnert Park, CA, USA). The KZK equation was solved in time domain using finite differences and was written in Matlab (The Mathworks, Inc., Natick, MA, USA) and C [Lee and Hamilton, 1995]. The non-linearity coefficient and the thermoviscous diffusivity in the model were set to 3.5 and $4.5\ .10^{-6}$ $\mathrm{m}^2.\mathrm{s}^{-3}$, respectively. Finally, the HDCs of the time traces obtained from both the measurements and the simulation program were calculated. The next step was to define an iterative matching algorithm to match a simulated HDC to a measured HDC to obtain an estimate of the pressure amplitude at the measurement position. Inputs to the estimation process were the excitation wave shape, the physical properties of the transmitting transducer such as its diameter and the transmitter-receiver distance as well as the properties of the fluid in which the propagation took place. Subsequently, an initial value for the pressure amplitude at the surface of the transducer was chosen which was input into the simulation program. The program calculated the resulting pressure wave at the measurement position which was transformed into an HDC. This HDC was finally used to update the pressure amplitude at the surface of the transducer for the next iteration step according to eq. 2.3 :

$$p_0(n) = p_0(n-1).\frac{1 + HDC_m - HDC_{kzk}}{HDC_m} \tag{2.3}$$

with HDC_m the measured HDC, HDC_{kzk}, the calculated HDC. The iterations process was stopped when the relative error between the measured HDC and the calculated HDC as shown in eq. 2.3 was less than 1%.

The matching procedure was tested with measurement of the acoustic pressure at 90 mm from a commercially available single element transducer (Panametrics V309) with center frequency 5 MHz and focused at 50.8 mm. According to specifications provided by the manufacturer the effective area of the transducer was 12.7 mm. The transducer was excited with the same setup as described earlier with an excitation frequency of 4 MHz. The pressure at 90 mm was measured with both a calibrated and a non-calibrated hydrophone. The data from the non-calibrated hydrophone was put into the matching procedure to obtain an estimate of the peak pressure at the measurement position. In the pulse-echo method the ultrasound field was determined using the transducer in a pulse-echo configuration, i.e. acting as transmitter and receiver. For this purpose, it is important to include a correction for spatial averaging over the transducer surface when receiving. The pulse-echo measurement was performed with a commercially available unfocused single element transducer (Panametrics V306) with center frequency 2.25 MHz and 12.7 mm diameter. The excitation signal was the same as above but with a center frequency of 1.5 MHz. As a reflector a flat plate was used with a reflection coefficient of 0.6. These measurements were corrected for spatial averaging and the relative transfer function of the transducer and put into the matching algorithm to obtain an estimate for the pressure amplitude.

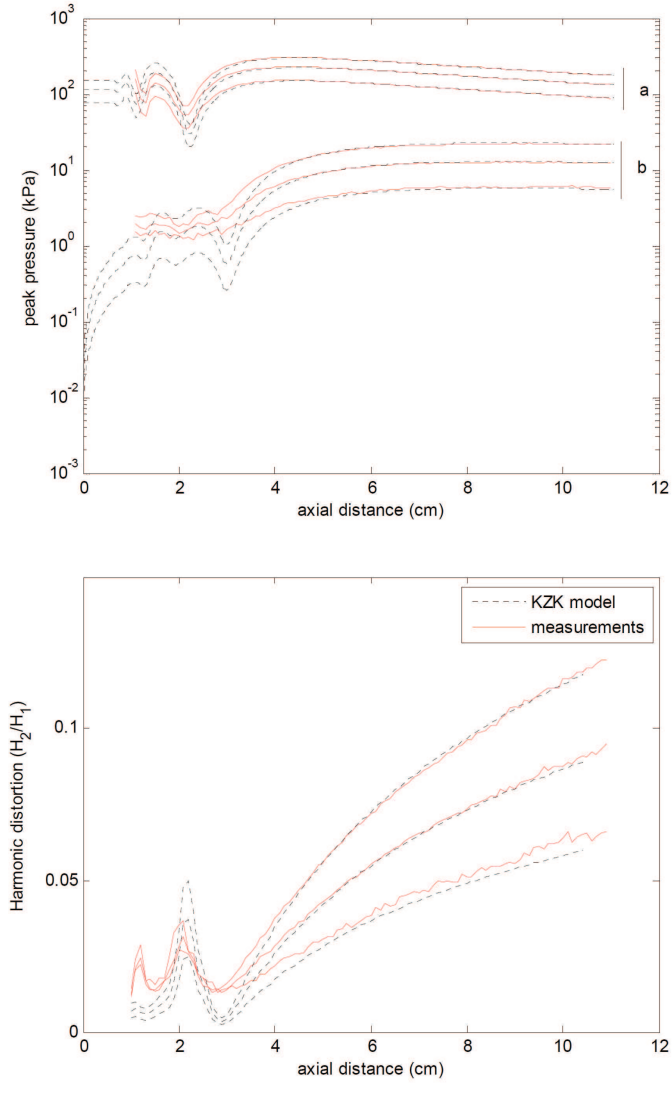

Figure 2.3: Axial beam profiles of an unfocused transducer , f = 1.5 MHz, diameter = 12.7 mm. Top : solid line : measured pressure, dashed line : KZK simulation (a) fundamental peak pressure, (b) second harmonic peak pressure. Bottom : corresponding harmonic distortion over the axial distance.

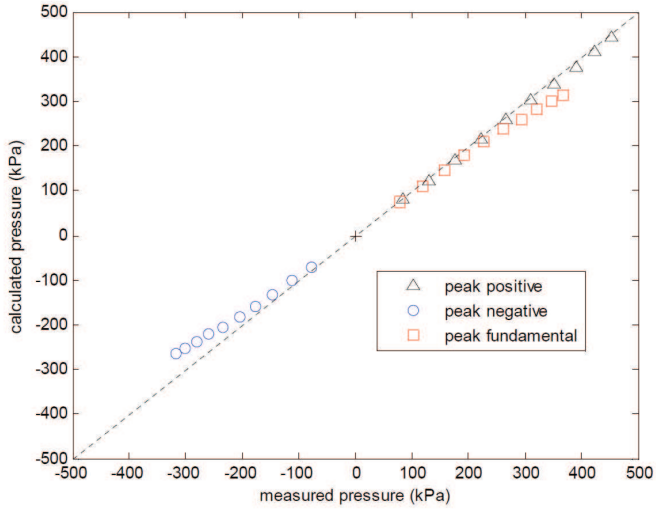

Figure 2.4: Peak pressure estimation from distortion measurement of a focused transducer (f = 4 MHz, receivers diameter = 0.2 mm).

2.4 Results

The measured on axis pressures and the pressures from the simulation model are shown in Fig. 3. The top graph shows the peak pressure of the fundamental (a) and the second harmonic (b) as a function of axial distance for three different excitation pressure levels. The bottom graph shows the corresponding HDCs as a function of distance. In the far field the curves for the measurements and the simulations coincide well for all excitation pressures. In the near field, however, the agreement is less good which may be partly due to the low accuracy of the KZK equation in the near field and to some inaccuracy on the alignment of the hydrophone.

Figure 2.4 shows the agreement between the actual peak pressure as measured by a calibrated hydrophone and the estimated peak pressure from the uncalibrated hydrophone for a range of excitation pressures. Perfect agreement would be indicated by a straight line through the origin. The small deviation occurring at higher pressures might be caused by a small misalignment of the receiver. The difference between measured and calculated pressure remains within 20%, which is about equal to the acurracy of a calibrated hydrophone. Finally, figure 2.5 shows the HDC as a function of distance as obtained by the pulse echo measurement and a simulation. Again, the curves show good agreement.

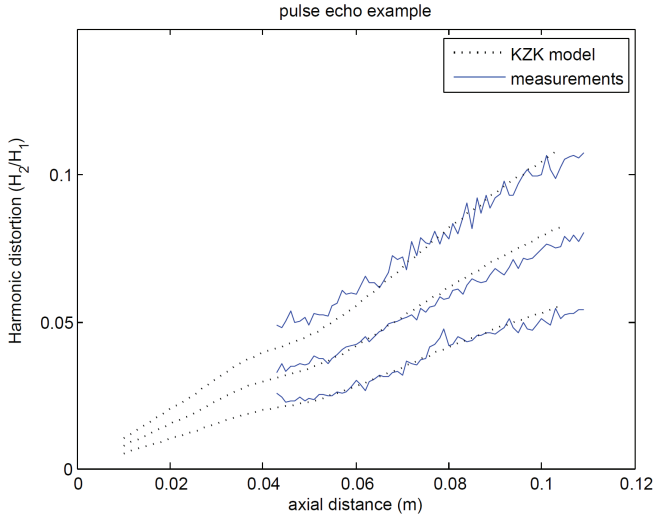

Figure 2.5: Axial measurement of the distortion on a pulse echo setup for an unfocused transducer, f = 1.5 MHz, diameter = 12.7 mm. (peak pressure of 125 kPa)

2.5 Discussion and Conclusion

The method presented in this paper describes pressure amplitude measurements of an ultrasound wave with an uncalibrated hydrophone. We have shown in figure 2.3 that it is possible to accurately simulate the response of a circular single element transducer in the far field when the parameters of the transducer and the measurement position are known. Combining this with figure 2.5, which showed that the relation between peak pressure of an ultrasound wave and the corresponding HDC for a given transducer is unique, we have a means of estimating the peak pressure from a relative measurement of the fundamental and second harmonic. Our method can be extended to a self calibration setup with only one transducer by means of a pulse-echo measurement as was shown in figure 2.5. The procedure will be more elaborate in that case, however, as the received signal must be corrected for the impulse response of the transducer and for spatial averaging over its surface. Limitations of the method are mainly in its use of only the second harmonic. As can be seen in fig. 2.2, the HDC asymptotically approaches 0.5 for high pressures. As said earlier, this is due to the limiting case of a saw tooth shaped wave to which the wave tends due to non-linear propagation. When we use the relation the other way around, i.e. try to estimate the pressure from the HDC, the error in the estimate increases sharply when approaching an HDC of 0.5. This could be improved by including more harmonics in the calculation of the HDC. This, however, is limited by the finite bandwidth of the receiving transducer and the decreasing accuracy of the KZK equation for higher harmonics, but for the range of medical transducers, this technique covers a quite larger range of pressure and frequencies. Another limitation is the dependence on accurate excitation conditions for the KZK simulation, for example the diameter and apodization of the active transducer surface. Because there is no quick way to measure the apodization of the transducer in transmission, any error or wrong assumption on these variables directly reflects on the estimated pressure. These kinds of errors may be an explanation for the deviation of the peak negative pressure in figure 2.4. We have introduced a method for the inexpensive calibration of a hydrophone or transducer. The expected accuracy is around 20% which is comparable to the accuracy of a commercial hydrophone calibration.

2.6 ACKNOWLEDGMENTS

This work was supported by the Dutch technology foundation STW (grant number 7734).

CHAPTER 3

Acousto-optic method to measure harmonic beam profiles

Guillaume Matte, Özgür Kaya, Nico de Jong
Based on the work of Özgür Kaya for his M. Sc's thesis [Kaya et al., 2008].

3.1 Introduction

Several acousto optic methods have been developed in order to measure sound beams and acoustic waves without disrupting the pressure field with an hydrophone. There are two main streams in acousto-optic measurement methods. One is called optical tomography. It is a non invasive and accurate method to measure absolute acoustic pressure distribution with a LASER vibrometer [Harvey and Gachagan, 2006, Wang et al., 2007, Bou Matar et al., 2000]. The second method is known as Schlieren imaging. The use of Schlieren technique is a fast method to visualize projections of the ultrasound beam. Scanning the whole beam using a Schlieren technique is faster than using optical interferometry. The acquisition of the complete beam volume can be achieved using tomography [Pitts et al., 1994, Neumann and Ermert, 2006]. The complete tomography of an ultrasonic beam is still faster than using a laser interferometer, considering that it is possible to acquire complete cross sections of the the beam using Schlieren technique and only a single line using a LASER interferometer. One way to measure harmonics consists in

having a sufficiently high temporal resolution. Neumann and Ermert [2006] described a Schlieren method to visualize sound pulse with a high temporal resolution. Their approach consisted in acquiring snapshots of the pressure distribution using very short light pulses in order to minimize the smearing effect.
This approach requires a pulsed light source able to deliver high light intensity in a short time (5 ns pulse to acquire 5 MHz wave with a blurring effect of 5%). In the process of building transducers for medical imaging, the control of their performances is an important step. In case of designing an manufacturing transducers for harmonic imaging, the control of the generated beam is compulsory, hence our motivation to develop an acousto-optic method to measure harmonic beam profiles.

This chapter is composed by an overview of the theoretical background about acousto-optic interaction. Then, simulation of harmonic Schlieren images will be described. Then, these calculations will be compared with measurements.

3.2 Background

The optical refraction index is defined as the ratio between the speed of electromagnetic wave in vacuum over its speed in the medium of interest. For commonly used media like air, water, the refractive index μ_0 is respectively 1.003 and 1.333. This ratio depends on the density of particle composing a medium. By extension, this ratio depends on the pressure.

The piezo-optic coefficient defines the rate of change of the optical refractive index when the pressure changes. For water [Riley and Klein, 1967]

$$\left(\frac{\partial \mu}{\partial p}\right)_S = 1.51\ 10^{-10} Pa^{-1} \tag{3.1}$$

the S evokes that the measurement is done under adiabatic conditions.

Klein and Cook [1967] described several regimes in acousto-optic interaction and defined the parameters Q and ν as :

$$Q = \frac{k_{us}^2 L}{k_{opt} \mu_0} \tag{3.2}$$

$$\nu = k_{opt} \left(\frac{\partial \mu}{\partial p}\right)_S p\ L \tag{3.3}$$

where k_{us} is the ultrasonic wave number, k_{opt} the optical wave number, p the local pressure and L the interaction length between light and sound. L is usually taken as the ultrasonic beam width [Zanelli and Kadri, 1994, Mc Lennan et al.].

The Raman Nath regime is defined if $Q \ll 1$. This situation correspond to the simplest solution to the differential equation describing the light interaction with the ultrasound beam. In this case, if the light beam encounter the ultrasound beam at normal incidence, the intensity of n^{th} diffraction orders is

$$I_n = J_n^2(\nu) \tag{3.4}$$

In the case that $Q \approx 1$, the solution to the optical wave equation can not include the same approximation, and it is necessary to solve it numerically. Q $\gg$ 1 is the third regime of interaction between light and sound [Klein and Cook, 1967]. In this case, the light intensity is concentrated in only one order according to the angle of incidence of the light beam with the acoustic beam. This regime is analogous the diffraction of light by a Bragg grating. In this study, the setup operated under the Raman-Nath regime.

In the direction of propagation of the acoustic wave, the light wave is diffracted as if it was passing through an optical phase grating. This phase grating is the acoustic wave that locally changes the refractive index of the medium. But the light beam is also diffracted in the direction perpendicular to the propagation of the acoustic wave. This is where Zanelli and Kadri observed the higher diffraction order to deduce the acoustic pressure from light intensity measurements. By integrating the light intensity in those higher diffraction order they measure ν , which is related to the pressure by the formula eq (3.3). In this case, the variation of the refracting index is not directly depending on the sound wavelength, but of the acoustic beam-width. In the expression of ν, the interaction length was considered to be the actual beam width at the focal spot. The acoustic wavelength was not involved in this expression. However, for slighly focused sound beams and considering the interaction length is the direction of propagation of the sound wave, L in equations 3.3 and 3.2 becomes the acoustic wavelength.

3.3 Theory

Simulation of axi symmetric non linear sound pulses were performed by solving numerically the KZK equation [Lee and Hamilton, 1995]. In order to get the actual projection of the pressure distribution measured by the Schlieren system, the pressure field has to be integrated over the path of the light propagation (fig 3.1). Lenses and mirrors were simulated as Fourier operators [Goodman, 2005]. At the focal spot of the focusing optical component, the optical diffraction figure was considered to be the scaled 2D Fourier transform of the ultrasound pulse (fig 3.2). The frequency selection of the ultrasound beam was performed by optical spatial filtering at optical focus [Goodman, 2005]. The use of a slit with the appropriate aperture, instead of the conventionally used knife edge, permitted to select the harmonic to image. A representation of this spatial filtering is given fig 3.2. This figure represents a snapshot of the Schlieren projection of an acoustic pulse and its instantaneous diffraction figure at the location of the spatial filter. With the use of a continuous light source, the sound pulse travels through the light beam and the resulting Schlieren projection represents the integration of the path of the sound pulse over time.

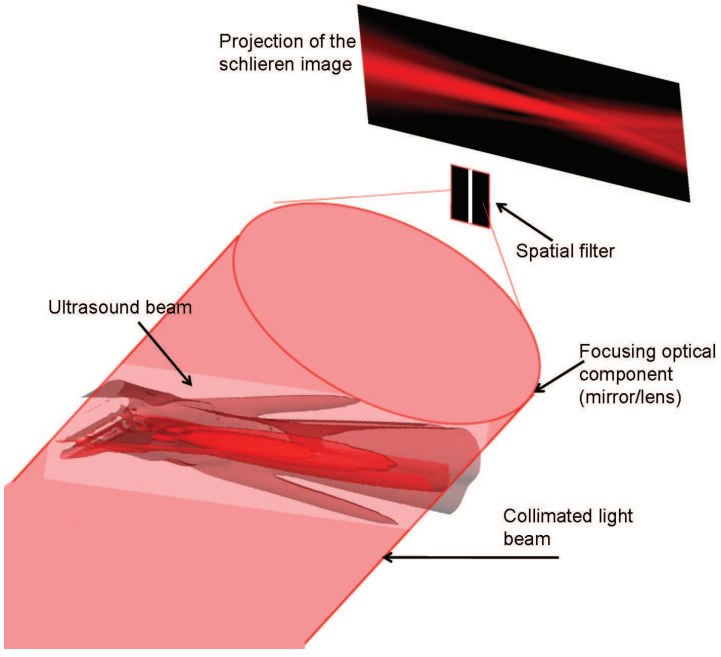

Figure 3.1: Collimated light beam crossing the ultrasound beam (3D artistic view), the focusing optical component and forming the schlieren image after spatial filtering at optical focus

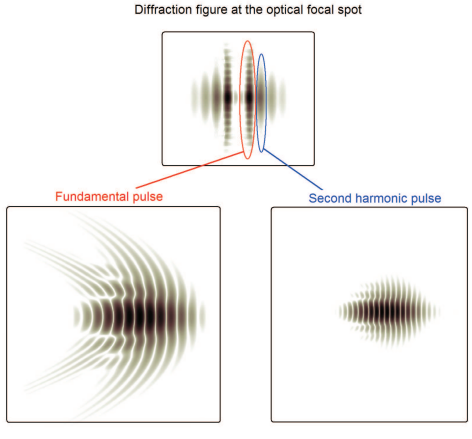

Figure 3.2: Optical diffraction figure at the location of the spatial filter and corresponding acoustic pulse

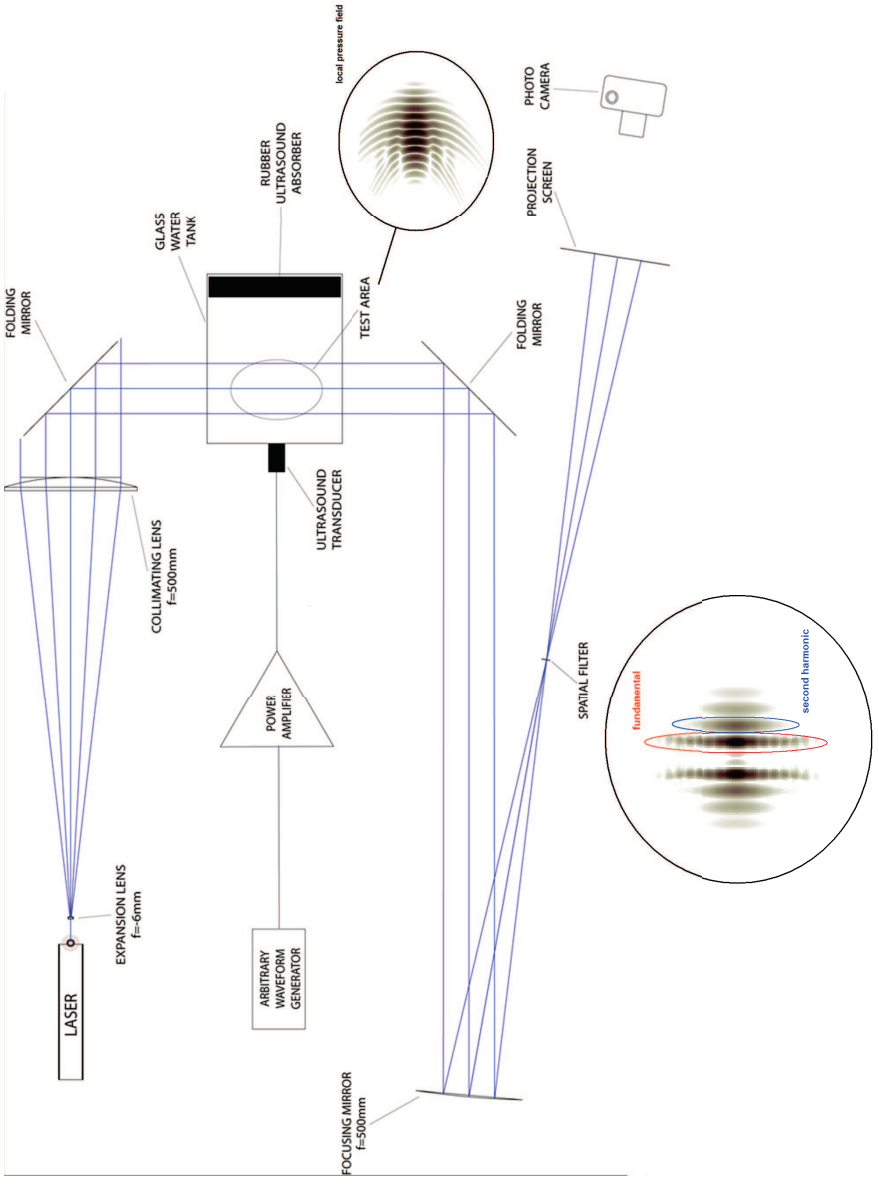

Figure 3.3: Setup

3.4 Materials and Methods

The light source was a He-Ne Laser (λ = 632.8 nm, 5 mW) from Nippon Electric company (NEC). The laser output was expanded to the size of the for collimating lens using an expension lens (f = -6 mm, D =6 mm, LINOS 314001). Two flat front surfaces mirrors were used to fold the optical assembly. In this way, the complete system could fit on a 90x90 cm suspended optical table (Newport).

After passing through the test region, the collimated laser beam is focused on the Fourier plane using a spherical front surface mirror ($f = 500$ mm, $D = 106$ mm) placed off-axis. The angle of the mirror is set as small as possible to prevent significant chromatic aberration which would otherwise complicate the spatial filtering at the focus.

The image was projected on a frosty-glass projection screen, and captured by a D-SLR camera (Nikon D80) mounted on an optical rail for stability. The camera was manually focused using a 50 mm lens. The aperture was set to $f/10$ for a large field of view enabling sharp focus besides long exposure time. A long exposure time of 1 s was used to evade the laser speckle by time averaging. The sensitivity was set to ISO 200 in order to prevent sensor noise and enable long exposure time. The camera was controlled remotely to avoid camera shake and move. For each slit position, the background illumination was also acquired without the presence of the ultrasound wave.

The spatial filter enabled the visualization of ultrasound harmonics separately. An adjustable-width slit attached on a micrometer translation stage was used to select the diffraction order of interest associated with the harmonic profile to visualize. In order to mark the location of the diffraction order associated with the frequency of interest, two transducers where mounted in the system. Those transducers where both focused single-element immersion transducers (Panametrics V309, 2" PTF, 5 MHz and V311, 2" PTF, 10 MHz). The transducers were excited at respectively 5 and 10 MHz. The resulting 5 MHz beam was not visible on the projected image when the slit was positioned at the location of the 10 MHz wave diffraction order. Inversely, the 10 MHz beam did not appear on the screen when the spatial filter was set to the location of the 5 MHz wave diffraction order. Once the locations were marked for several frequencies, the system was configured to measure harmonic beams. Ultrasound was generated using a single-element focused immersion transducer (Panametrics V309, 2" PTF, 5 MHz). The transducer was mounted into a side of a glass water tank placed in the test region of the Schlieren assembly. A rubber absorber was disposed in the water tank at the opposite side of the transducer to prevent reflections. The electric signal was generated by an Arbitrary Waveform Generator (20 MHz) from Agilent Technologies 33220A. This signal was amplified by a RF power amplifier A-500 from Electronic Navigation Industries (ENI) and applied to the transducer. The output voltage of this amplifier for a 5 MHz sinusoidal signal at several input values were measured using an oscilloscope to check the amplification factor and the linearity of the amplifier on this wide amplitude range. The transducer was driven with a sinusoidal burst at the transmit frequency of 5 MHz. Two sets of Schlieren image acquisitions were made for voltage sweeps from

8 V_{PP} to 124 V_{PP} in increments of 4 V_{PP} with 50 and 100 burst cycles per 200 μs. A continuous excitation was avoided to prevent damaging the transducer. In order to compare the pressure values of ultrasound harmonics at various driving voltage levels, a hydrophone system was used to measure the pressure signal at the focus of the transducer as a reference.
The acquired Schlieren images were processed using MATLAB. First step was to subtract the background illuminations from the corresponding Schlieren acquisitions in order to improve the image quality. This procedure removes unwanted features interfering with the beamprofile of the ultrasound wave.

The intensity levels at the focus were measured by taking the average of a small region (lateral: 488.4 μm $\times$ axial: 3255.8 μm) to smooth the effects of background noise.

3.5 Results

The measured beam using a screen projection of the Schlieren image displays a poor image quality and the dynamic range is critical. Theoretically the data acquired by the optical setup can be displayed at most on 24 dB (256 gray levels). However, because of the background noise, this range was reduced to only 20 dB. Measurements of the integrated light intensity were realised for several harmonics by changing the position of the optical slit. By this mean, the integrated light intensity was measured for several power applied on the transducer and for 4 harmonics.

At first, images of harmonic profiles were compared with the simulated harmonic beams (see 3.4). The pressure at which these acquisitions were recorded is indicated above the experimental data. The very near field of the experimental data was intentionally removed by masking it with electric tape (in a triangular shape).

Figure 3.5 corresponds to the integrated power for several applied voltage acquired with 50 cycles transmission burst. It provides quantitative information about this setup. The integrated intensity over the previously defined region of interest was compared with simulations. The power dependent intensity profiles show a clear saturation of the optical setup above a peak negative pressure of 300 kPa. The fundamental beam is affected by this saturation very quickly, and the second harmonic beam which becomes very energetic also saturates the Schlieren acquisition setup. Four harmonics components displayed on figure 3.5 exhibit very similar tendency than the simulation. The fourth harmonic component does not increase with the increasing power, but the poor dynamic range and high noise level can be an explanation to this lack of similarity.
Figure 3.6 compares slices of beam profile sampled from the experimental and theoretical datasets. The dashed lines represent the experiment, and the solid lines the theory. All four harmonics are displayed. This comparison put in evidence two limits of the optical setup. First, the saturation threshold is very difficult to estimate by only looking at the Schlieren image. Secondly, the level of the background noise is very high and limits

consequently the available dynamic range.

3.6 Conclusion and Discussion

Harmonic Schlieren technique may be used to visualize harmonics generated during the propagation of high frequency sound beams. With the explosion of non linear imaging technique during the past years, it becomes interesting to be able to isolate harmonics beams. This optical setup would provide insight for interactions of acoustic waves with complex media or contrast agents. This method in combination with the technique described in the previous chapter can be related to an absolute measurement of the pressure. However the limited dynamic of the acquisition system suggests an adjustment of the setup for each new harmonic measurement.

3.7 Acknoledgments

The authors are grateful to the enthusiasm, insight and help from Gijs van Soest. We also would like to thank Wim van Holland who generously lend us good quality mirrors and lenses from his department. Finally, Geert Springeling and Wim van Alphen for the devoted help they provided with the mechanical aspect of this enterprise.

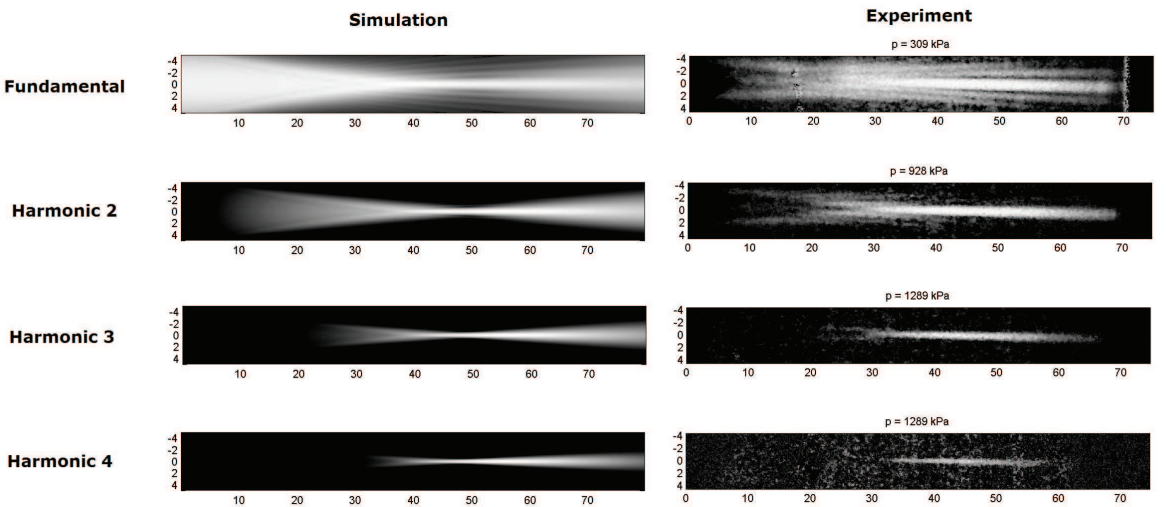

Figure 3.4: Left : schlieren images of harmonic beams simulated by solving numerically the KZK non-linear wave equation. Right : acquisition of ultrasound harmonic beams with the system described on fig.3.3

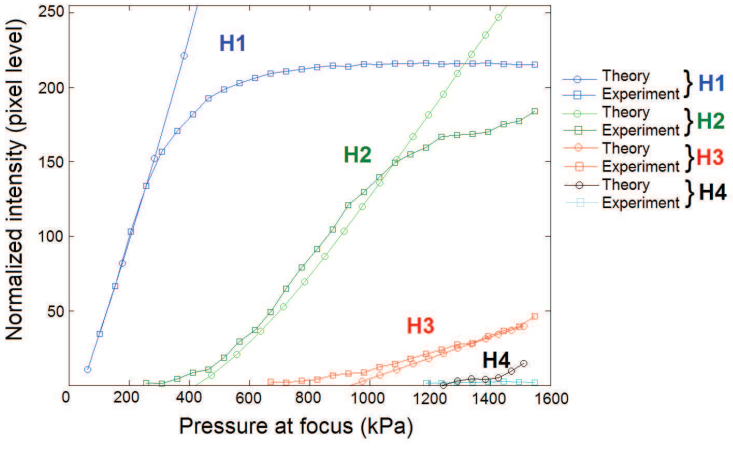

Figure 3.5: pressure dependency of the harmonic components

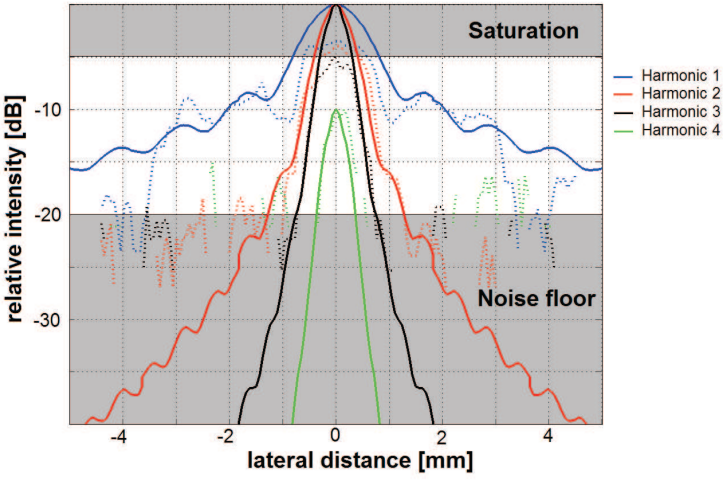

Figure 3.6: beam profile slice of the simulated beam (harmonics 1 to 4)

Part 2 : Transducers for harmonic imaging

CHAPTER 4

Transfer functions of US transducers for harmonic imaging and bubble responses

Paul L.M.J. van Neer, Guillaume Matte, Jeroen Sijl, Jerome M.G. Borsboom, Nico de Jong

Based on: Ultrasonics, 2007, 46:336-340

Abstract Current medical diagnostic echosystems are mostly based on harmonic imaging. This means that a fundamental frequency (e.g. 2 MHz) is transmitted and the reflected and scattered higher harmonics (e.g. 4 and 6 MHz), produced by nonlinear propagation, are recorded. The signal level of these harmonics is usually low and a well-defined transfer function of the receiving transducer is required. Studying the acoustic response of a single contrast bubble, which has an amplitude in the order of a few Pascal, is another area where an optimal receive transfer function is important. We have developed 3 methods to determine the absolute transfer function of a transducer. The first is based on a well-defined wave generated by a calibrated source in the far field. The receiving transducer receives the calibrated wave and from this the transfer functions can be calculated. The second and third methods are based on the reciprocity of the transducer. The second utilizes a calibrated hydrophone to measure the transmitted field. In the third method, a pulse is transmitted by the transducer, which impinges on a reflector and is received again by the same transducer. In both methods the response combined with the transducer impedance and beam profiles enables the calculation of the transfer function. The proposed methods are useful to select the optimal piezoelectric material (PZT, single crystal) for transducers used in reception only, such

as in certain 3D scanning designs and superharmonic imaging, and for selected experiments like single bubble behavior. We tested and compared these methods on two unfocused single element transducers, one commercially available (radius 6.35 mm, center frequency 2.25 MHz) the other custom built (radius 0.75 mm, center frequency 4.3 MHz). The methods were accurate to within 15%.

4.1 Introduction

Harmonic imaging is an established technique used in current medical diagnostic echo systems [Bouakaz and de Jong, 2003]. A fundamental frequency (eg., 2 MHz) is transmitted into the human body and the reflected higher harmonics (eg., 4 and 6 MHz), produced by nonlinear propagation, are recorded. The signal level of these harmonics is low [Bouakaz and de Jong, 2003] and as such the efficiency in both transmission and reception and bandwidth of the transducer are critical. An area where an optimal transfer function in reception is important, is the study involving the acoustic response of single contrast bubbles, which are in the order of a few Pascal.
To assess the performance of a transducer, absolute measurements of its transfer functions are important. The functions of importance are the transmit, receive and pulse-echo transfer functions. In general, to characterize a transducer, the transmit transfer function is measured using a hydrophone. Also pulse-echo measurements are standard. Receive transfer functions are generally not considered. In this article we show that if one of the three transfer functions is measured the other two can be derived, if in addition the impedance of the transducer is measured.
We have adapted and tested three methods to determine absolute transfer functions, which are independent of the circuitry connected to the transducer. In the next section the necessary theory will be established.

4.2 Theory

The transducer transmit efficiency ($S_T(\omega, z)$) is defined by the International Electrotechnical Commission (IEC) as [Labuda et al., 2004]

$$S_T(\omega, z) = \frac{|p(\omega, z)|z}{|I_T(\omega)|}, \tag{4.1}$$

where $p(\omega, z)$ is the acoustical point pressure at an axial distance z of the transducer, ω is the angular frequency and $I_T(\omega)$ is the current through the transducer.
For unfocused transducers a reference transmit efficiency ($S_{ref}(\omega)$) can be defined as the transmit efficiency in the far field, whereas for focused transducers the reference transmit efficiency is defined to be the transmit efficiency at the focal point.

By rewriting expressions reported by Chen et al. [1993] $|p(\omega, z)|$ can be expressed as a function of $|p_0(\omega)|$ at the reference position

$$|p(\omega, z)| = \frac{A_T}{\lambda \cdot z}|p_0(\omega)|, \tag{4.2}$$

where A_T is the transducer surface area, λ the wave length and $|p_0(\omega)|$ the pressure at the transducer surface.

Combining (4.1) and (4.2) yields

$$|p_0(\omega)| = \frac{\lambda}{A_T} S_{ref}(\omega)|I_T(\omega)|. \tag{4.3}$$

The transducer transmit transfer function ($T_t(\omega)$) is defined to be

$$T_t(\omega) = \frac{|p_0(\omega)|}{|V_T(\omega)|}, \tag{4.4}$$

where $V_T(\omega)$ is the voltage over the transducer (see Fig. 4.1).

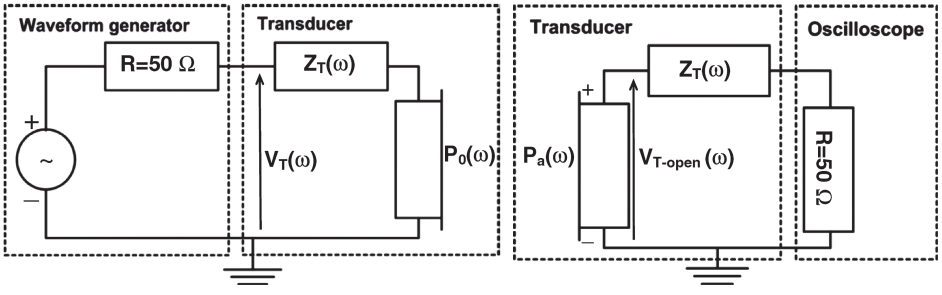

Figure 4.1: The essentials of the transmission and receive circuits are shown schematically on the left and right respectively.

Combining (4.3) and (4.4) produces

$$T_t(\omega) = \frac{1}{|Z_T(\omega)|} \frac{\lambda}{A_T} S_{ref}(\omega), \tag{4.5}$$

where $Z_T(\omega)$ is the complex impedance of the transducer.

The receive transfer function ($T_r(\omega)$) is defined to be similar to the sensitivity in reception ($M_T(\omega)$) as defined by the IEC [Labuda et al., 2004]

$$M_T(\omega) = T_r(\omega) = \frac{|V_{T-open}(\omega)|}{|p_a(\omega)|}, \tag{4.6}$$

where $V_{T-open}(\omega)$ is the open circuit voltage produced by the transducer (see Fig. 4.1) and $p_a(\omega)$ the received pressure averaged across the transducer surface.

Reciprocity

The spherical wave reciprocity parameter J for transducers of arbitrary shape and size is given by Bobber [1966]

$$J(\omega) = \frac{M_T(\omega)}{S_{ref}(\omega)} = \frac{2}{\rho_0 f}, \tag{4.7}$$

where ρ_0 is the ambient density of the medium in which the transducer is inserted and f the frequency.

A relation between $T_t(\omega)$ and $T_r(\omega)$ is obtained by combining (4.5), (4.6) and (4.7)

$$\frac{T_r(\omega)}{T_t(\omega)} = \frac{2|Z_T(\omega)|A_T}{\rho_0 c_0}, \tag{4.8}$$

where c_0 is the small signal acoustic wave speed of the medium in which the transducer is inserted.

4.3 Methods

4.3.1 Experimental setup

The experimental setup consisted of a tank filled with water with the transmitting transducer mounted in the sidewall and the receiving transducer, hydrophone or flat plate mounted in a holder controlled by an xyz-system (see Fig. 4.2).

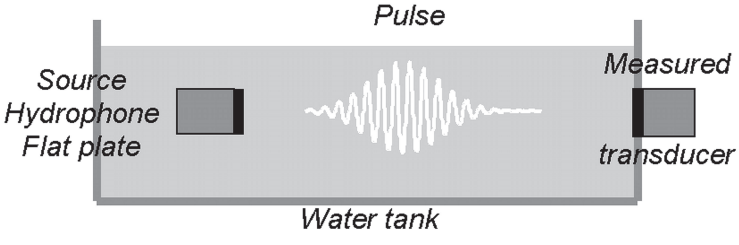

Figure 4.2: Schematic diagram of the experimental setup.

Care was taken to ensure that the transmitter output pressure was of such low magnitude that nonlinear propagation could be neglected. The influence of attenuation was neglected as well, as the propagation distance in water was small, in the order of centimetres. A correction for diffraction is necessary to recalculate the pressure at the transducer surface from a pressure measured some distance away. The exact diffraction correction function posted by Goldstein et al. [1998] is used to correct for the diffraction effects of a transmitting flat, circular piston transducer mounted in an infinite rigid baffle and the spatial averaging effects by a receiving flat circular piston transducer in a coaxial geometry. The expression given by Chen and Schwarz [1994] is used to correct for the diffraction of a flat plate transducer to a flat plate (perfect reflector) and back to the transducer. As a transmission pulse a spike was generally used.

4.3.2 Direct transmit transfer measurement

The transducer is mounted in the sidewall of the tank and used as a source transmitting a known pulse. A hydrophone is mounted in the holder of the xyz-system and measures the transmitted field. The transmit transfer function (T_t) of the transmitting transducer is calculated by

$$T_t = \frac{V_h}{V_T} \cdot \frac{1}{T_h \cdot D_t}, \tag{4.9}$$

where V_h is the Fourier transformed voltage produced by the hydrophone, V_T the Fourier transformed voltage measured over the impedance of the transmitting transducer, T_h the hydrophone transfer function and D_t the diffraction correction function for the transmitting transducer.

4.3.3 Direct receive transfer measurement

A source with known transmit transfer function is mounted in the sidewall of the tank transmitting a known pulse. The transducer is mounted in the holder of an xyz-system and used as a receiver. Its receive transfer function (T_r) is calculated by

$$T_r = \frac{V_{T-open}}{V_T^s} \cdot \frac{1}{T_t^s \cdot D_t^s}, \tag{4.10}$$

where V_{T-open} is the Fourier transformed open circuit voltage produced by the receiving transducer, V_T^s the Fourier transformed voltage measured over the source impedance, T_t^s the transmit transfer function of the source and D_t^s the diffraction correction function for the source.

4.3.4 Pulse-echo

The transducer is mounted in the sidewall of the tank. It transmits a known pulse, which impinges on a thick aluminium plate reflector. The same transducer receives the reflected sound. The transmit and receive transfer functions of said transducer are related by

$$T_t \cdot T_r = \frac{V_{T-open}}{V_T} \cdot \frac{1}{D_{pe} \cdot R_I}, \tag{4.11}$$

where V_{T-open} is the Fourier transformed open circuit voltage produced in reception, V_T the Fourier transformed voltage measured over the transducer impedance in transmission, D_{pe} the diffraction correction function for the transmitting transducer to the flat plate and back and R_I the intensity reflection coefficient, for aluminium $\sqrt{0.84}$.

4.3.5 Equipment

Two transducers were investigated, both were of the unfocused single element type. The first was a commercially available transducer (PZT V306, Panametrics, Waltham, MA,

USA, 2.25 MHz center frequency, diameter 12.7 mm), the other custom built (composite, 4.5 MHz center frequency, diameter 1.5 mm). An arbitrary waveform generator (33250A, Agilent, Loveland, Colorado) is used as a voltage source and connected directly to the transmitting transducer if necessary. The signal received by the transducer under scrutiny or hydrophone is attenuated by an attenuator (355D, Agilent, Santa Clara, CA, USA), amplified by a low noise amplifier (AU-3A-0110-BNC, Miteq, Hauppauge, NY, USA) and digitized by an oscilloscope (9400A, LeCroy, Geneva, Switzerland). Both the waveform generator and oscilloscope are connected to a computer through GPIB.

4.4 Results

4.4.1 Panametrics V306

The left graph of Fig. 4.3 shows the transmit transfer functions of a Panametrics V306 determined by the various methods, the right graph presents its receive transfer function. The transfer functions determined by the different methods are similar and overlap. Except for the transfer spectra determined by the direct transmit experiment, which are significantly lower near 5 MHz. This is due to the presence of a low pass Butterworth filter with a cut-off point at 5 MHz in the measurement system. The accuracy is estimated at $\pm$ 15%, which is close to the accuracy of the hydrophone used.
Notice the difference in shape between the transmit and receive transfer spectra, this is caused by the frequency dependency of the transducer's impedance.

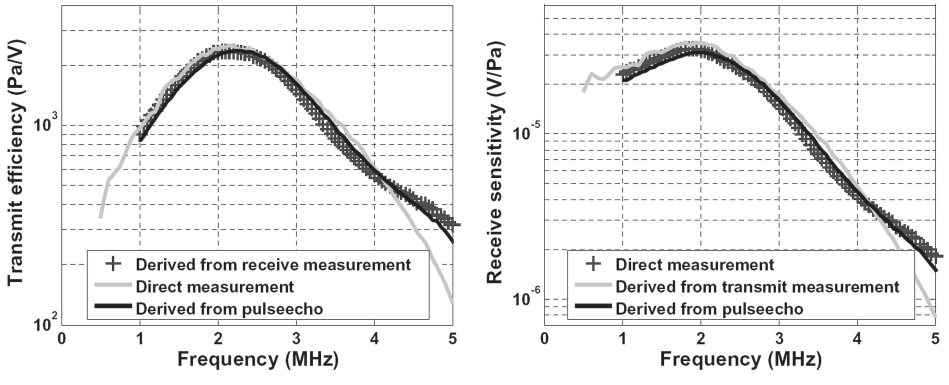

Figure 4.3: The transmit and receive transfer function of a Panametrics V306 are shown in the left and right graph respectively.

4.4.2 Custom made 1.5 mm transducer

The left graph of Fig. 4.4 shows the transmit transfer functions of the custom 1.5 mm transducer determined by the various methods, the right graph presents its receive transfer function.
The transfer functions determined by the different methods are similar. Below 2 MHz and above 7 MHz the SNR of the received signals was quite low. Between these frequencies the accuracy is estimated at $\pm$ 15%, which is close to the accuracy of the hydrophone used.
Notice the difference in shape between the transmit and receive transfer spectra, this is caused by the frequency dependency of the transducer's impedance.

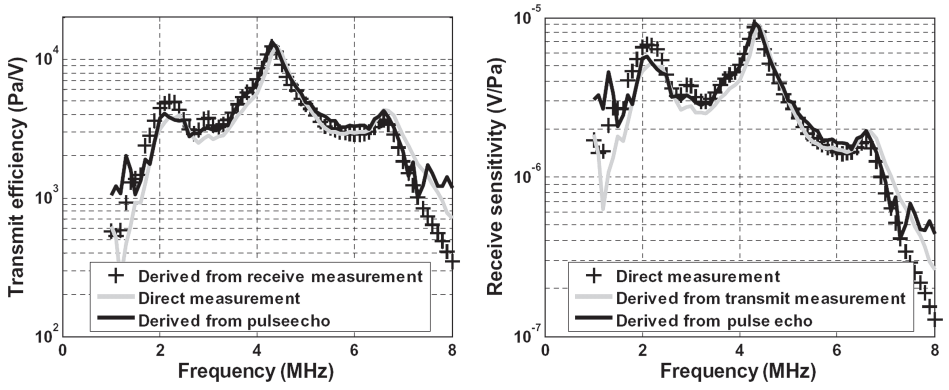

Figure 4.4: The transmit and receive transfer function of the custom built 1.5 mm transducer are presented in the left and right graph respectively.

4.5 Conclusion

The specific definitions of the transmit and receive transfer functions ensure that these transfer functions and the reciprocity theorem relating them are transducer characteristics and circuit independent.
All methods described are sufficiently accurate for absolute transfer function measurements, the particular choice of method is based on practical considerations. A reciprocal transducer can be completely characterized using a pulse-echo measurement and a vector impedance measurement, without the need for a hydrophone or calibrated transducer.
Because of these reasons, the proposed methods are particularly suited to select the optimal piezoelectric material (PZT, single crystal) for arrays used in reception only (3D scanning, superharmonic imaging) or to judge the performance of alternative transducer designs.
These methods are also important for selected experiments like single bubble behavior,

where the complicated low pressure bubble response makes the precise absolute characterization of the measurement system mandatory.

CHAPTER 5

A comparison of array element surface vibration calculated by finite element modeling and laser interferometer measurements

Paul L.M.J. van Neer, Guillaume Matte, Philipp Gatta, Massimo Pappalardo, Nico de Jong

Based on: proceedings IEEE Ultrasonics, 2008, 788-791

Abstract For several years the standard in ultrasound imaging has been second harmonic imaging. Recently, a new imaging modality dubbed superharmonic imaging (SHI) was proposed. SHI uses the higher - third to fifth - harmonics produced by either nonlinear propagation or contrast agent response. This modality requires a transducer with a high bandwidth (>130%), which was achieved by choosing different frequencies for the odd (4 MHz) and even (1 MHz) elements. For SHI it is important to minimize both crosstalk and the transmission of odd transducer harmonics. To determine the influence of geometry on these issues a 3D transducer model is necessary. In this paper we compare array element surface vibrations calculated by a finite element model (FEM) with measurements obtained using a laser interferometer system. A custom array was built (element size 13 mm x 0.2 mm, resonance frequency 1.6 MHz, no matching layer, backing 5.3 MRayl). Its elements were excited using continuous signals or impulses and its spatially and time dependant surface vibrations were measured in air using a laser interferometer setup. The array element (characterized by its dimensions, piezo parameters from the data sheet and measured bulk parameters of the backing) was modeled using the ANSYS 11 FEM package and subjected to the same

excitation. The fundamental resonance, third harmonic, fifth harmonic and lateral resonance of the array elements were measured at 1.6, 6.2, 9.9 and 7.9 MHz and predicted by the FEM simulation at 1.7, 6.1, 9.9, and 8.0 MHz. The excursion during continuous wave excitation was measured at 27.6 nm and predicted by FEM at 26.4 nm. The ripple in the surface displacement over the elevation axis of the element had a 1.2 - 1.3 mm wavelength both in the measurements and in the FEM simulation. Good agreement was achieved between the FEM predicted surface vibrations and the laser interferometer results.

5.1 Introduction

For several years the standard in ultrasound imaging has been second harmonic imaging. Recently, a new imaging modality dubbed superharmonic imaging (SHI) was proposed [Bouakaz et al., 2002a]. SHI uses the higher - third to fifth - harmonics produced by either nonlinear propagation or contrast agent response. This modality requires a transducer with a high bandwidth (>130%), which was achieved by choosing different frequencies for the odd (4 MHz) and even (1 MHz) elements [Bouakaz et al., 2004]. For SHI it is important to minimize both the transmission of odd harmonics by the interleaved array and the interelement crosstalk. The higher harmonic components used for SHI are low in amplitude, thus even low energy transmission of transducer harmonics reduces the image quality. Crosstalk limits the ring down of delayed signals from neighboring elements and the angular dispersion by increasing the effective element size [Guess et al., 1995]. The influence of geometry on these issues can not be determined using 1D models (such as the KLM model) and requires a 3D approach. Traditionally, beam pattern measurements and electric measurements on the connections of neighboring elements [Guess et al., 1995] have been used to evaluate crosstalk. Recently, techniques such as laser interferometry and finite element modeling (FEM) have gained popularity in the modeling of complex vibration modes and crosstalk of phased arrays based on piezomaterial and cMUT's. Caronti et al. [2005] used both 3D FEM [Caronti et al., 2005] and laser interferometry [Caronti et al., 2003, 2005] to describe the acoustic coupling between cMUT array elements. Kondo and Kitatuji [2004] applied both FEM and laser interferometry to describe the effects of composite matching layers on mechanical crosstalk and Branca et al. [2004] used laser interferometry to study the effect of filling materials on interelement coupling. Goldberg et al. [1997] used 3D FEM to predict the performance of multilayer transducers and to visualize their complex vibration modes.
In this paper we compare element surface vibration calculated by FEM with measured surface vibration obtained using a laser interferometer setup.

5.2 Methods

5.2.1 Custom array

A custom array was built based on CTS 3203HD piezomaterial, its backing had an acoustic impedance of 5.3 MRayl with an attenuation of 18 dB/cm at 1.6 MHz. No matching layer was applied. The array was cut into 18 elements using a diamond saw yielding an element size of 13 mm x 0.2 mm. The resonance frequency of the elements was 1.6 MHz. A picture of the array is displayed in Fig. 5.1.

5.2.2 Laser interferometer setup

An element of the array was excited by either a continuous sinusoidal signal at the array's resonance with amplitude 29 V_{pp} using a HP 8116A function generator (Agilent

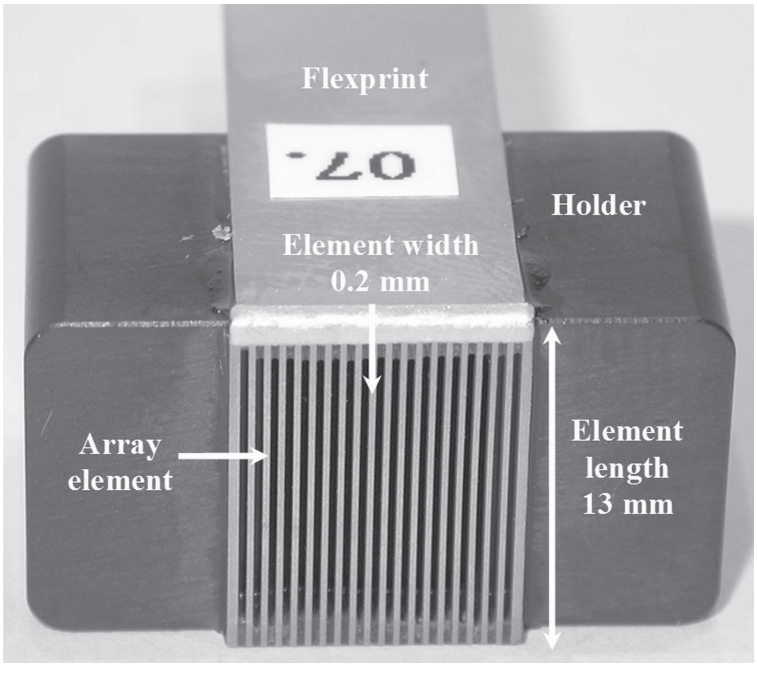

Figure 5.1: The custom built array.

Technologies Inc., Englewood, CO, USA) or by an impulse with amplitude -69 V using a Panametrics 5800 pulser/receiver (Panametrics, Waltham, MA, USA). The spatially and time dependant surface vibrations of the array elements in air were studied using a system originally realized by Gatta [2008] for the interferometric characterization of the vibrations of MEMS structures. The system was based on a Polytec MSV-300 laser scanning vibrometer system (Polytec GmbH, Waldbronn, Germany), similar to the one used by Caronti et al. [4, 5]. The laser interferometer consisted of a Polytec OFV 511 fiber interferometer connected to a Polytec MSV-Z-040 scanner controller and a Polytec OFV 2700-2 vibrometer controller. The interferometer equipment was mounted on a DMLM microscope (Leica Microsystems GmbH, Wetzlar, Germany) using a Polytec OFV 074 microscope adapter. The signals produced by the interferometer were digitized by a TDS 5034B oscilloscope (Tektronix Inc., Beaverton, OR, USA) at 100 MHz, which was triggered by the function generator. The oscilloscope was connected to a PC using an Ethernet connection. Labview 7.1 software (National Instruments, Austin, TX, USA) was used to control the xy-stage, laser interferometer and data acquisition. The array element surface vibration was studied using a laser spot diameter of 10 μm and a translation step size of 27 μm. In the case of continuous wave experiments the signal was averaged 8000 times for each measurement and filtered using an analogue filter with a

cut off frequency of 2 MHz, in order to reduce the effects of variance in signal quality due to the variability of element surface reflectivity and surface roughness. In the case of impulse response experiments 128 traces were averaged per measurement with a pulse repetition frequency of 100 Hz.

5.2.3 Finite element model

An array element was modeled using the ANSYS 11 FEM package (ANSYS Inc., Canonsburg, PA, USA) and subjected to the same excitation used in the laser interferometer experiments. Only a quarter of the array element needed to be modeled due to symmetry. The piezomaterial geometry had dimensions 6.5 mm x 0.88 mm x 0.1 mm and was based on CTS 3203HD. Its material parameters were based on the values reported by Sherrit et al. [1997]. The piezomaterial structure was meshed using the 20 node, 3D solid element SOLID226. The electrodes were assumed to be infinitesimally thin. The backing layer had dimensions 6.5 mm x 1.175 mm x 0.1 mm and was modeled using Maxwell viscoelasticity with a single time constant. The modeled backing was thin; the attenuation of the backing was set to ensure no reflections. The backing structure was meshed using the 20 node 3D viscoelastic elements VISCO89. The initial bulk modulus was taken to be 3.32 GPa and the initial shear modulus was 10.2 GPa. For both the associated time constant was 0.5 μs. The maximum frequency of interest was 10 MHz. The spatial sampling was chosen to be 12 points/wavelength at this frequency assuming the CTS 3203HD 33 direction wave speed of $\sim$3600 m/s. The sampling frequency was 25 MHz for the 'continuous' wave simulations and 100 MHz for the impulse simulations. A schematic of the model is displayed in Fig. 5.2 and the material properties used in the simulations are listed in table 5.1.

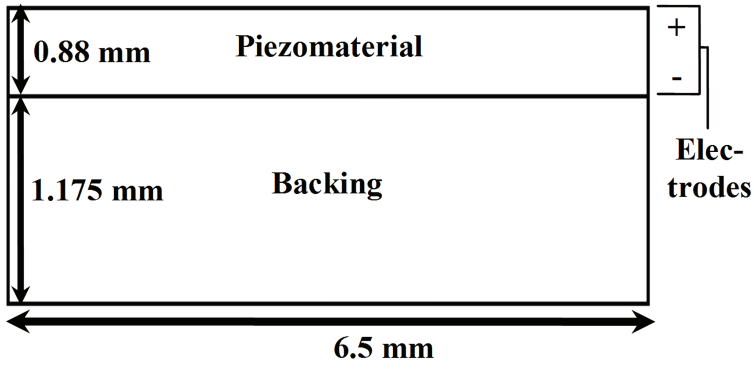

Figure 5.2: Array element geometry for FEM simulations.

5.3 Results

5.3.1 Continuous wave excitation

The mean element surface displacement versus time of the optical measurements and the FEM simulation are displayed in the top and bottom graph of Fig. 5.3 respectively.

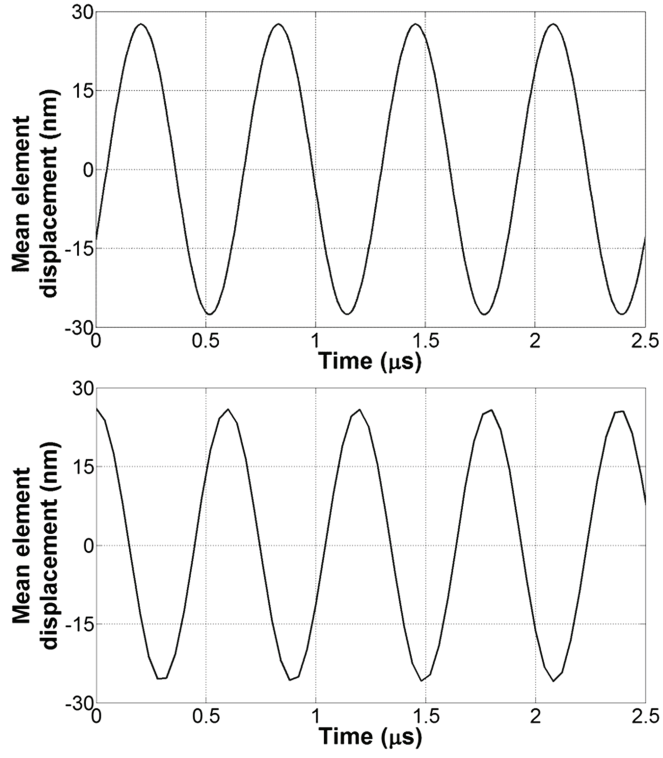

Figure 5.3: The mean element displacement versus time as optically measured on the top and as predicted by FEM simulations on the bottom.

The mean maximum excursion of the array element surface was 27.6 nm in the optical measurements versus a mean maximum excursion of 26.4 nm as predicted by the FEM simulation. The measured and the FEM predicted maximum excursion of the array element surface due to continuous wave excitation versus the location on the element elevation axis are shown in Fig. 5.4. The optical measurements did not start at the array element edge but a little distance away from the edge, due to poor reflectivity of the top electrode near the edge. Therefore, the measurements and the FEM simulation cannot be precisely superimposed: the apparent 180° phase shift between measurements and simulation is coincidental. The maximum excursion of the array element surface measured

during continuous wave excitation was between 14.5 and 32 nm. The ripple in surface displacement over the elevation axis of the element had a wavelength between 1.2 and 1.3 mm and amplitude of ∼2 nm. Notice the apodization in the measured excursion as the measurement position was further away from the center. The maximum excursion of the array element surface predicted by the FEM model was between 13.6 and 35.1 nm. The ripple in surface displacement over the elevation axis of the element had a wavelength between 1.1 and 1.2 mm and amplitude ∼7 nm.

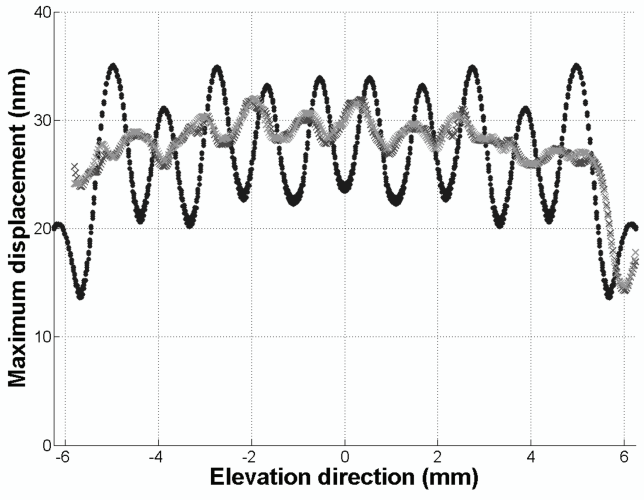

Figure 5.4: Optically measured and FEM simulation predicted maximum excursion of the array element surface, due to a continuous wave excitation with amplitude 29 V_{pp}, versus location on the element elevation axis. The FEM simulation predicted excursion is denoted by black dots, the optical measurements are denoted by light and dark grey crosses.

5.3.2 Impulse excitation

The measured and FEM predicted mean displacements of the array element surface due to impulse excitation are displayed in Fig. 5.5. The measured maximum mean displacement was ∼7.5 nm, and the FEM simulation predicted maximum mean displacement was ∼6.6 nm. After the initial peak the measured mean surface displacement decayed considerably faster than the FEM predicted mean surface displacement, except for a clear 130 kHz vibration trailing the initial excitation in the optical measurement. The absolute intensity of the Fourier transformed mean surface displacement of both the optical measurements and the FEM simulations as presented in Fig. 5.5 are displayed in Fig. 5.6. The optical measurements showed that the array had three resonances at 1.6, 6.2 and 9.9

MHz respectively. The FEM model predicts these resonances at 1.7, 6.1 and 9.9 MHz. A lateral mode was measured at 7.9 MHz, the FEM simulation put it at 8.0 MHz. Also, the FEM simulation yielded a resonance peak at 100 kHz.

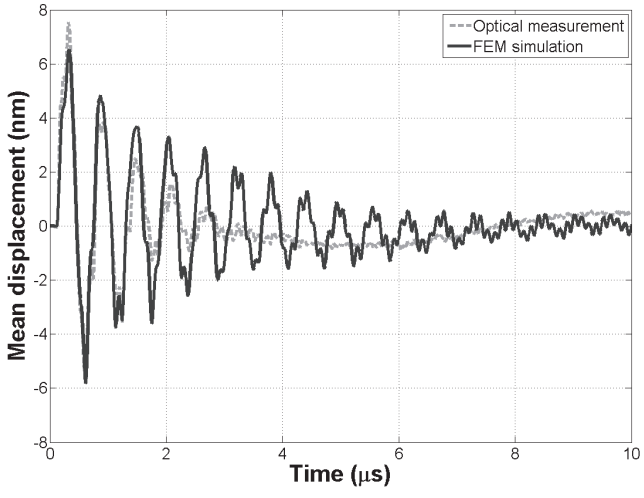

Figure 5.5: Optically measured and FEM simulation predicted mean excursion of the array element surface versus time, due to an impulse excitation with amplitude -69 V.

5.4 Discussion

5.4.1 Continuous wave excitation

There is good agreement between the FEM predicted mean maximum surface vibration (26.4 nm) and the laser interferometer measurements (27.6 nm). The wavelength of the ripple in surface displacement over the element elevation axis was the same in both the optical measurements and the simulation. The ripple originates from the interference of standing surface waves. The difference in ripple amplitude between experiment and simulation may be explained by the fact that only a single array element was modeled in the FEM simulation. Thus there is no energy transfer from the excited element to other elements or to the holder, allowing the standing waves to reach higher amplitudes.
Notice the apodization in the optically measured displacement over the element elevation axis and the drop in maximum displacement ($\sim$50%) at the element edge (Fig. 5.4). These effects may be attributed to the glue present between the array elements. However, there is a drop in maximum displacement near the edges of the simulated array

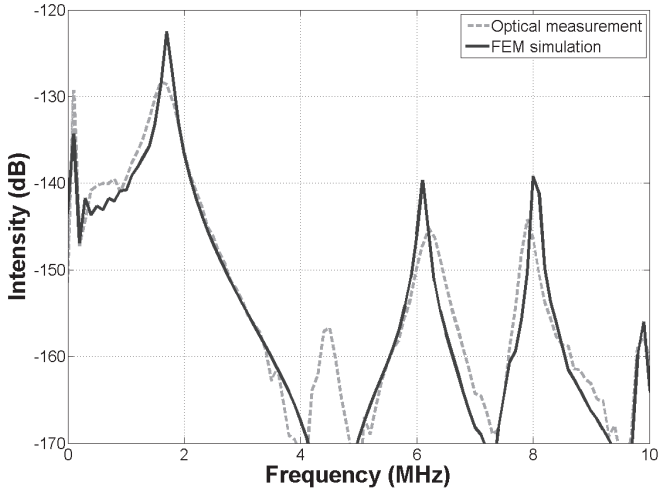

Figure 5.6: Absolute intensity of the Fourier transformed mean surface displacement, based on the time signal shown in Fig. 5.5.

element as well (no glue is included in the simulation). This drop may be explained by the superposition of surface waves.

5.4.2 Impulse excitation

The optical measurements and FEM results showed similar initial maximum mean displacements of 7.5 nm and 6.6 nm respectively. The difference in decay after the initial peak between the simulation and measurements can be explained by the implemented viscoelastic backing model - it is suboptimal - and the damping effects of glue and holder, which are not modeled in the simulation.
There is good agreement in the thickness mode and lateral mode resonance frequencies predicted by the FEM simulation and those found in the optical measurements. The small differences are caused by the slightly different piezomaterial loading in the FEM simulation - the model does not incorporate glue or the holder of the custom array. Also, the precision with which the material properties can be measured plays a part. The optical measurements do show an unexplained peak on 4.5 MHz, which is absent in the FEM simulation results. The resonance at 100 kHz in the FEM model and 130 kHz in the optical measurements is likely the element elevation resonance.

5.5 Conclusion

Good agreement was achieved between the FEM predicted surface vibrations and the laser interferometer results.
Next steps include an improved implementation of viscoelastic backing, and the modeling of the matching layers, electrical connections and housing in order to obtain a model of the interleaved design.

Acknowledgements We gratefully acknowledge the efforts of Alessandro Caronti, Giosu Caliano, Jerome Borsboom, Wim van Alphen and Geert Springeling.

Table 5.1: Material properties used in the FEM simulations

Property	Unit	Piezomaterial	Property	Unit	Backing
Elastic compliance (s^E)	[m^2/N x 10^{-11}]	s^E_{11}=1.56, s^E_{12}=-0.420, s^E_{13}=-0.823, s^E_{33}=1.89, s^E_{55}=3.92, s^E_{66}=3.98	Bulk modulus (K)	[GPa]	Initial: 3.22, End: 0.5
Piezoelectric strain coefficient (d)	[C/N x 10^{-10}]	d_{13}=2.95, d_{33}=5.64, d_{15}=5.60	Bulk modulus time constant (τ_K)	[μs]	0.5
Relative permittivity (K^T)	-	K^T_{11}=2417, K^T_{33}=3331	Shear modulus (G)	[GPa]	Initial: 10.2, End: 0.5
Density (ρ)	[kg/m^3]	7800	Shear modulus time constant (τ_G)	[μs]	0.5
Dielectric loss ($tan\delta_e$)	-	0.028	Density (ρ)	[kg/m^3]	3100
Mechanical loss (Q_m)	-	66			

CHAPTER 6

Transoesophagal probe for newborns

Thierry V. Scohy, Guillaume M. Matte, Paul van Neer, Ton van der Steen, Jackie McGhie, Ad Bogers, Nico de Jong.

Based on Ultrasound in Medicine and Biology 2009, vol. 35, no10, pp. 1686-1689

Abstract Current transesophageal probes are designed for adults and are used both in the operating theatre for monitoring as well as in the outpatient clinic for patients with specific indications, like obesity, artificial valves, etc. For newborns (5 kg), transesophageal echocardiography (TEE) is not possible because the current probes are too big for introducing them into the esophagus. There is a clear need for a small probe in newborns that are scheduled for complicated cardiac surgery and catheterization. We present the design and realization of a small TEE phased array probe with a tube diameter of 5.2 mm and head size of only 8.27 mm. The number of elements is 48 and the center frequency of the probe is 7.5 MHz. A separate clinical evaluation study was carried out in 42 patients [Scohy et al., 2007].

6.1 Introduction

The clinical application of transesophageal echocardiography (TEE) technology continues to progress, with various indications and diagnostic uses [Milani et al., 2003]. The most common indications for TEE in pediatric patients with congenital heart disease (CHD) are for assessment during cardiac surgery and interventional cardiac catheterization procedures [Ayres et al., 2005]. Another indication for TEE in pediatric patients is in situations in which the transthoracic technology is diagnostically inadequate because of poor quality or limited echocardiographic windows, which

is frequently encountered in patients receiving mechanical ventilation, and other critically ill patients in an intensive care unit. Other indications for TEE are pediatric patients with intracardiac conduits or patients with suspicion of CHD, but where transthoracic echocardiography is nondiagnostic [Ayres et al., 2005]. Until 1990, TEE evaluation in infants and children was not possible because probes were too large [Muhiudeen et al., 1998]. The development of miniaturized single - and biplane probes (from 3.3 to 9 mm diameter) generated a number of studies, which demonstrated that TEE can be performed safely in the pediatric population [Bruce et al., 2002, Andropoulus et al., 2000, Yumoto and Katsuya, 2002]. A multiplane TEE probe is an obvious advantage, certainly considering the complexity of the intracardiac defects in neonates [Shiota et al., 1999, Tardif et al., 1994, Yvorchuk et al., 1995]. Until recently, a safe investigation with the multiplane technique was limited to children of 5 kg [Sloth et al., 1996]. Recently, we demonstrated that a new Oldelft micromultiplane TEE probe (8.2 to 7-mm tip diameter, 5.2-mm shaft diameter) connected to a Philips iE33 ultrasound system (Philips, Andover, MA, USA) provided excellent intraoperative TEE assessment in neonates as small as 2.5 kg without major complications [Scohy et al., 2007]. In this study, we describe the physical characteristics and the acoustic properties of the Oldelft/Philips micromultiplane TEE probe.

6.2 Measurements and Methods

6.2.1 Transducer

The TEE transducer consist of 48 elementa. The element width is 70 μm and the kerf 30 μm. The center 32 elements measure 7.5 mm in the elevation, whereas eight elements at both ends of the transducer are tapered from 7.5 to 3.75 mm (size of element 1 and 48), resulting in an octagonal shape. The transducer center frequency is 7.5 MHz, which is higher than the standard 5-MHz frequency of an adult TEE probe. The probe was connected to a Philips IE33 scanner for the clinical evaluation and to a dedicated phased array system (Lecoeur Electronique, Chuelles, France) for acoustic in vitro measurements. A photograph of the transducer is shown in Fig. 6.1.

Figure 6.1: Photograph of the new probe (micro-multi) together with 2 commercially available TEE probes. Top: Adult probe, Middle: mini multiplane probe, Bottom: micro multiplane probe.

6.2.2 Acoustic measurements

The probe was connected to an experimental phased array system (Lecoeur Electronique), enabling optimal control in transmission. The acoustic field was measured with a calibrated hydrophone of 0.2-mm diameter (Precision Acoustics, Teddington Middlesex, UK), of which the position was

controlled by a computer-controlled X-Y-Z system (6K4, Parker Hannifin Corporation, Rohnert Park, CA, USA). For beam profile measurements, the scanner operated in a single-line mode steering at 0 and focused at an axial distance of 2 cm. The profiles were measured using a transmit pulse of two periods and a center frequency of 7.5 MHz. The generated peak pressure at the focal point was kept low (240 kPa).

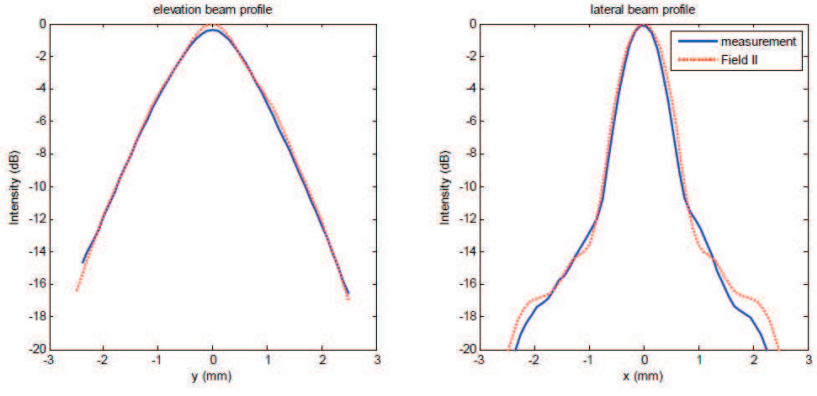

Figure 6.2: Lateral (right) and elevation (left) beam profile at an axial distance of 2 cm

6.2.3 Simulations

Simulations were done using Field II [Jensen and Svendsen, 1992, Jensen, 1996]. For the simulations, the same settings were used as for the measurements (lateral focus at 2 cm, elevation focus at 6 cm, steering 0 degrees, acoustic pressure 240 kPascal).

6.3 Results

Figure 2 shows the beam profiles in lateral and elevation at a distance of 2 cm. The lateral and elevation 3 dB beamwidths (one way) were, respectively, 0.5 mm and 1 mm. The dotted line in the figure denotes the result of the simulation, which is in agreement with the measurements. Figure 6.3 shows the acoustic pulse in focus (left) and the corresponding frequency spectrum (right). The maximum in the frequency spectrum is at 7.5 MHz, as seen in the figure. By considering this value as the center frequency, the relative bandwidth at 6 dB is 53%.

6.3.1 Clinical examples

Figures 6.4, 6.5 and 6.6 have been acquired as part of a routine intraoperative TEE examination in a 1-week-old neonate weighing 2.6 kg, with transposition of the great arteries, and who was scheduled for arterial switch procedure. Institutional review board approval/consent was waived.

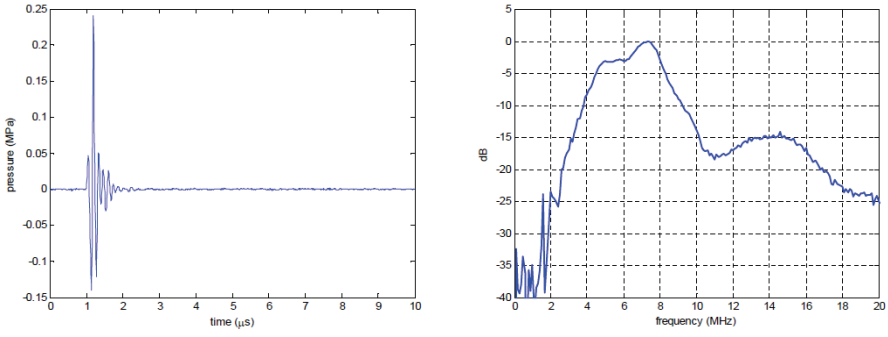

Figure 6.3: Acoustic pulse (left) and corresponding frequency spectrum at an axial distance of 2 cm.

Figure 4 shows the aorta and the pulmonary artery before the arterial switch procedure for transposition of the great arteries; this image could only be visualized in a 113 multiplane angle. In Fig. 5 we measured the velocity of the septal site of the mitral valve annulus with pulsed-wave tissue Doppler imaging, which can be used to evaluate left ventricular function. Figure 6 shows the post-repair patency of the coronary artery after implantation in the aorta with color Doppler. We also distinguish the bifurcation of the mainstem into the left anterior descending and the circumflex coronary arteries.

6.4 Conclusion

We present the design and realization of a small TEE phased array probe with a tube diameter of 5.2 mm. The image quality of the probe is good and the probe has a clear diagnostic value for neonates.

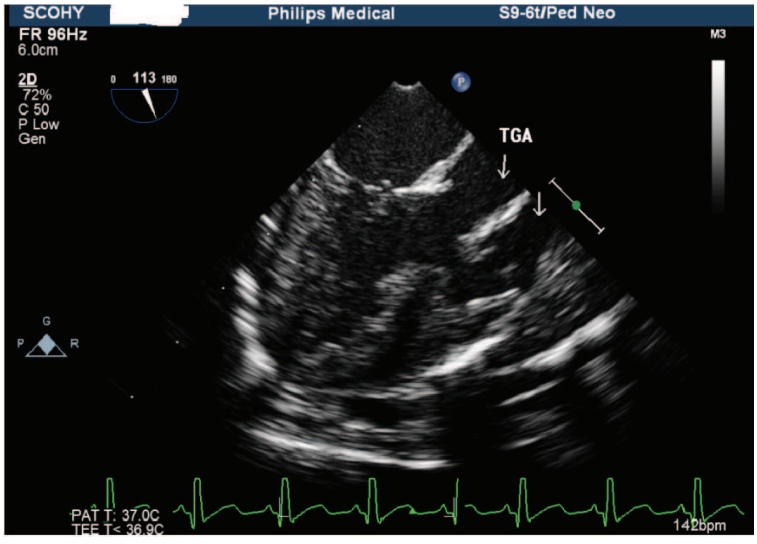

Figure 6.4: Aorta and Pulmonary artery in Transposition of the Great Arteries (TGA) in a 2.6 kg neonate in a multiplane angle of 113.

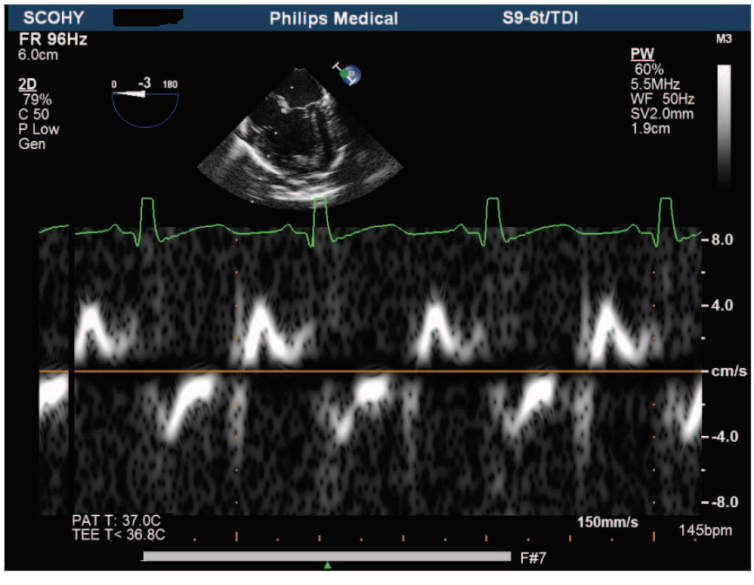

Figure 6.5: Pulsed-wave Tissue Doppler Imaging at the septal site of mitral valve annulus in a 2.6 kg neonate.

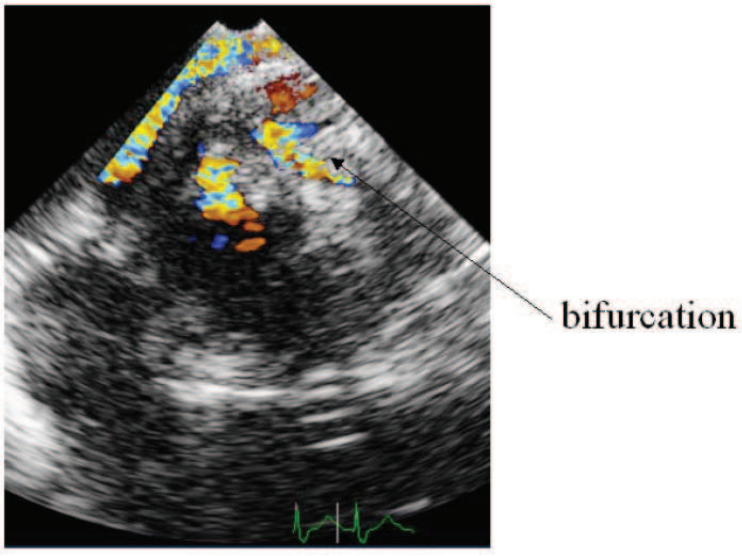

Figure 6.6: color Doppler of the maistem coronary artery after reimplantation in the aorta.

Part 3 : Superharmonic imaging for tissue

CHAPTER 7

Superharmonic imaging: development of an interleaved phased array transducer

Paul L.M.J. van Neer, Guillaume Matte, Mikhail G. Danilouchkine, Christian Prins, Franc van den Adel, Nico de Jong

Based on: IEEE Transactions on Ultrasonics, Ferroelectrics, and Frequency Control, 2010, 57(2):455-468

Abstract For several years the standard in ultrasound imaging has been second harmonic imaging. A new imaging technique dubbed ”superharmonic imaging” (SHI) was recently proposed. It takes advantage of the higher - third to fifth - harmonics arising from nonlinear propagation or ultrasound contrast agent (UCA) response. Next to its better suppression of near-field artifacts, tissue SHI is expected to improve axial and lateral resolutions resulting in clearer images than second harmonic imaging. When SHI is used in combination with UCAs, a better contrast-to-tissue ratio can be obtained. The use of SHI implies a large dynamic range and requires a sufficiently sensitive array over a frequency range from the transmission frequency up to its fifth harmonic (bandwidth $> 130\%$). In this paper, we present the characteristics and performance of a new interleaved dual frequency array built chiefly for SHI. We report the rationale behind the design choice, frequencies, aperture and piezomaterials used. The array is efficient both in transmission and reception with well behaved transfer functions and a combined -6 dB bandwidth of 144%. Moreover, there is virtually no contamination of the harmonic components by spurious transducer transmission, due to low element-to-element crosstalk (< 30 dB) and a low transmission efficiency of the odd

harmonics (< 46 dB). The interleaved array presented in this article possesses ideal characteristics for SHI, and is suitable for other methods like second harmonic, subharmonic and second order ultrasound field (SURF) imaging.

7.1 Introduction

A decade ago it became possible to improve ultrasound image quality by exploiting the nonlinear nature of wave propagation. The technique is called tissue second harmonic imaging and is based on the selective imaging of the second harmonic frequency. Compared to fundamental imaging second harmonic imaging has a higher resolution and is less sensitive to near-field artifacts, clutter and off-axis scatterers [Bouakaz and de Jong, 2003]. As a result second harmonic imaging has been the standard in tissue imaging for several years. Nonlinear effects are not just exploited in tissue imaging. In fact the selective imaging of the second harmonic band was originally intended for ultrasound contrast agent (UCA) enhanced imaging [Bouakaz and de Jong, 2003]. Used in this way the technique improved the contrast-to-tissue ratio (CTR) compared to fundamental imaging, thus enabling better imaging of blood flow [Bouakaz et al., 2002a].
Several other methods have been proposed to exploit the nonlinear behavior of UCAs. A new and promising imaging modality for the nondestructive imaging of UCAs is subharmonic imaging [Shi and Forsberg, 2000, Chomas et al., 2002, Forsberg et al., 2004, Biagi et al., 2007]. This imaging method is primarily intended to estimate blood perfusion by accurately quantifying the refresh of UCAs in a vascular bed after UCA destruction [Chomas et al., 2002]. The principal advantage of UCA subharmonic imaging compared to UCA (second) harmonic imaging is that subharmonic signals are not generated in tissue at diagnostic pressures and frequencies maintaining a high CTR [Forsberg et al., 2004]. The optimal subharmonic imaging technique described in literature insonifies the UCA using a low pressure excitation pulse - but still higher than the UCA pressure threshold for subharmonics - at twice the UCAs resonance frequency [Chomas et al., 2002].
Another promising UCA imaging modality utilizing nonlinear UCA behavior is second order ultrasound field (SURF) imaging or radial modulation imaging. In this method a low frequency low pressure pulse is transmitted (0.5 - 2 MHz), which manipulates the contrast agent around resonance by altering its scattering properties. In conjunction with the low frequency pulse a high frequency pulse (3 - 14 MHz) is transmitted to detect the changes in scattering [Shariff et al., 2006, Masoy et al., 2008]. The main advantage of this imaging technique is that it allows for UCA detection at clinically high frequencies - higher frequencies than the resonant frequencies of the UCAs. Example *in-vivo* B-mode results were presented by [Masoy et al., 2008], who obtained contrast enhanced images of pig kidneys with a CTR of 15 - 40 dB.
Recently, a new imaging modality dubbed 'superharmonic imaging' (SHI) was proposed. The modality improves on second harmonic imaging by combining the third to fifth harmonics arising from nonlinear wave propagation or contrast-agent response [Bouakaz et al., 2002a]. Tissue SHI efficiently suppresses near-field artifacts, reverberations, and off-axis artifacts in addition to the enhanced lateral and axial resolution. The resulting images showed more details than those produced by second harmonic imaging [Bouakaz and de Jong, 2003]. Recently, this was confirmed by simulations and *in-vitro* experiments conducted by Ma et al. [2006]. SHI is also promising for UCA enhanced imaging.

It has been demonstrated by Bouakaz et al. [2002a] that the CTR increases as a function of the order of the harmonic frequency. Thus, SHI in combination with contrast agents produces a higher CTR than second harmonic imaging, while at the same time minimizing shadowing effects. Until now, imaging with harmonics higher than the second one has been hampered by signal-to-noise ratio (SNR) issues, due to the progressively lower energy content of these harmonics.
A traditional phased array design is inadequate for the implementation of the above imaging modalities. In the case of SHI the principle of transmission at the fundamental and receiving the third to fifth harmonic implies a -6 dB bandwidth $> 130\%$, a considerably larger bandwidth than that achievable with a conventional array configuration. Although -6 dB bandwidths as high as 140% are reported in the literature for single element transducers made from a 1-3 single crystal-epoxy composite, the actual peak bandwidth at -6 dB reported for single crystal arrays are in the order of 95% [Rehrig et al., 2003, Zipparo et al., 2004, Li et al., 2007] - not sufficient for SHI. Next to the bandwidth demand, the implementation of SHI requires an array to be efficient in transmission - to generate significant higher harmonics - and sensitive in reception - the reflected harmonic energy will be low.

This paper presents the rationale behind, construction of and performance measurements of a very broadband array primarily intended for both tissue and UCA enhanced cardiac medical imaging. The array is mainly optimized for SHI, but is also capable of regular second harmonic imaging. Furthermore, the suitability of the array for UCA techniques, such as subharmonic and SURF imaging, is discussed.

7.2 Materials and methods

7.2.1 Requirements

The requirements for the new array can be listed as follows:

1. Very broad bandwidth. For SHI, the principle of transmission at the fundamental and receiving the third to fifth harmonic implies a -6 dB bandwidth $> 130\%$.

2. High efficiency in transmission. For optimal image quality in the cases of tissue SHI and second harmonic imaging the peak pressure at focus should be as close as possible to the 1.9 MI limit allowed by the FDA.

3. High sensitivity in reception. In the case of the imaging modalities based on harmonics the amplitude of the reflected signal at higher harmonic frequencies will be low for both nonlinear propagation and UCA produced harmonics. Noise levels of ultrasound imaging systems are generally in the order of 10 μ V_{rms}, thus a receive sensitivity of $\sim$10 μ V/Pa is required.

4. Have a good acoustic field with grating lobes of acceptably low amplitude. Cobbold [2007] states that grating lobe levels should be 30 - 40 dB below the central lobe response at the receiving frequency of interest.

The main application of the array will be echocardiography, which adds the following extra requirements:

1. A small enough footprint to facilitate imaging through the ribs. Generally cardiac transducers have a footprint of about 15 mm x 15 mm.

2. Be optimized for an imaging depth of 0.5-15 cm.

7.2.2 Design options

Several designs meet the bandwidth requirement for SHI [Hossack and Auld, 1993, Hossack et al., 2000, Bouakaz et al., 2002a, Zhou and Hossack, 2002, Bouakaz et al., 2004, Mills, 2004, Zhou et al., 2005, Akiyama et al., 2006, Yaralioglu et al., 2006, Ferin et al., 2007]. In the following paragraphs we list these alternatives and consider their advantages and disadvantages.
The first option is to stack two active layers (usually PZT or a PZT composite) with different resonance frequencies on top of each other for each array element [Hossack and Auld, 1993, Hossack et al., 2000, Zhou and Hossack, 2002, Akiyama et al., 2006]. Advantages of this configuration are a limited total footprint of the array and ease of manufacture. Its main disadvantage is the electromechanical coupling between both active layers. This causes troughs in the frequency response of the transducer, if the resonance frequencies of both active elements are close to each other. Hossack and Auld [1993] presented a study on a transducer design consisting of a piezoelectric layer and an active (piezoelectric) matching layer. A proper adjustment of the phase response of the active matching layer and the subsequent addition of the responses of both active layers yielded a well behaved broadband transfer function. Zhou and Hossack [2002] showed in a finite element analysis study that the transfer function of a dual active layer transducer can be further improved with matched filtering. However, fairly complicated electronics [Hossack and Auld, 1993, Hossack et al., 2000] and knowledge of the phase transfer function of each element are required for successful implementation. Also, the choice of matching layer characteristics is not straightforward, as the active layer used in transmission has a significantly different resonance frequency than the layer used in reception.
A second alternative was reported by Akiyama et al. [2006]. They presented an ultra broadband transducer used in a mechanical sector scanner. The design features a PZT layer for transmission and a PVDF layer for reception. The PVDF layer functions well below its resonance frequency, to guarantee electromechanical decoupling. However, the absolute sensitivity of PVDF applied in this manner is generally low.
The third option is a horizontal stack topology, where two low frequency arrays are positioned laterally on both sides of a central high frequency array [Ferin et al., 2007]. The

main advantage of this design is that the initial performance of each subarray is not modified. Disadvantages are the limited overlap of both acoustic beams and the increased footprint in the elevation dimension relative to a regular array design.
The fourth alternative is an interleaved configuration as proposed by Bouakaz et al. [2002a, 2004], where the even elements are used in transmission and the odd elements are used in reception. The main advantages of this design are the full overlap of the transmission and receive beams and a small footprint. Disadvantages are its relatively complicated manufacture and its intrinsically reduced sensitivity as only half the elements are used in reception - necessary to keep the footprint size limited.
A final option is capacitive micro machined ultrasound transducers (cMUT's). cMUT transducers with -6 dB bandwidths of 130% have been reported in literature [Mills, 2004, Zhou et al., 2005]. However, cMUTs are held back by challenges such as achieving high output pressures [Yaralioglu et al., 2006], their inherent nonlinearity and relatively high crosstalk [Zhou et al., 2005]. One of the most important difficulties of cMUT technology is the contradicting requirement regarding the gap height to get both a high sensitivity in reception and a high output pressure in transmission [Yaralioglu et al., 2006]. Mills [2004] reported pulse-echo gains of cMUT transducers, which were between 10 and 20 dB less than a comparative PZT transducer.

After careful consideration of the advantages and disadvantages of each option the interleaved design was chosen. Next to obvious advantages, such as fully overlapping beams and a low foot print, there are no fundamental problems associated with this design. There is no direct electromechanical coupling between the elements, because the acoustic stacks for transmission and reception, including the associated circuitry, are fully separated. Also, the use of piezoceramics - PZT, single crystal or piezocomposites - ensures operation in the linear regime, even at high output pressures. In this way any transmission of harmonics due to device nonlinearity, which considerably reduces the dynamic range of the imaging system, can be prevented. This fact is particularly important for SHI, as the level of higher harmonics generated by either nonlinear propagation or UCA response will be low.
The design does have an intrinsically reduced sensitivity in reception. However, this is alleviated by the fact that - like all designs with completely separate active elements for transmission and reception - each element can be acoustically matched and electrically tuned for its specific role.

7.2.3 Frequency

After selecting a design the transmission frequency has to be chosen. This frequency influences other characteristics of the array, such as the receive frequency, layer thicknesses and element dimensions.
For fundamental imaging the transmission frequency used in clinical echocardiography is $\sim$3.5 MHz [Kasprzak et al., 1999]. For both tissue and UCA enhanced second harmonic imaging the fundamental transmission frequency used in clinical echocardiogra-

phy ranges between 1.6 - 1.8 MHz [Kasprzak et al., 1999]. It is expected that for tissue SHI the transmission frequencies will be lower still. The optimal transmission frequency for tissue SHI is intrinsically dependent on the level of the third to fifth harmonics at distances typical for cardiac imaging. Consequently, the level of these harmonics is determined by two competing phenomena - nonlinear propagation and attenuation. In order to find the optimal transmission frequency for SHI we used a combination of nonlinear and linear simulations. Forward propagation was simulated using the Burgers equation, which describes the propagation of finite-amplitude plane progressive waves. The solution was found as a complex Fourier series using the iterative computation scheme given by Cobbold [2007]. The back propagation was assumed to be linear. The acoustic nonlinearity parameter (B/A) was taken to be 5.8 and the attenuation was modeled as $\alpha = a.f^b$ with a = 0.52 dB.cm^{-1}.MHz^{-b} and $b = 1$. Furthermore, a density of 1060 kg/m^3 and an acoustic wavespeed of 1529 m/s were used. These values were reported for human fetal or dog cardiac tissue [Duck, 1990]. Calculations were performed for transmit frequencies between 0.5 - 1.8 MHz. The initial MI was kept at 1.5. The imaging depth was taken between 0.5 - 15 cm. The intensities of the first five harmonics and the superharmonic versus the transmission frequency are shown in Fig. 7.1 for an imaging depth of 10 cm. The simulations showed that the frequency giving the optimal compromise between the rapidity of the build-up of harmonics at short distances and the attenuation of the harmonics at large distances was $\sim$1 MHz. This frequency was chosen as the resonance frequency of the low frequency subarray. Correspondingly, a resonance frequency of $\sim$4 MHz was opted for the high frequency subarray.

The optimal frequency for tissue SHI generally agrees with the requirements for UCA enhanced SHI, as the UCAs used for cardiac applications are resonant at 1 - 5 MHz [Dawson et al., 1999]. More specifically, Sonevue® and Definity®/Luminity® have reported resonance frequencies in the range of 1.5 - 3.1 MHz [Masoy et al., 2008].

7.2.4 Element geometry

The next feature to be established is the geometry of the two subarrays. The number and size of the array elements has a profound effect on the acoustic wave field, but also affects the ease of manufacture.

Elevation dimension

The elevation dimension of the low frequency subarray was chosen to be 16 mm. This value was small enough for the ultrasound beam to pass unimpeded between the ribs, but is still as high as possible to optimize the energy transferred into the medium. Due to the method used to interleave the elements, the elevation size of the high frequency subarray was 13 mm.

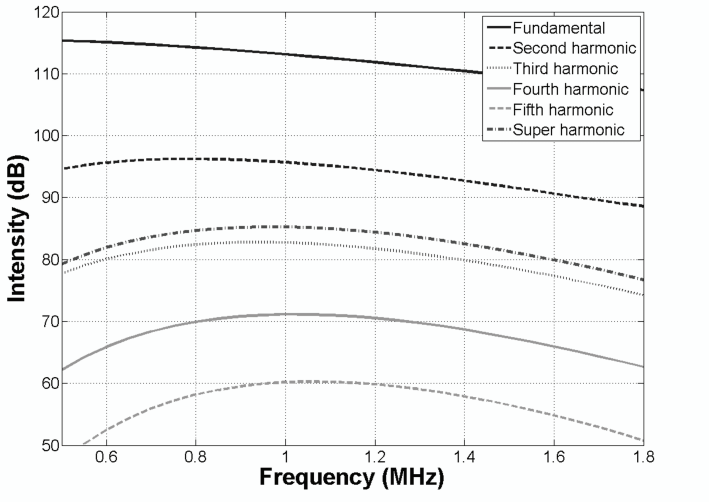

Figure 7.1: The intensity of the first five harmonics and the superharmonic versus the transmission frequency at an image depth of 10 cm. The intensity values are relative to 1 Pa. The forward propagation was modeled using the Burgers equation, the back propagation was assumed to be linear. The acoustic nonlinearity parameter (B/A) was 5.8 and the attenuation was modeled as $\alpha = a.f^b$ with a = 0.52 dB.cm^{-1}.MHz^{-b} and $b = 1$. The density was 1060 kg/m^3 and the acoustic wavespeed 1529 m/s. The initial MI was 1.5.

Lateral dimension: kerf/pitch

The spacing between the elements of the final interleaved array is a compromise between the desire to waste as little as possible of the footprint real estate and the ability to reliably merge both subarrays - a critical step in the production process. If the elements of improperly merged subarrays touch each other, the element transmit efficiency and receive sensitivity are suboptimal. Moreover, crosstalk levels are increased. Practical experience showed that an inter element spacing of 50 μm was optimal.

The width of the elements for both subarrays was the same in order to facilitate the array production process. The principal compromise for the lateral element size/pitch is the desire to have an as high as possible pitch-to-kerf ratio, whilst still having acceptable grating lobe levels at the highest intended transmitting frequency for the tissue imaging modalities (which is 1.6 - 1.8 MHz for tissue second harmonic imaging). The effects of grating lobes are less important for UCA imaging, as UCAs exhibit a very nonlinear pressure dependent response at pressures above 50 - 100 kPa [Emmer, 2009]. The FIELD II simulation program [Jensen and Svendsen, 1992, Jensen, 1996] was used to evaluate the peak intensities of the fundamental grating lobe relative to the main beam versus the

subarray pitch at transmission frequencies of 1.7 - 1.8 MHz and a steering angle of 35°. The element elevation size was 13 mm and the geometric elevation focus was 6 cm. No lateral focus was applied. The simulations were performed using 3 cycle sine bursts, which were Gaussian apodized. The propagation medium was assumed to be lossless. The peak intensities of the second harmonic grating lobe relative to the main second harmonic beam were estimated from the fundamental levels using the Fubini solution for weakly shocked plane waves produced by a monofrequency source [Cobbold, 2007]. A graph detailing the peak intensities of the simulated grating lobe versus the subarray pitch is shown in Fig. 7.2. Note that the subarray pitch was twice the element width plus twice the 50 μ m element spacing of the final interleaved array. A subarray pitch of 0.5 mm yields a lateral element size of 0.2 mm (Fig. 7.2). For this chosen pitch the second harmonic levels in the grating lobe were $\sim$-45 dB at 1.7 MHz, $\sim$-38 dB at 1.75 MHz and $\sim$-33 dB at 1.8 MHz relative to the second harmonic of the main bundle. The positions of the grating lobes in these cases were -83°, -79° and -77° respectively. The obtained characteristics match the requirements for grating lobe levels, which should be at least 30 - 40 dB below the central lobe response [Cobbold, 2007].

To keep the total footprint size practical, the final interleaved array consisted of a total of 88 elements, 44 of which were used in transmission and 44 were used in reception. This yielded a total footprint of 16 mm x 22 mm.

7.2.5 Choice of piezomaterial

To optimize the receive sensitivity research was conducted to select the optimal piezomaterial for an array with the selected frequency and aperture. After the piezomaterial was selected, the matching and backing materials were chosen in order to optimize each subarray for bandwidth.
A preselection of commercially available piezomaterials was made by careful consideration of their datasheet properties and by using the KLM model [Leedom et al., 1971]. Of these selected piezomaterials custom arrays (18 elements, element size 13 mm x 0.2 mm, pitch 0.5 mm, resonance frequencies 3 - 4 MHz, backing 5.3 MRayl, no matching layers) were constructed in order to compare their performance in both transmission and reception. Columns 1 and 2 of Table 7.1 provide a summary of custom array characteristics. The arrays with large element variance were repoled in an attempt to improve performance. A voltage of 300 V DC was applied over the element electrodes for about 30 minutes. This voltage was chosen to prevent over-poling of single crystal material and corresponds to an electric field strength of $\sim$700 V/mm.

The performance of the custom arrays was evaluated in terms of:

1. the maximal peak of the receive transfer function (shortened in this article as sensitivity) and the maximal peak of the transmit transfer function (shortened in this article as efficiency) of each element.

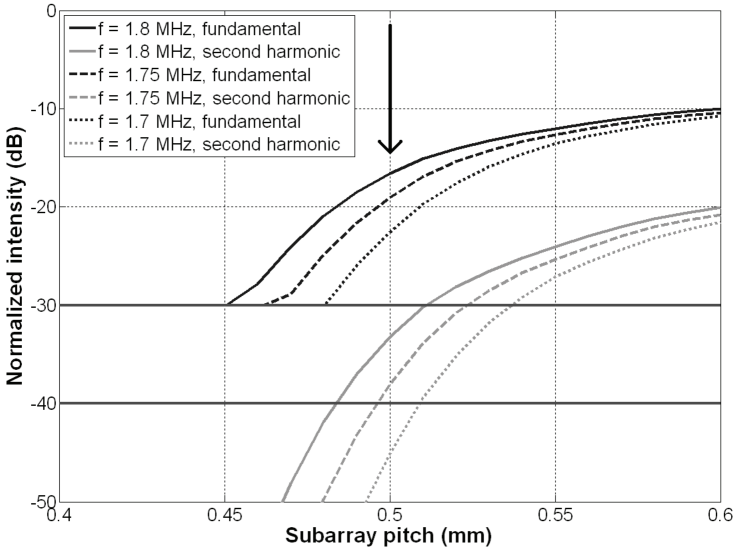

Figure 7.2: The relation between the fundamental peak grating lobe intensity versus the subarray pitch, simulated using Field II. The grating lobe intensity was normalized by the main beam peak intensity. Note that the subarray pitch was double the element width plus double the 50 μm element spacing of the interleaved array. The peak second harmonic intensity of the grating lobe was estimated from the fundamental using the Fubini solution. The simulations were performed using Gaussian apodized 3 cycle sine bursts at center frequencies of 1.7, 1.75 and 1.8 MHz. The element elevation size was 13 mm and the geometric elevation focus was 6 cm. The beam was unfocused in the lateral direction and steered 35°, the propagation medium was assumed to be lossless. The horizontal lines are at the intensity levels at which the grating lobe levels are low enough for high quality imaging [Cobbold, 2007]. The subarray pitch used in the final interleaved array is indicated by the black arrow.

2. The SNR. The SNR was determined for continuous ultrasound at the element's resonance frequency and a pressure of 1 Pa.

Table 7.2 summarizes the performance results of all 8 custom arrays. We considered the essential characteristics of each array, such as the resonance frequency, the mean and standard deviation of the sensitivity and efficiency, the -6 dB bandwidth, the impedance and the SNR while receiving a 1 Pa pressure wave.

The custom array constructed of CTS 3203HD PZT was the most sensitive in our study and this piezomaterial was used for the interleaved array.

A few remarks have to be made. In this study no correction for differences in piezomaterial acoustic impedance was made, as preliminary calculations indicated that the correction factors were small compared to actual sensitivity differences - even when comparing composite piezomaterial to PZT. Also, the sensitivity as expressed in μV/Pa is influ-

Table 7.1: Custom array and final interleaved array characteristics

	Custom array	Interleaved array low frequency subarray	Interleaved array high frequency subarray
Nr. of elements	18	44	44
Resonance frequency [MHz]	3 - 4	1	3.7
Element size [mm x mm]	13 x 0.2	16 x 0.2	13 x 0.2
Pitch [mm]	0.5	0.5	0.5
Piezomaterial	Various	CTS 3203HD	CTS 3203HD
Matching layers	-	1	2
Backing [MRayl]	5.3	3.2	3.2
Lens	-	Elevation, focus 6 cm	Elevation, focus 6 cm

enced by the resonance frequency of each array element. The resonance frequencies of the undiced slabs of piezomaterial lay between 4.0 to 4.9 MHz. However, KLM model simulations established that the effect of variation of the resonance frequency was less than 1 dB. Therefore, no correction was made for this effect.
The custom arrays based on composite piezomaterial had a somewhat low sensitivity. A retrospective investigation using an optical microscope showed damaged elements due to the dicing process. The arrays built using single crystal material had low mean sensitivities with high standard deviations and similar -6 dB bandwidths compared to PZT based arrays - even after repoling. This was different from earlier studies, in which single crystal material was found to be superior in performance to PZT [Rehrig et al., 2003, Rhim et al., 2005, Li et al., 2007, Rhim and Jung, 2007]. Part of the explanation is that the array element height-to-width ratio was $\sim$2:1, which is not ideal for 33-mode vibrations. Also, the effects may be related to dicing difficulties. The custom arrays were diced using a diamond saw. A visual inspection using a microscope of the array elements showed that small chips had broken off the brittle single crystal material during dicing. Temperature dependent degradation of the single crystal properties could not have been the cause, as the custom array production process takes place at low temperatures (below 70°C).

7.3 Array prototype

The transducer consisted of two interleaved subarrays with 88 transducer elements in total. The low and high frequency elements were mechanically separated and electrically decoupled. That enabled the optimization of each element (eg., matching layers, electrical tuning) for its specific role. Both the low and high frequency subarrays were built using CTS 3203HD piezomaterial. The subarray optimized for transmission had a resonance frequency of 1.0 MHz and consisted of 44 elements. The low frequency elements had a single matching layer and a backing of 3.2 MRayl. The low frequency element size

was 16 mm x 0.2 mm and the subarray had a pitch of 0.5 mm. The subarray optimized for reception had a resonance frequency of 3.7 MHz and was composed of 44 elements. The high frequency elements had two matching layers on the front and a backing with an impedance of 3.2 MRayl. The high frequency element size was 13 mm x 0.2 mm and the subarray had a pitch of 0.5 mm. A lens with a geometric elevation focus at an axial distance of 6 cm was attached to the final interleaved transducer. The total footprint of the interleaved transducer was 16 mm x 22 mm. The electrical tuning of the final interleaved transducer to the imaging machine was optimized for SHI. A coil was mounted in series with each element of the low frequency subarray and a coil was fitted in parallel to each element of the high frequency subarray.
Each subarray was constructed separately and cut with a diamond saw. The kerf between the elements was 0.3 mm for both subarrays. After cutting of the two subarrays, special tooling was used to merge the two subarrays, ensuring that the adjacent elements did not touch each other and aligning the front of both subarrays on the same plane.
The final interleaved transducer is shown schematically in Fig. 7.3. A summary of its characteristics is given in columns 3 and 4 of Table 7.1. The transducer was manufactured by Oldelft Ultrasound, Delft, the Netherlands.

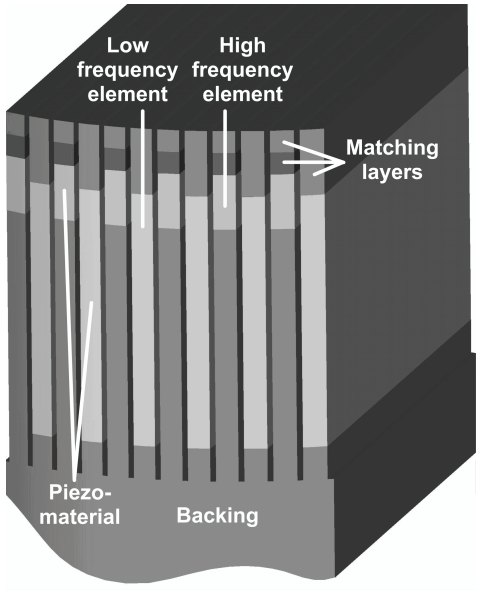

Figure 7.3: Schematic showing the various parts of the final interleaved array transducer.

7.4 Acoustic characterization

The final interleaved array transducer was characterized by measuring its efficiency in transmission as well as its sensitivity in reception. For that, we determine the transmit and receive transfer functions of all the elements. Also, lateral and elevation beam profiles were measured at high pressure ultrasound. Finally, the array's electrical and mechanical crosstalk was measured.

7.4.1 Transfer functions

Definitions

The transducer transmit transfer function ($T_t(\omega)$) is defined as

$$T_t(\omega) = \frac{|p_0(\omega)|}{|V_T(\omega)|}, \tag{7.1}$$

with $p_0(\omega)$ the pressure at the transducer surface and $V_T(\omega)$ the voltage over the transducer electrodes.
The receive transfer function $T_r(\omega)$) is defined as

$$T_r(\omega) = \frac{|V_{T-open}(\omega)|}{|p_a(\omega)|}, \tag{7.2}$$

with $V_{T-open}(\omega)$ the open circuit voltage produced by the transducer and $p_a(\omega)$ the pressure received on the transducer surface.

The transfer functions are calculated using the methods described by van Neer et al. [2007].

Setup

The experimental setup consisted of a water-filled tank. The array was attached to its sidewall. A calibrated source was mounted in a holder controlled by an xyz-system (see Fig. 7.4a). The source was a flat circular piston transducer (V310, Panametrics, Waltham, MA, USA, 2.25 MHz center frequency, diameter 6.35 mm).
For the transfer function measurements the source was excited by an arbitrary waveform generator (33250A, Agilent, Loveland, Colorado), which produced 600 cycle sine bursts with an amplitude of 5 V. Each array element was connected to a computer controlled matrix switch (custom built). The received signal was digitized by a digitizer card (DP235, Acqiris, Geneva, Switzerland) at a sampling rate of 100 MHz. The waveform generator was connected to a computer through GPIB, and the matrix switch was controlled using an Ethernet connection.
The acoustic pressures were low, so nonlinear propagation could be disregarded. Also attenuation was neglected, as the propagation distance in water was only $\sim$20 cm. The

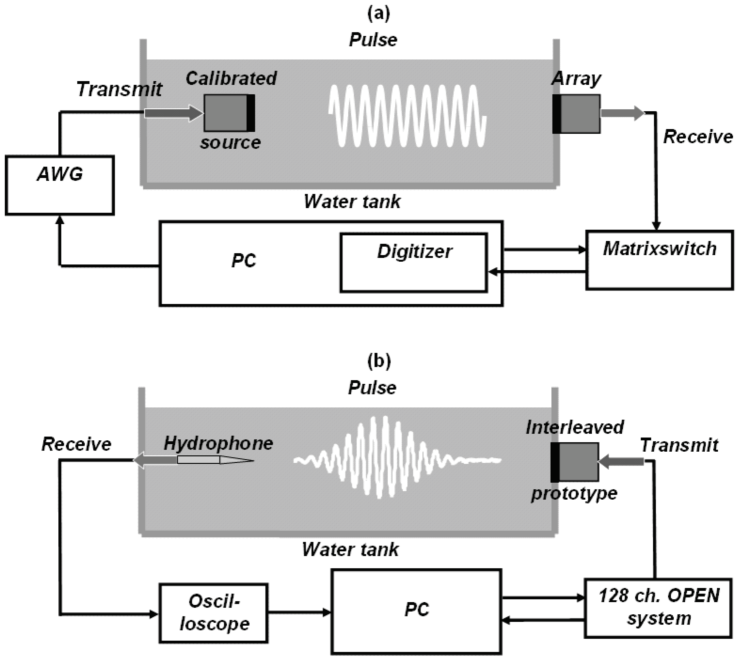

Figure 7.4: a) Setup to obtain transfer functions and SNR measurements. b) Setup to obtain beam profiles and crosstalk measurements.

exact diffraction correction function posted by Goldstein et al. [1998] was used to calculate on-axis pressures from the pressure produced at the source's surface. The elements of the high frequency subarray were 13 mm long in the elevation direction. The spatial averaging correction factor ($S(\omega)$) was calculated by simulating the complete wave over the elevation range (-6.5 to 6.5 mm) produced by the calibrated source at the axial distance ($\sim$23 cm) using Field II [Jensen and Svendsen, 1992, Jensen, 1996] and calculating the mean pressure. $S(\omega)$ was recalculated for the elements of the low frequency subarray, as their size was 16 mm x 0.2 mm.

7.4.2 Beam profiles and crosstalk measurements

Beam profiles of the final interleaved array transducer were measured with a hydrophone (diameter 0.2 mm, Precision Acoustics, Dorchester, UK) mounted in a xyz-system (see Fig. 7.4b). The elements of the low frequency subarray were excited by an eight cycle Gaussian apodized sine burst at 1 MHz and amplitude of 30 V, which was produced by a multi channel programmable ultrasound system (OPEN system, Lecoeur Electronique, Chuelles, France, first reported by Vignon et al. [2005]). The signals received by the hy-

drophone were digitized by an oscilloscope (9400A, Lecroy, Geneva, Switzerland) with a sampling frequency of 100 MHz and transferred to a computer for further processing. The electrical and mechanical crosstalk was measured by exciting an element of either the low frequency or the high frequency subarray by a 3 cycle Gaussian apodized sine burst at the element's resonance with an amplitude of 12 V_{pp}. The responses of all the elements were measured and recalculated for the open circuit case (V_{resp}^{open}). The crosstalk was defined as:

$$Crosstalk = 20\log(\frac{V_{resp}^{open}}{V_e}) \tag{7.3}$$

where V_e is the excitation voltage, which is measured over the electrodes of the excited element.

7.5 Results: interleaved array characteristics

7.5.1 Low frequency subarray

The transmit and receive transfer functions of both the low and high frequency subarrays are shown in Fig. 7.5. The average efficiency (defined in this article as the maximum of the transmit transfer function) of the elements of the low frequency subarray was ∼22 kPa/V (Fig. 7.5a). The average -10 dB bandwidth was 86%. After electrical tuning the average efficiency increased to ∼98 kPa/V (Fig. 7.5a). The -10 dB bandwidth was lowered from 86% to 55%. The transmit transfer function of the tuned elements shows that the efficiency of the third and fifth harmonics was respectively ∼46 dB and ∼55 dB below that of the fundamental.

Fig. 7.6 details the variation in element behavior by showing the normalized efficiency of the elements at resonance. The standard deviation of the normalized efficiency at resonance of the low frequency subarray was ∼1.9 dB (Fig. 7.6). The peak negative pressure reached ∼1.6 MPa at a focal distance of 6 cm, if the elements of the low frequency subarray were excited with a 2 cycle 1 MHz Gaussian apodized sine burst of amplitude 120 V_{pp}. The peak negative pressure reached 2.0 MPa, if a similar excitation signal 3 cycles in length was applied.

In Fig. 7.7 the normalized time pulse at focus is displayed, which was produced by exciting the elements of the low frequency subarray with a 2 cycle 1 MHz Gaussian apodized sine burst of amplitude 120 V_{pp}. The lateral focus of 6 cm was equal to the geometric elevation focus. The top panels show the fundamental and third harmonic components, the lower panels detail the fourth and fifth harmonics. The fundamental -6 dB pressure pulse length was ∼2.9 μs at focus, and it decreased to 1.7 μs, 1.4 μs and 1.3 μs for the third, fourth and fifth harmonics respectively. In Fig. 7.8a the lateral beam profiles of the fundamental up to the fifth harmonic recorded at a lateral focal distance of 6 cm (is equal to the geometric elevation focus) are presented. The lateral -6 dB beam width was 4.6 mm, 2.6 mm, 2.1 mm, 1.7 mm and 1.5 mm for the fundamental, second, third, fourth and fifth harmonic respectively. In Fig. 7.8b lateral beam profiles of the second, third and superharmonic components are displayed. The superharmonic component is defined as

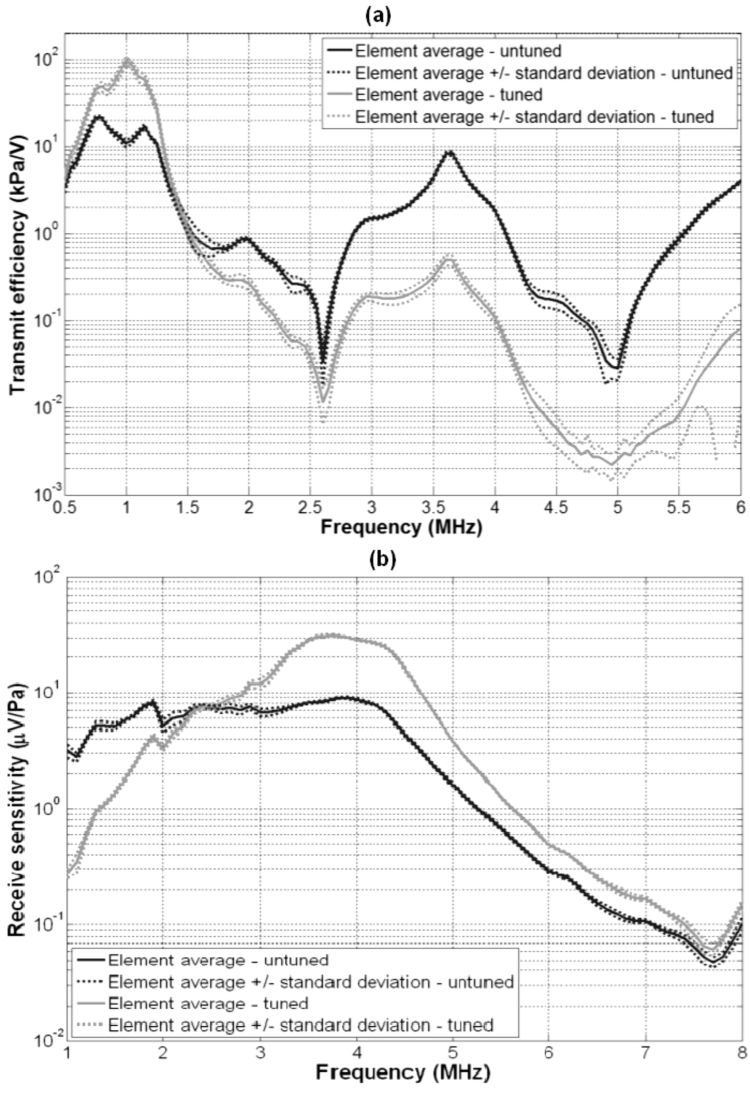

Figure 7.5: a) Transmit transfer function of the low frequency subarray, the mean and standard deviations are based on measurements of 8 elements. b) Receive transfer function of the high frequency subarray, the mean and standard deviations are based on measurements of 8 elements.

the combination of the third, fourth and fifth harmonics. The -6 dB beam width of the superharmonic was 1.9 mm.

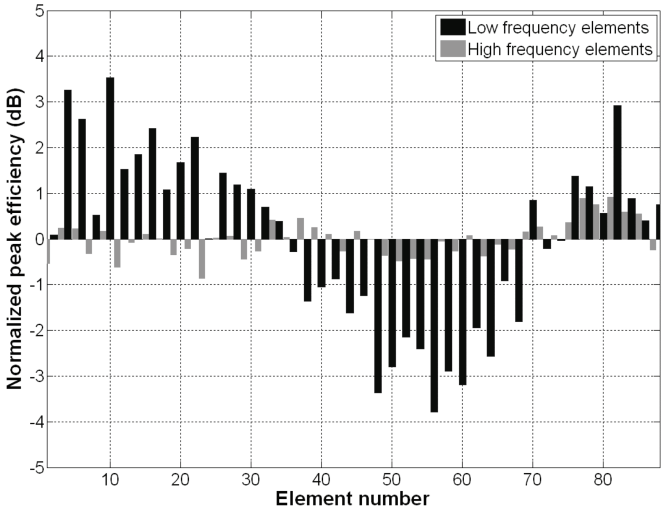

Figure 7.6: The element variation of both subarrays by showing the efficiency (defined as the maximum of the transmit transfer function). The efficiency was normalized to the mean efficiency of either the low or high frequency subarray.

7.5.2 High frequency subarray

The elements of the high frequency subarray had an average sensitivity (defined in this article as the maximum of the receive transfer function) of $\sim$9 μV/Pa, with a -10 dB bandwidth of 93% (Fig. 7.5b). After electrical tuning the average sensitivity increased to $\sim$31 μV/Pa. The -10 dB bandwidth of the elements was lowered from 93% to 50%. The standard deviation of the normalized efficiency at resonance of the high frequency part was $\sim$0.4 dB (Fig. 7.6). In transmission the untuned elements of the high frequency subarray had an average efficiency of $\sim$20 kPa/V.

7.5.3 Crosstalk

The inter-element crosstalk is shown in Fig. 7.9. Fig. 7.9a displays the crosstalk versus the element position relative to the excited element. The peak crosstalk amplitude was normalized by the excitation voltage. Fig. 7.9b shows the corresponding time delay. The mechanical crosstalk between the elements of the low frequency subarray ranged from -53 to -31 dB relative to the transmitted signal, depending on the distance between the active element and the element of interest (Fig. 7.9a). Notice the local minimum in the mechanical crosstalk 3 elements away from the excited element; this was caused by diffraction effects in the backing. The large standard deviations of the 4 elements closest

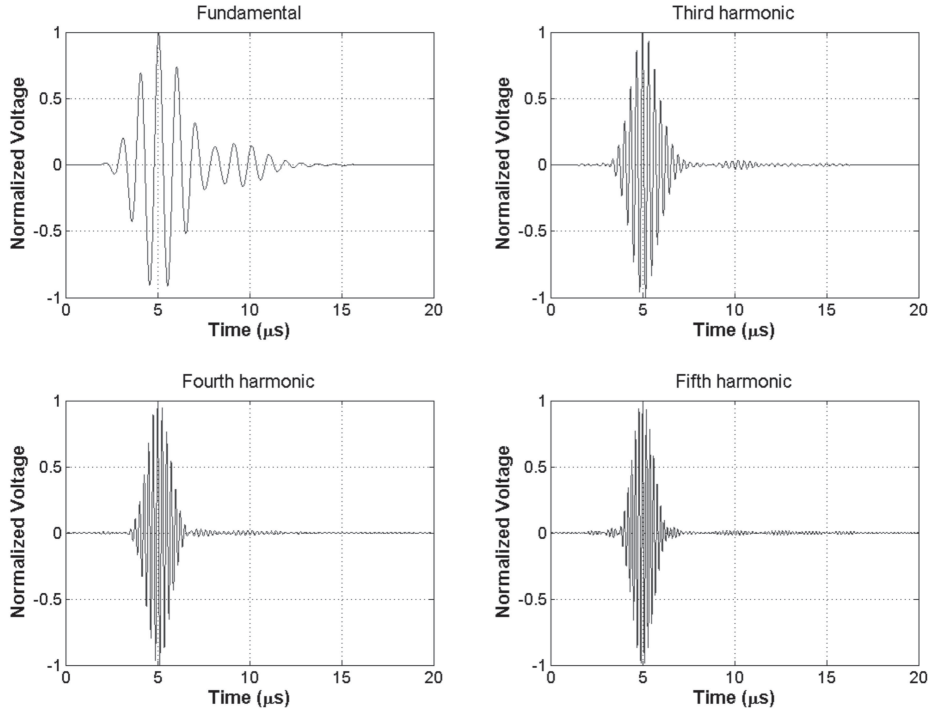

Figure 7.7: The normalized fundamental, third, fourth and fifth harmonic components of a pressure signal recorded at focus. The lateral focus of 6 cm was equal to the geometric elevation focus. The elements of the low frequency subarray were excited using a 2 cycle Gaussian apodized sine burst at 1 MHz with amplitude 120 V_{pp}.

to the excited element in Figs. 7.9a and 7.9b were caused by overlap and interference of electrical and mechanical crosstalk. The large standard deviation in time delay of the excited element in Fig. 7.9b was caused by clipping of the receive circuitry. The mean element-to-element travel distance of the pressure wave was 0.8 mm, as was calculated from the mean relative time delay of 0.47 μs between the peak values of the mechanical crosstalk of each element (Fig. 7.9b). The crosstalk between the elements of the low frequency subarray was not significant ($<$ -60 dB) for elements further away than 10, except for elements at a distance of 16. In this case the crosstalk was $\sim$-37 dB with a standard deviation of 5.0 dB compared to the excitation signal. The time delay between this element and the excited element was 0 μs implying purely electrical crosstalk. This crosstalk was explained by the wiring configuration.
Peak crosstalk from the low to the high frequency elements was $\sim$-60 dB relative to the transmitted signal with a standard deviation of 3.7 dB.

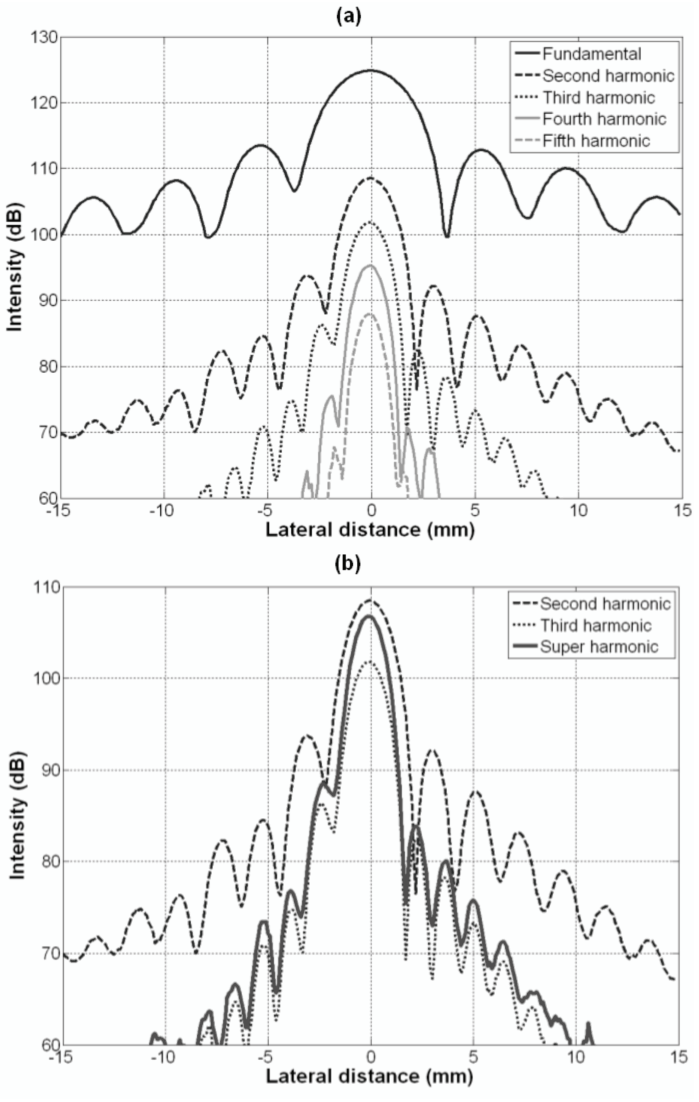

Figure 7.8: a) Lateral beam profiles of the fundamental up to the fifth harmonic at focus. The lateral focus of 6 cm was equal to the geometric elevation focus. The intensity values are relative to 1 Pa. The elements of the low frequency subarray were excited using an eight cycle Gaussian apodized sine burst at 1 MHz with amplitude 60 V_{pp}. b) Zoomed lateral beam profiles of the second, third and superharmonic component at focus. The lateral focus of 6 cm was equal to the geometric elevation focus.

7.6 Discussion

7.6.1 Performance of the interleaved array for SHI

The frequency response of the final interleaved array is shown in Fig. 7.10. Its combined -6 dB bandwidth exceeds 144%, whereas traditional arrays generally have 80% - 90% bandwidth. The graph summarizes the key characteristics of the implemented concept for the interleaved array in terms of bandwidth and efficiency.
The interleaved array consists of two separate subarrays, which are merged during manufacture. This is a critical step and improperly merged arrays suffer from high crosstalk levels.

The low frequency subarray used in transmission

The resolution of a B-mode picture is determined by such transmission beam characteristics as the length of the imaging pulse and the bundle profile. The effect of imaging schemes on the (axial) resolution is not treated, as it is considered to be out of the scope of this article.
The axial resolution is related to the time duration of the pressure pulses produced by the transducer (Fig. 7.7). Two main observations can be made. Firstly, the pulse lengths of the third, fourth and fifth harmonic are progressively shorter than the one of the fundamental. Secondly, the time trace of the fundamental is relatively long. This stems from the rather narrow bandwidth of the transmit transfer function of the tuned low frequency subarray (55% at -10 dB). Because of the intrinsic relation between the length of the fundamental pulse and the axial image resolution, it is highly desirable to increase the bandwidth. This goal can be achieved by either electrically tuning the low frequency subarray off resonance or by use of a multiple resonance circuit. Both methods exchange transmit efficiency for bandwidth, resulting in a lower peak pressure at focus - and, consequently, less energy in the higher harmonics - at the same excitation voltage. However, with the limited output voltage of our imaging system and a short excitation pulse of 2 cycles, the final interleaved array produced a maximum peak negative pressure of 1.6 MPa at focus. As this is below the MI limit of 1.9, the electrical tuning was not optimized further for bandwidth.
The lateral resolution is best investigated using lateral beam profiles (Fig. 7.8a). The profiles show the progressively smaller -6 dB beam width of the higher harmonics. The most striking is the superharmonic component shown in Fig. 7.8b: its on-axis intensity is almost equal to the second harmonic, but it has an off-axis energy distribution similar to the third harmonic. This decreases the so called haze in an image and by that improves the 2D image quality. The -6 dB superharmonic beam width is 59% smaller than the fundamental and 37% smaller than the second harmonic beam width. Similar values were reported by Bouakaz and de Jong [2003], who found the -6 dB beam width of the superharmonic component to be 50% smaller than the fundamental and 30% smaller than the second harmonic in nonlinear wave propagation simulations of circular symmetric transducers. However, this comparison is not completely suitable. It would be more ap-

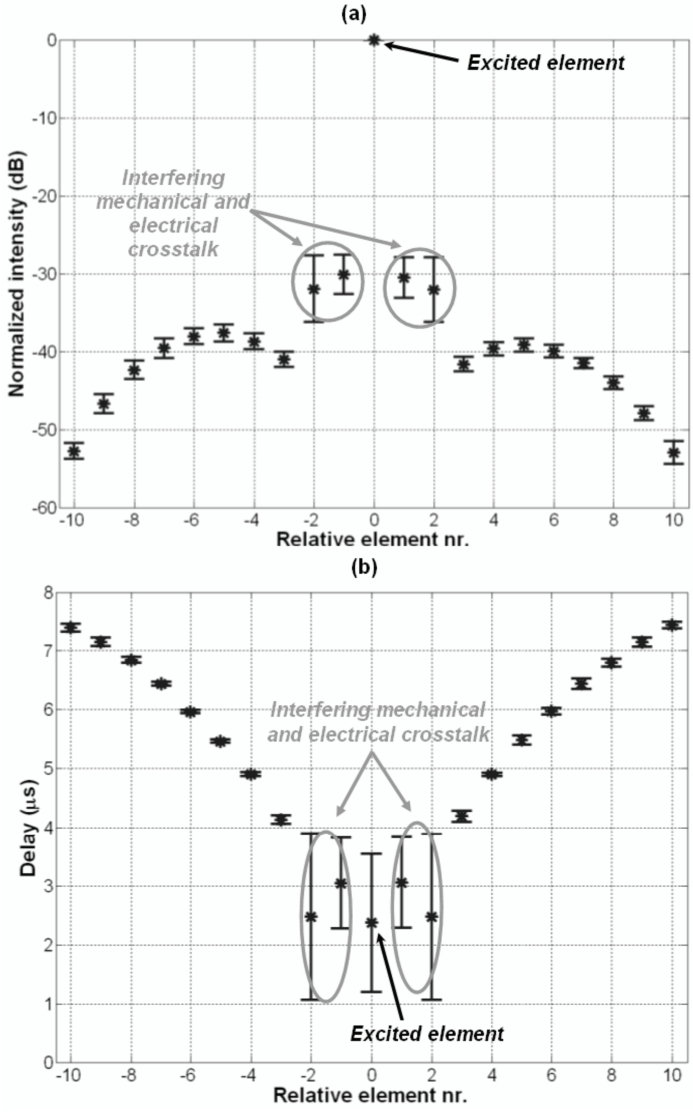

Figure 7.9: a) Peak element-to-element mechanical crosstalk of the low frequency subarray relative to the excited element. The average and standard deviation are based on measurements of 9 elements. b) Time delay of peak mechanical crosstalk of the low frequency subarray relative to the excited element. The average and standard deviation are based on measurements of 9 elements.

propriate to compare superharmonic beam profiles to the optimal second harmonic beam

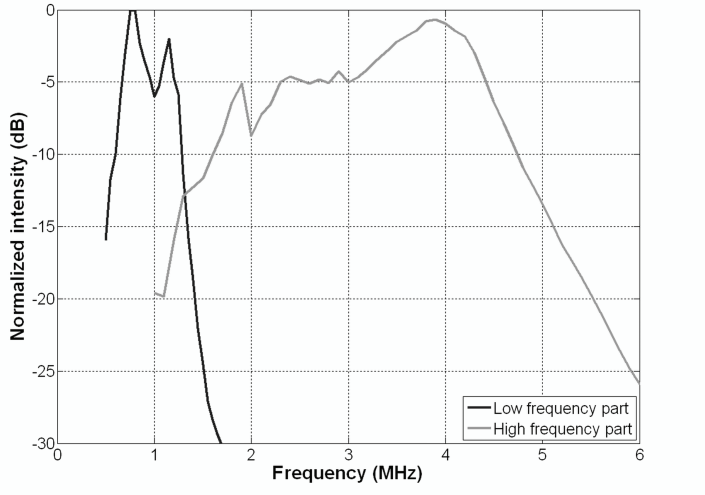

Figure 7.10: The transmission transfer functions of the untuned low and high frequency subarrays combined in order to illustrate the interleaved array concept. The transfer functions are normalized by the peak transmission transfer of the low frequency subarray.

profiles produced using a transmission frequency of 1.6 - 1.8 MHz [Kasprzak et al., 1999]. But the graph does demonstrate the potential of SHI, not only from a beam width perspective but also because of the lower off-axis energy of the superharmonic component at almost-equal-to-second-harmonic on-axis pressure intensity.

The high frequency subarray used in reception

Next to the characteristics of the transmission beam, the image quality is further affected by the sensitivity of the subarray used in reception and the noise characteristics of the imaging system. The untuned elements of the high frequency subarray had an average sensitivity of 9 μV/Pa, which is more than 50% less than that of the custom array made of the same piezomaterial (see Table 7.2). This is caused by the extra attenuation of the lens on the array and the optimization for very wide bandwidth. The final interleaved array in combination with the OPEN system can detect a pressure as low as 3 Pa with 10 dB SNR. By far the largest noise contribution (17 μV_{rms} over a 20 MHz band) originates from the OPEN system. To improve total system SNR, preamplifiers for each high frequency element could be added in the handle. The necessary circuitry will be relatively simple, as no high voltage protection circuitry is needed for the elements in SHI mode. Currently, the electrical tuning of the final interleaved array is optimized for SHI. The high frequency subarray is tuned on a single resonance, making the transducer plus circuitry quite narrowband (its -10 dB bandwidth is lowered from 93% to 50%). For SHI

broadband electrical tuning is preferable, such as using a matching circuit with multiple resonances distributed over the required pass band of 2.5 to 5.5 MHz. In both cases the phase response of the matching circuit should be taken into account as well. In the future programmable electrical tuning will be installed yielding a transducer capable of efficient second harmonic imaging and SHI.

Transducer generated SHI contaminants

As the energy of the superharmonics generated by either nonlinear propagation or UCA response is quite low, the contamination of the SHI component by transducer produced signals at these frequencies should be minimized. For this two transducer characteristics are essential. Firstly, the low frequency subarray should have a low efficiency at the superharmonic frequencies. Secondly, the crosstalk between the low and high frequency subarrays should be minimized.
The transmit transfer function of the tuned low frequency subarray showed that the third harmonic efficiency was $\sim$46 dB below its fundamental (Fig. 7.4a). The subarray's fifth harmonic efficiency was more than 55 dB lower than its efficiency at the fundamental. By using a Gaussian modulated sine burst with a center frequency at the low frequency elements' resonance with a -6 dB bandwidth similar to or slightly larger than the elements' fundamental band, the energy produced by the transducer at the third or fifth harmonic frequency can be kept $<$ -100 dB. Thus, although the energy of the third and fifth harmonic components due to either nonlinear propagation or UCA response is quite low, the energy content of spuriously transmitted odd harmonics by the array is negligibly low.
Crosstalk from the low to the high frequency elements was $\sim$-60 dB, due to the fact that the low and high frequency parts are in essence completely separate arrays. The high frequency elements are quite insensitive at the frequencies generated by the low frequency part during SHI and possible crosstalk artifacts in B-mode images are kept to a minimum. The crosstalk between the low frequency elements is important, because it has a detrimental influence on the transducer's ability to perform beam steering by effectively making the elements less omnidirectional. McKeighen [1998] reported that crosstalk values of -30 dB are considered acceptable for most imaging situations. Crosstalk between low frequency elements was $<$ -31 dB, so the interleaved array performed superior to this value.

Abdominal SHI

SHI is also suitable for abdominal imaging. As there is no size constraint on the array footprint in this application, the number of elements could be increased to 128; 64 elements used in transmission and 64 used in reception. In this case the footprint size would be 16 mm x 32 mm instead of the current 16 mm x 22 mm. Advantages of this modification would be an increased maximum lateral focal distance ($\sim$10 cm instead of the current $\sim$6 cm) and higher peak pressures at focus using equal excitation voltages. As the current interleaved array in conjunction with regular ultrasound equipment is already capable of reaching the 1.9 MI limit using a 3 cycle imaging burst, this means that the

array's fundamental compromise between efficiency and bandwidth would shift more to bandwidth.

7.6.2 Potential imaging methods

The final interleaved array is suitable for new UCA imaging techniques such as subharmonic imaging or SURF imaging due to its broad bandwidth. The role of each subarray changes for these imaging techniques. For subharmonic imaging, the high frequency elements are used in transmission and the low frequency elements in reception. In the case of SURF imaging, both element types are used in transmission and reception. To facilitate these different roles, the electrical tuning has to be changed and optimized for each application. A possible problem is the existence of grating lobes produced when transmitting using the high frequency elements. These grating lobes are caused by the fact that the subarray pitch of 0.5 mm is large relative to ultrasound wavelengths of 0.3 - 0.5 mm. For example, if a 4 MHz square wave is transmitted, a grating lobe of -10 dB relative to the main beam is located 45° off the main beam.
The following sections treat subharmonic and SURF imaging in combination with the final interleaved array, with the emphasis on usable imaging frequencies and grating lobes.

Subharmonic imaging

First of all, the frequencies necessary for subharmonic imaging in cardiac applications are discussed in relation to the transfer function of the final interleaved array. Chomas et al. [2002] reported that the best subharmonic response is produced - while minimizing bubble instability - by using a transmission frequency which is twice the UCAs resonant frequency. UCAs used for cardiac applications are resonant at 1 - 5 MHz [Dawson et al., 1999]. The final interleaved array is suitable for subharmonic imaging of UCAs with resonance frequencies between 1 - 2.4 MHz, as the high frequency subarray is efficient up to $\sim$4.8 MHz (see Fig. 7.10). Depending on the frequency of the subharmonic component either the low or high frequency subarray should be used in reception.
The other topic of discussion is the influence of grating lobes. There exists an onset pressure threshold for the production of subharmonics by UCA. Below this threshold no subharmonic component can be detected. Chomas et al. [2002] reported a pressure threshold of 200 kPa. By keeping the peak pressure in the grating lobe below this threshold, only the UCA in the main beam will produce significant subharmonic response. In this case, the existence of grating lobes can be disregarded. This implies that there is a frequency dependent maximum of the peak pressure in the main beam. To study the aforementioned relation we investigated the appearance of grating lobes in the acoustic field produced by the final interleaved array at varying transmission frequencies using the FIELD II simulation program [Jensen and Svendsen, 1992, Jensen, 1996]. The element size was 13 mm x 0.2 mm with a subarray pitch of 0.5 mm. The simulations were performed using 3 cycle sine bursts, which were Gaussian apodized. The geometric elevation focus of the beam was 6 cm, but no lateral focus was applied. The beam was steered 35° and the

propagation medium was assumed to be lossless. In Fig. 7.11a a graph is shown detailing the peak intensities of the simulated grating lobe versus the transmission frequency and in Fig. 7.11b the angle of the grating lobe is shown versus the transmission frequency. From Fig. 7.11a can be deduced that the maximum peak pressures of the main beam for subharmonic imaging reduce from 600 kPa at 2.5 MHz to 360 kPa at 4.5 MHz. These pressures are common for nondestructive UCA imaging. The actual pressure threshold value for the generation of subharmonics depends on the bubble type and the excitation frequency. Typical threshold values for free gas bubbles are around 60 kPa, if excited at twice the bubbles' resonance frequency [Eller and Flynn, 1969]. For UCAs, such as Levovist®, Optison®, Definity® and Sonazoid®, threshold values around 300 kPa were reported [Frinking et al., 2009]. For SonoVue® the subharmonic pressure threshold was found to be 40 kPa [Biagi et al., 2007].

SURF imaging

Firstly, the frequencies necessary for SURF imaging in cardiac applications in relation to the transfer function of the final interleaved array are discussed. Masoy et al. [2008] state that the difference between the low and high frequency bursts should be on the order of 7 - 10 times for SURF imaging. In the case of echocardiography this would imply a low frequency pulse of $\sim$0.6 MHz and a high frequency pulse of $\sim$4 - 5 MHz. The combined bandwidth of the interleaved array is sufficient for SURF imaging, albeit at relatively low frequencies. For example, if a manipulation pulse of 0.6 MHz is used, an imaging pulse of $\sim$4.2 MHz could be used. As the manipulation pulse pressures are usually in the order of 50 - 100 kPa [Masoy et al., 2008], the normalized -10 dB transmit efficiency of the untuned low frequency subarray at 0.6 MHz (Fig. 7.10) is sufficient.
Secondly, the effect of grating lobes on SURF imaging is discussed. It turns out that grating lobes caused by transmitting at higher frequencies are of minor importance for SURF imaging. Although the high frequency imaging pulse ($\sim$5 MHz) used in SURF would produce significant grating lobes, the low frequency manipulation pulse ($\sim$0.7 MHz) used to alter UCA scattering properties would not. Therefore, the final image subtraction step used in SURF imaging removes the UCA response from the grating lobes of the high frequency imaging pulse.

Other possibilities

Although the details are not covered in this article, the interleaved array is also suitable for other advanced imaging techniques. Examples are source prebiasing to reduce tissue harmonics in UCA imaging [Christopher, 1999] or third harmonic transmit phasing to either enhance the tissue second harmonic - in tissue imaging - or reduce the tissue second harmonic - in UCA imaging - [Shen et al., 2007a].

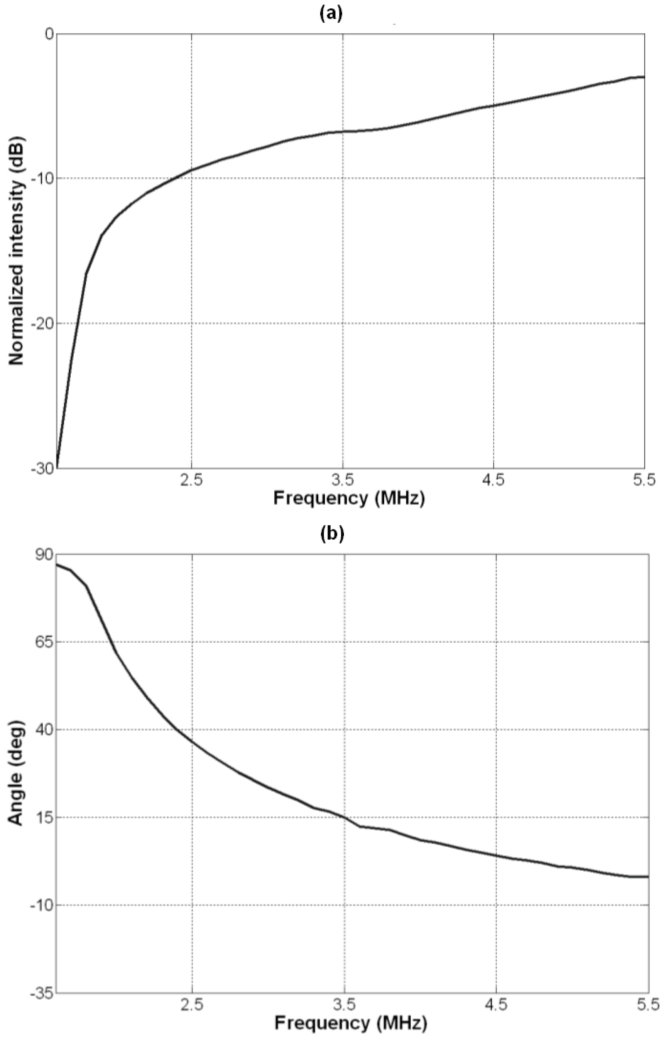

Figure 7.11: a) The relation between the fundamental peak grating lobe intensity versus the transmission frequency, simulated for the final interleaved array using Field II. The grating lobe intensity was normalized by the main fundamental beam peak intensity. The element size was 13 mm x 0.2 mm with a subarray pitch of 0.5 mm. The simulations were performed using 3 cycle sine bursts, which were Gaussian apodized. The geometric elevation focus of the beam was 6 cm, no lateral focus was applied. The beam was steered 35° and the propagation medium was assumed to be lossless. b) The angle of the grating lobe versus transmission frequency. The beam was steered 35°.

7.7 Conclusion

The interleaved array presented in this article possesses optimal characteristics for tissue and UCA enhanced SHI. Moreover, this array is suitable for a wide range of other experimental and clinical imaging modalities, such as second harmonic, subharmonic, and SURF imaging.
With considerably less variation in response over the elements, much lower element-to-element crosstalk, a higher fundamental transmission efficiency, reduced third and fifth harmonic transmission efficiency, and improved sensitivity in reception, the interleaved array described in this article is a large improvement over the array reported by Bouakaz et al. [2004].

Acknowledgements We would like to thank W. van Alphen, G. Springeling, J.M.G. Borsboom, C. Pakvis, J.E.T. van Wamel, J.G. Bosch and T.R. Shrout for their efforts.

Table 7.2: Custom array performance parameters

Custom array ID	Material type	Resonance frequency (f_r)	$T_r(f_r)$: μ	$T_r(f_r)$: σ	Bandwidth at -6 dB	$T_t(f_r)$: μ	$T_t(f_r)$: σ	$\lvert Z(f_r)\rvert$	$\angle Z(f_r)$	SNR if receiving 1 Pa wave
		[MHz]	[μV/Pa]	[μV/Pa]	[%]	[kPa/V]	[kPa/V]	Ω	[$^\circ$]	[dB]
1	CTS 3203HD	3.2	21	0.8	41	32.5	1	440	-18	24
2	Ferroperm Pz29	3.1	10.6	1.1	43	15.8	1.3	530	-36	16
3	Morgan PZT5K1	3.4	13.7	1.3	41	20.5	2.1	450	-22	17
4	TRS PZT HK1HD	3.6	14.4	0.4	47	31.1	1.1	330	-17	18
5	CTS 50-50 composite	3.3	7	1.2	51	4.6	0.8	440	-77	14
6	CTS 60-40 composite	3.3	3.3	0.6	68	1.8	0.3	470	-86	3
7	Omega PZNT	1.6	15.6	3.8	48	5.5	1.8	850	-45	11
	after repoling	2.0	15.6	3.7	45	7	2	800	-38	1
8	TRS PMN-30%PT	3.4	5.5	0.8	46	5.9	1.1	340	-50	18
	after repoling	3.4	12.6	0.7	47	16	1.2	380	-35	15

CHAPTER 8

Optimization of a phased array transducer for multiple harmonic imaging in medical applications : Frequency and topology

G.M Matte, P.L.M.J. Van Neer, M. G. Danilouchkine, J. Huijssen, M.D. Verweij, N. de Jong

Submitted to IEEE transactions on UFFC (March 2010)

Abstract Second harmonic imaging is currently one of the standards in commercial echographic systems for diagnosis because of its high spatial resolution and low sensitivity to clutter and near-field artifacts. The use of nonlinear phenomena mirrors a great set of solutions to improve echographic image resolution. To further enhance the resolution and image quality the combination of the third to fifth harmonics dubbed the superharmonics could be used. However, this requires a bandwidth exceeding that of conventional transducers. A promising solution features a phased array design with interleaved low and high frequency elements for transmission and reception respectively. As the amplitude of the backscattered higher harmonics at the transducer surface is relatively low, it is highly desirable to increase the sensitivity in reception. Therefore, we investigated the optimization of the number of elements in the receiving aperture as well as their arrangement (topology). A variety of configurations was considered, including one transmit element for each receive element (1/2) up to one transmit for 7 receive elements (1/8). The topologies are assessed based on the ratio of the harmonic peak pressures in the main and grating lobes. Further, the higher harmonic level is maximized by optimization of the center frequency of the transmitted pulse. The achievable signal-to-noise-ratio (SNR) for a specific application is a compromise between the frequency dependent attenuation and nonlinearity at a required penetration depth. To calculate the

SNR of the complete imaging chain, we use an approach analogous to the SONAR equation used in underwater acoustics. The generated harmonic pressure fields due to nonlinear wave propagation were modeled with the Iterative Nonlinear Contrast Source (INCS) method, the KZK or the Burgers equation. The optimal topology for superharmonic imaging was an interleaved design with 1 transmit element per 7 receive elements. It improves the SNR by $\sim$5 dB compared to the interleaved (1/2) design reported by Bouakaz et al. Bouakaz et al. [2004] and van Neer et al. van Neer et al. [2010]. The optimal transmission frequency for superharmonic echocardiography was found to be 1.0 1.2 MHz. For superharmonic abdominal imaging this frequency was found to be 1.7 1.9 MHz. For second harmonic echocardiography the optimal transmission frequency of 1.8 MHz reported in the literature was corroborated with our simulation results.

8.1 Introduction

Since its introduction in the late 90s, tissue second harmonic imaging of biological tissue has become the de-facto standard in commercial echographic systems for medical diagnosis. The method is based on the selective imaging of the second harmonic frequency [Averkiou et al., 1997, Thomas and Rubin, 1998]. Compared to fundamental tissue imaging, tissue second harmonic imaging has a higher lateral resolution and lower sidelobes, and is, therefore, less sensitive to clutter and off-axis scatterers [Ward et al., 1996, Shapiro et al., 1998, Tranquart et al., 1999, Humphrey, 2000a, Bouakaz and de Jong, 2003]. Also, since the second harmonic field builds up progressively, the effects of reverberation and near-field artifacts are greatly reduced [Tranquart et al., 1999, Bouakaz and de Jong, 2003]. Recently, Bouakaz et al. [2002a] introduced a novel ultrasonic tissue imaging method dubbed superharmonic imaging (SHI) Bouakaz et al. [2002a], Bouakaz and de Jong [2003]. This technique combines the third to fifth harmonics to construct an image. Tissue SHI efficiently suppresses near-field artifacts, reverberations, and off-axis artifacts in addition to the enhanced lateral and axial resolution. The resulting images showed more details than those produced by second harmonic imaging Bouakaz and de Jong [2003]. However, one of the challenges in SHI is the very wide bandwidth requirement ($> 130\%$) for the array used to transmit at the fundamental and receive the third to fifth harmonic signals.

An approach for having such a very wide band transducer is to use capacitive Micromachined Ultrasound Transducers (cMUTs). CMUTs having a -6 dB bandwidth of 130% have been reported [Mills, 2004, Zhou et al., 2005]. However, cMUTs are held back by challenges such as achieving high output pressures [Yaralioglu et al., 2006], their inherent nonlinearity and relatively high crosstalk [Zhou et al., 2005]. The most important drawback of cMUTs for tissue SHI is their nonlinearity at high output pressures. The level of the higher harmonics generated by nonlinear propagation is low, thus any transmission of harmonics due to device nonlinearity will considerably reduce the dynamic range of the imaging system. The other way to obtain a transducer with sufficient bandwidth is to further improve the current transducer technology. However, the 130% bandwidth necessary for SHI is considerably larger than that achievable with conventional arrays. Although -6 dB bandwidths as high as 140% are reported in the literature for single element transducers made from a 1-3 single crystal-epoxy composite, the actual peak bandwidth at -6 dB reported for single crystal arrays are in the order of 95% [Rehrig et al., 2003, Zipparo et al., 2004, Li et al., 2007] not sufficient for SHI. Thus, in order to accommodate the bandwidth requirement for SHI, the transmit and receive elements need to be separated. Such an approach has been proven to be viable and has been intensively treated in the scientific literature [Hossack and Auld, 1993, Hossack et al., 2000, Zhou and Hossack, 2002, Bouakaz and de Jong, 2003, Bouakaz et al., 2004, Akiyama et al., 2006, Ferin et al., 2007, van Neer et al., 2010]. A short overview of the earlier proposed solutions is given in the following paragraphs.

The first solution comprises a stacked topology. In this design two active PZT layers with different resonance frequencies are placed on top of each other [Hossack and

Auld, 1993, Hossack et al., 2000, Zhou and Hossack, 2002]. Thus the total surface used for transmission and reception remains the same as in a conventional phased array. Advantages of this configuration are the limited total footprint of the array and the ease of manufacturing. The difficulty of using such a configuration comes from the electromechanical and acoustical coupling between the active layers. This causes troughs in the frequency response of the transducer due to destructive interference in the active layers, if the resonance frequencies of both layers are close to each other. Although solutions have been presented in literature, they require either fairly complicated electronics or knowledge of the phase transfer function of each element [Hossack and Auld, 1993, Zhou and Hossack, 2002]. Moreover, the matching layer characteristic is compromised, since it should match for two different resonance frequencies. A stacked topology for a single element has been described by Akiyama et al. Akiyama et al. [2006]. Their design comprises an ultra wide band transducer used in a mechanical sector scanner. It features a PZT layer for transmission and a PVDF layer for reception. To obtain very wide bandwidth the PVDF layer functions below its resonance frequency. This has the added benefit of guaranteeing electromechanical decoupling between the active layers. However, the sensitivity of PVDF used in this manner is generally low. Another option is to use a horizontal stack topology, where two low frequency arrays are positioned in the elevation direction on both sides of a central high frequency array [Ferin et al., 2007]. The main advantage of this approach is that the initial performance of both arrays is not modified, thus facilitating manufacture. Disadvantages are the limited overlap of the acoustic beams constricting the imaging range and the increased footprint in elevation direction.

A final possibility is to arrange the transmit and receive elements in the lateral direction. Bouakaz et al. Bouakaz and de Jong [2003], Bouakaz et al. [2004] proposed to interleave two arrays distributing the transmit and receive elements alternately. With this configuration the transmit and receive beams overlap fully. Also, its footprint remains small and the transmit and receive elements can be optimized for their specific roles. Drawbacks are the relatively complicated manufacturing process and the intrinsically reduced sensitivity as only half the elements are used in reception and transmission. For transmission the reduced efficiency can be compensated by increasing the amplitude.

The interleaved design is chosen in our project. It has fully overlapping beams and a low foot print. Also, there is no direct electromechanical coupling between the elements, since the acoustic stacks for transmission and reception including the associated circuitry are fully separated. Next to the initial interleaved array design reported by Bouakaz et al. Bouakaz et al. [2004], a follow-up interleaved array intended primarily for SHI and optimized for echocardiography was reported by Van Neer et al. van Neer et al. [2010]. In the paper the rationale behind the element geometry, frequency and material choice was reported and performance measurements were provided van Neer et al. [2010]. However, in the current paper the interleaved design of alternate transmit and receive elements is further investigated. Redistributing the transmit and receive elements in groups or changing the ratio of transmit-to-receive elements may considerably improve the receive efficiency whilst a high quality beam is retained. This is important for tis-

sue SHI, as the level of the higher harmonics generated by nonlinear propagation is low. Moreover, the paper by van Neer et al. van Neer et al. [2010] only basically covers the choice for the 1 MHz transmit frequency used for the interleaved array optimized for superharmonic echocardiography. The optimal transmit frequency for tissue SHI depends on the level of the third to fifth harmonics at the distances determined by the application. Consequently, the level of these harmonics is determined by two competing phenomena nonlinear propagation and attenuation. To the authors knowledge no systematic study of the optimal transmit frequency for SHI versus the imaging distance determined by the application has been conducted.

The first aim of the manuscript is to investigate the optimal transmit frequency for second harmonic imaging and SHI depending on the imaging application domain. The second aim of this paper is to optimize the distribution of the transmit and receive elements in groups or by changing the ratio of transmit-to-receive elements in order to maximize the receive sensitivity whilst retaining a high quality ultrasound beam.

8.2 Research directions

8.2.1 Transmission frequency optimization

The first part of the paper focuses on the optimization of the transmission frequency for multiple harmonics imaging, initially for echocardiography but also extended to the different imaging ranges associated with other applications. In order to study the best possible compromise between the level of the third to fifth harmonics received and the penetration depths associated with different applications the transmit frequency has to be optimized. For this we modify the SONAR equation widely used in underwater acoustics for transducer design [Lurton, 2002] to medical imaging purposes. This equation describes the whole pulse-echo imaging chain including transmit equipment, nonlinear wave propagation, backscattering and receive equipment. The levels of harmonics generated during the propagation of sound through tissue are calculated by two analogous methods described later.

8.2.2 Topology optimization

The other part of the paper focuses on the optimization of the lateral distribution of the transmit and receive elements in order to improve the receive efficiency whilst retaining a high quality ultrasound beam.
First we analyze an array where the ratio of transmit and receive elements is 1. The array with N elements is then divided in 2, 3 or N groups. So each group has $N/2$, $N/3$ or 1 elements. The former cases are referred to as group topology, and the latter case is referred to as interleaved or mixed topology. After this the effects of lowering the ratio of transmit-to-receive elements is studied in order to increase the receive sensitivity. The decrease in transmission efficiency can be compensated by higher electrical transmission amplitude. For the analyses we used simulations based on Field II [Jensen and Svendsen,

1992, Jensen, 1996] in combination with the Burgers equation [Cobbold, 2007] and the INCS method (Huijssen, Verweij et al. 2006; Huijssen, Verweij et al. 2008; Huijssen and Verweij 2009; Huijssen and Verweij 2010)[Huijssen et al., 2006, 2007, Huijssen, 2008, Verweij and Huijssen, 2009](update reference).

8.2.3 Group topology

In the first configuration of the group topology class the array is constituted of two equal groups of elements distributed laterally (see 8.5a). The transmit elements (tuned on the fundamental frequency) are on one side of the array, while the receive elements (tuned on higher frequency components) are on the other side. The origin of the coordinate system of the probe is located in between both groups of elements.
The second type of the group topology defines an array consisting of three parts in a lateral distribution (see Fig. 8.5b). A group of transmit elements is located in the middle and two groups of receive elements are laterally arranged on each side of the transmit elements. The total number of receive elements is twice the amount of transmit elements. This configuration is analogous to the one described by Ferin Ferin et al. [2007], except in our case the lateral arrangement of the elements enables electronic focusing instead of a fixed focus. The transmit and receive elements are distributed symmetrically, thus the convolved transmit and receive beams are expected to be symmetric.

8.2.4 Interleaved topology

The interleaved topology is an array configuration where single transmit elements are equidistantly placed over the footprint (see 8.5c-e). The successive transmit elements are interleaved by a group of n receive elements ($n = 1$ to N). We further refer to $1/k$ interleaved topology to make distinction between each particular combination of a single transmit element and ($n = k - 1$) receive elements. The main difference between the introduced topology classes lies in the fact that transmit elements are grouped together to form the transmit aperture in the group topology class. The perceived advantage of the interleaved over the group topology is the possibility of increased sensitivity in reception whilst having the best distribution of the elements from a beam quality perspective. According to the nomenclature established in the current paper, the transducer design described by Bouakaz et al. Bouakaz et al. [2004] and van Neer et al. van Neer et al. [2010] belongs to the 1/2 interleaved topology. Figure 2 describes some interleaved topologies(update reference to figure).

8.2.5 Criteria for topology evaluation

Of major importance in the design of phased arrays for medical ultrasound is the system dynamic range. It is limited by the relative energy difference between the main and the grating lobes and by the signal-to-noise ratio (SNR). A grating lobe is the result of constructive interference of the acoustic waves produced by the array at a sideways

direction. The backscattered echoes originating from a grating lobe pollute the signal of the main beam. The grating lobes are caused by the under-sampling of the physical aperture. Considering a phased array as a sampled aperture and taking into account the Nyquist theorem, it is easy to deduce that a grating lobe would occur when the distance between neighboring elements of the array exceeds half of the wavelength of the emitted pulse. Thus, the presence of a grating lobe and its intensity depend on the wavelength and the pitch. Obviously to avoid the occurrence of grating lobes, the interelement spacing should be equal to or less than the abovementioned distance. In case of harmonic imaging this requirement can be weakened, as the production of the nth harmonic is related to the pressure in the beam to the power n the peak pressure in the main beam will be considerably higher than the pressure in the grating lobe. The pressure in the grating lobe relative to the pressure in the main beam at the frequency used to construct an image sets a limit on the dynamic range of that image. Cobbold Cobbold [2007] states that the grating lobe pressure should be 40 dB below the pressure in the main beam.

To evaluate the effect of the varying distance between elements for each topology, the levels of a harmonic in the main and grating lobe have to be calculated and compared with each other. All further analyses will be backed by simulations based on the KZK equation [Lee and Hamilton, 1995] and the INCS method [Huijssen et al., 2006, 2008, Verweij and Huijssen, 2009], as well as Field II [Jensen and Svendsen, 1992, Jensen, 1996] in combination with the Burgers equation [Cobbold, 2007].

8.3 Theory

8.3.1 Expression of the SNR

The SNR can be expressed as a logarithmic sum of transfer functions affecting the signal, each representing a phenomenon of the imaging process:
In general the SNR can be expressed as :

$$SNR(\omega) = V + Te(\omega) + H_{FRWD} - Bs(\omega) - H_{BKWD} - Hs(\omega) - Ns, \quad (8.1)$$

with

V excitation amplitude on the transducer clamps,

Te the transmit efficiency, analogous to TVR (Transmitting Voltage Response) in underwater acoustics

H_{FRWD} the function describing the pressure wave during forward propagation. It includes diffraction, the focal gain, attenuation and nonlinearity

Bs Bs corresponds to the loss of power during the backscattering process. It is analogous to the target strength in underwater acoustics.

H_{BKWD} the function describing the pressure wave during back propagation. By assuming linear back propagation, it includes only frequency dependent attenuation (A). Backscattering is assumed to be spherical. The diffraction term is assumed to be negligible on the back propagation.

Hs the receive sensitivity of the transducer.

Ns the noise of the imaging system.

This expression is analogous to the SONAR equation, widely used in underwater acoustics for transducer design ([Lurton, 2002]). The combination of V, Te and H_{FRWD} is the incoming pressure at the scatterer location. Thus, 8.1 can be rewritten into:

All the factors in equation 8.1 are expressed in dB.

$$SNR(\omega) = P(\omega) + Bs(\omega) + A(\omega) - Hs(\omega) - Ns, \tag{8.2}$$

with

P the incoming pressure at the scatterer location, by forward propagation of the ultrasound produced by the transducer

A ultrasound attenuation during linear back propagation to the transducer

ω the angular frequency

All the factors in 8.1 and 8.2 are expressed in dB. Fig. 8.1 provides a schematic for the concept of the expression of the SNR. The terms in (8.2) are explained in more detail in the following paragraphs.

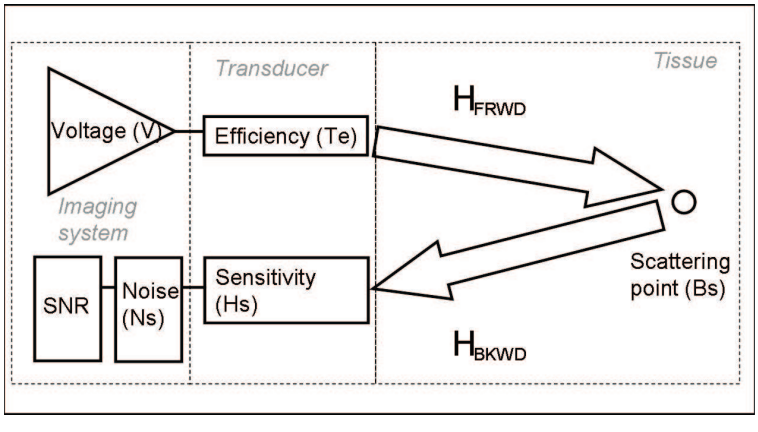

Figure 8.1: Schematic description of the expression of the SNR

The excitation voltage (V)

The excitation voltage (V) over the clamps of the transmitting part of the transducer is expressed in dB relative to 1 volt.

The transmit efficiency (T_e)

The transmit transfer (T_e) is defined as [van Neer et al., 2007]:

$$T_e = \frac{|p_0|}{|V_T|}, \tag{8.3}$$

with p_0 the pressure at the transducer surface and V_T the voltage over the transducer electrodes. T_e is expressed in dB relative to 1 Pa/V.

The backscattered signal (Bs)

The total backscattered intensity (Bs) is defined as:

$$Bs = \Omega \mu_t L, \tag{8.4}$$

where Ω is the solid angle, impinging the receive aperture of the transducer for a given observation point. The area of the receive aperture is simply determined as a product of an element area and the number of elements in reception. L defines the scattering distance, which is equal to the distance between the observation point and the transducer, and μ_t the backscattering cross-section which is modeled as [Duck, 1990]:

$$\mu_t = \mu_a f^{\mu_b}, \tag{8.5}$$

with f the frequency.
Bs is expressed in dB.

The incoming pressure at the scatterer location by forward propagation (P)

For nonlinear propagation the acoustic wave at the transducer surface has to be propagated towards the scatterer location. We use two simulations models: the KZK equation (Hart and Hamilton 1988; Lee and Hamilton 1995; Hamilton and Blackstock 1998) and the INCS approach(Huijssen, Verweij et al. 2006; Huijssen, Verweij et al. 2008; Huijssen and Verweij 2009; Huijssen and Verweij 2010). These models include the attenuation of the medium. (update references) P is expressed in dB relative to 1 Pa.

Attenuation of backscattered signal during backpropagation (A_{back})

The amplitude of the backscattered signal is generally low, thus the backward propagation can be considered to be linear. The attenuation of the backscattered signal during

linear propagation of the backscattered signal from the tissue target to the transducer (A_{back}) was modeled as

$$A_{back} = L \cdot \alpha_0 \cdot f^b, \tag{8.6}$$

with α_0^f the frequency attenuation factor. A_{back} is defined per harmonic n in dB.

The receive transfer (H_s)

The receive transfer (H_s) is defined as [van Neer et al., 2007]:

$$H_s = \frac{|V_{T-open}|}{|p_a|}, \tag{8.7}$$

with V_{T-open} the open circuit voltage over the transducer and p_a the pressure received on the transducer surface.
H_s is expressed in dB relative to 1 V/Pa.

Transducer and system noise (Ns)

The transducer and system noise (Ns) was expressed in dB relative to 1 V_{RMS}. The noise is assumed to be white. As the SNR is considered after beamforming, the noise level is divided by $\sqrt{N_{el}}$.

8.3.2 The KZK equation

The cumulative effects of diffraction, absorption and nonlinearity in directive sound beams are modeled by the KZK nonlinear wave equation [Averkiou et al., 1997, Cobbold, 2007]. The KZK equation uses the parabolic approximation and is therefore only valid for 15 degrees around the direction of the wave propagation.

$$\frac{\partial^2 p}{\partial z \partial t'} = \frac{c_0}{2}\left(\frac{\partial^2 p}{\partial r^2} + \frac{1}{r}\frac{\partial p}{\partial r}\right) + \frac{\alpha_0}{\omega_0^2}\frac{\partial^3 p}{\partial t'^3} + \frac{\beta}{2\rho_0 c_0^3}\frac{\partial^2 p}{\partial t'^2}, \tag{8.8}$$

With p the sound pressure, t the retarded time defined as $t' = t - \frac{z}{c_0}$, c_0, c_0 the small-signal acoustic velocity, r the transverse radial coordinate, α_0 the thermoviscous attenuation coefficient, ω_0 the angular frequency of the fundamental, β the coefficient of nonlinearity and ρ_0 the ambient density. The first term on the right-hand side of 8.8 accounts for diffraction, the second term accounts for absorption and the third term accounts for quadratic nonlinearity. To mimic tissue absorption the absorption term was replaced with an attenuation term which depended linearly on the frequency [Bouakaz and de Jong, 2003]. Equation 8.8 is written using cylindrical coordinates, which implies axi-symmetry also in the source and it uses a paraxial approximation. The well known time domain approach proposed by Lee and Hamilton was implemented [Hart and Hamilton, 1988, Lee and Hamilton, 1995, Hamilton and Blackstock, 1998]. The KZK equation has been utilized by many researches and is in excellent agreement with experiments [Tjotta et al., 1990, 1991].

8.3.3 The INCS method

A second order approximation of the nonlinear propagation of acoustic waves in a homogeneous medium is given by the Westervelt equation [Hamilton and Blackstock, 1998].

$$\frac{1}{c_0}\frac{\partial^2}{\partial t^2}[\chi(t) *_t p] - \nabla^2 p = S + \frac{\beta}{\rho_0^3 c_0^4}\frac{\partial^2 p^2}{\partial t^2}, \tag{8.9}$$

with $\chi(t)$ a normalized compressibility relaxation function, $*_t$ the convolution with respect to time and S the primary source term. The usual prescription of a pressure $P(x, y, t)$ at the boundary $z = 0$ can be accounted for by using $S = -\partial[F(x, y, t)\delta(z)]/\partial z$, where $F = 2P(x, y, t)$ is the surface force density in the positive z-direction and $\delta(z)$ is the Dirac delta function. The details about the theoretical background of the method can be found in the works of Huijssen et al. [Huijssen et al., 2006, 2007, Verweij and Huijssen, 2009]. The INCS method provides a numerical solution for this equation and is not dependent on the direction of the wave propagation. The strategy to solve this equation is to consider the nonlinear pressure field as a sum of the linear field solution and a nonlinear correction. The linear field solution can be obtained from the homogeneous lossy and linear background medium with external source S. The nonlinear field correction arises from the solution of equation 8.9 with the single second term on the right hand side. Those solutions are numerically refined in an iterative manner until convergence [Huijssen, 2008]. The non quadratic attenuation of lossy media like tissue was incorporated [Huijssen, 2008]. In contrast to the KZK simulations the INCS method does not require a paraxial approximation.

8.3.4 Linear acoustic modeling using Field II

The FIELD II simulation program [Jensen and Svendsen, 1992, Jensen, 1996] was used to calculate the fundamental acoustic fields of the various group configurations and mixed configurations. The Burgers equation was used in order to estimate the harmonic level in the grating lobes.

8.3.5 The Burgers equation

The Burgers equation describes the propagation of finite-amplitude plane progressive waves in a classic viscous loss medium. The solution was found as a complex Fourier series using the iterative computation scheme given by Cobbold [2007].

8.4 Material and Methods

8.4.1 Frequency optimization

Nonlinear propagation is frequency dependent. In general it holds that the higher the frequency the more higher harmonics are generated. On the other hand the attenuation

in the propagated medium also increases with frequency counterbalancing the generated harmonics. The SNR of the harmonics depends on the transducer configuration and the characteristics of the propagating medium.
The SNR as a function of the frequency is given by (8.2). The value of every individual harmonic in P was computed using either the KZK equation or the INCS method. We used liver as the propagation medium (c_0 = 1580 m/s, ρ = 1050 kg/m^3 and β = 4.4, μ_a = 2.7 10^{-4} m^{-1}.Sr^{-1}.MHz$^{\mu_b}$ and μ_b = 1.2, α_0 = 5.2 Np.m^{-1}.MHz^{-b} and b = 1.05 [Duck, 1990]). The transducer was the interleaved array reported by van Neer et al. [2010]. This phased array transducer had a low frequency subarray consisting of 44 elements (16 mm x 0.2 mm, center frequency of 1 MHz) interleaved with a high frequency subarray also consisting of 44 elements (13 mm x 0.2 mm, center frequency of 3.7 MHz). The pitch was 0.5 mm and so the lateral dimension of the array was 22 mm. The elevation focus was fixed and set to 60 mm. In the lateral direction the steering angle was set to zero and the focal distance to 60 mm. The transmit transfer (T_e) was taken to be 32.5 kPa/V and for the receive transfer (H_s) 21 μV/Pa was taken (see van Neer et al. [2010]). The transducer and system noise was measured and equal to 7 μV_{RMS}. This measurement was performed on a commercial system including the above mentioned transducer. The excitation amplitude on the transducer was chosen to get a resulting MI in focus of 1.5 (note: MI is equal to the derated peak-negative pressure divided by the square root of the frequency in megahertz).
The KZK equation for an axi-symmetric lightly focussed source was solved in the time domain according to the algorithm described by Lee and Hamilton [1995]. The algorithm was implemented in C and the interface was written in Matlab [Matte et al., 2008b].
For an overview of the parameters used see Table 8.3. The solver of the INCS method has been implemented in parallel and ran on an IBM clustered symmetric multiprocessing system (Huygens system, Amsterdam, the Netherlands). The system consists of 1664 dual core processors (IBM Power6, 4.7 GHz), 128 Gbytes / 256 Gbytes of memory per node. The total peak performance is 60 Teraflop/sec. Depending on the frequency, a single run takes 2 to 30 hours on 32 processors for a complete 3D nonlinear beam profile.

8.4.2 Topology

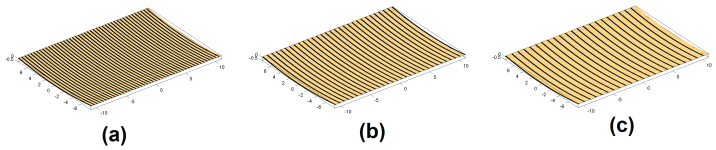

Figure 8.2: Example of interleaved topologies. (a) 1/2 (b) 1/4 (c) 1/8

For the topology the grating lobe level is the discriminating feature and simulations

have been carried out to calculate the fundamental and harmonic main beam together with the sidelobes and grating lobes. For the simulations we used a Gaussian apodized transmission signal of 3 cycles with a frequency of 1.2 MHz. This frequency corresponds to the optimal transmission frequency for SHI and echocardiography (see Fig. 8.4). For the propagation medium we used the properties of liver - c_0 = 1580 m/s, ρ_0 = 1050 kg/m^3. The linear simulations were lossless, for the nonlinear simulations β = 4.4, α_0 = 5.2 Np.m^{-1}.MHz^{-b} and b = 1.05 [Duck, 1990]. The excitation amplitude was set such to get a MI of 1.5 in focus. The used apertures with different transmit-to-receive element ratio's are shown in Fig. 8.5. The beam steering angle was 35° and the lateral and elevation foci were set to 60 mm.
A two step approach was used to calculate the grating lobe levels. Firstly, the fundamental acoustic field was calculated using the FIELD II simulation program [Jensen and Svendsen, 1992, Jensen, 1996]. Secondly, the harmonic grating lobes were estimated from the fundamental grating lobe levels using the Burgers equation. For that the fundamental peak pressure in the grating lobe was used as the starting pressure for the Burgers equation. The wave was then propagated 60 mm. Acoustic attenuation was included. The harmonic levels of the grating lobes were compared to the harmonic levels in the main beam as calculated using INCS simulations for the same apertures shown in Fig. 8.5. For an overview of the parameters used see Table 8.3.

8.5 Results

8.5.1 Transmission frequency optimization

In Fig. 8.3a the SNR of the system as function of the transmission frequency is plotted for the fundamental up to the fifth harmonic. The curves are calculated at a depth of 6 cm. The MI is kept constant at 1.5. As seen in the figure the SNR of the fundamental (H1) ranges between 62 and 79 dB for the transmit frequency range of 0.5 - 2.5 MHz. The second harmonic (H2) SNR ranges between 47 and 70 dB, the third harmonic (H3) SNR between 30 and 61 dB, the fourth harmonic (H4) SNR between 13 and 53 dB and the fifth harmonic (H5) SNR between -2 and 45 dB. For H1 there is no maximum observed for the frequencies between 0.5 and 2.5 MHz. The optimal transmitting frequency is higher than 2.5 MHz. There is a maximum observed for the second, the third, fourth and fifth harmonics. For H2 the maximum occur at 2.1 MHz, for H3 around 1.9 MHz, for H4 around 1.85 MHz and for H5 around 1.75 MHz.
In the figure the results of the KZK as well as the INCS simulations methods are plotted. In the frequency range from 0.8 up to 1.4 MHz the two methods differ only by $\pm$1dB for the fundamental up to the third harmonic, while this is slightly more for the fourth and fifth harmonic ($\pm$2dB). The accuracy of the KZK model decreases for higher frequencies and such high MI of 1.5. The difference between the two models reaches 6 dB at 2.5 MHz. Since the frequency of interest lies for the third, fourth and fifth harmonics between 0.7 and 1.4 MHz the computationally lighter KZK method is used for most of the remainder of this article.

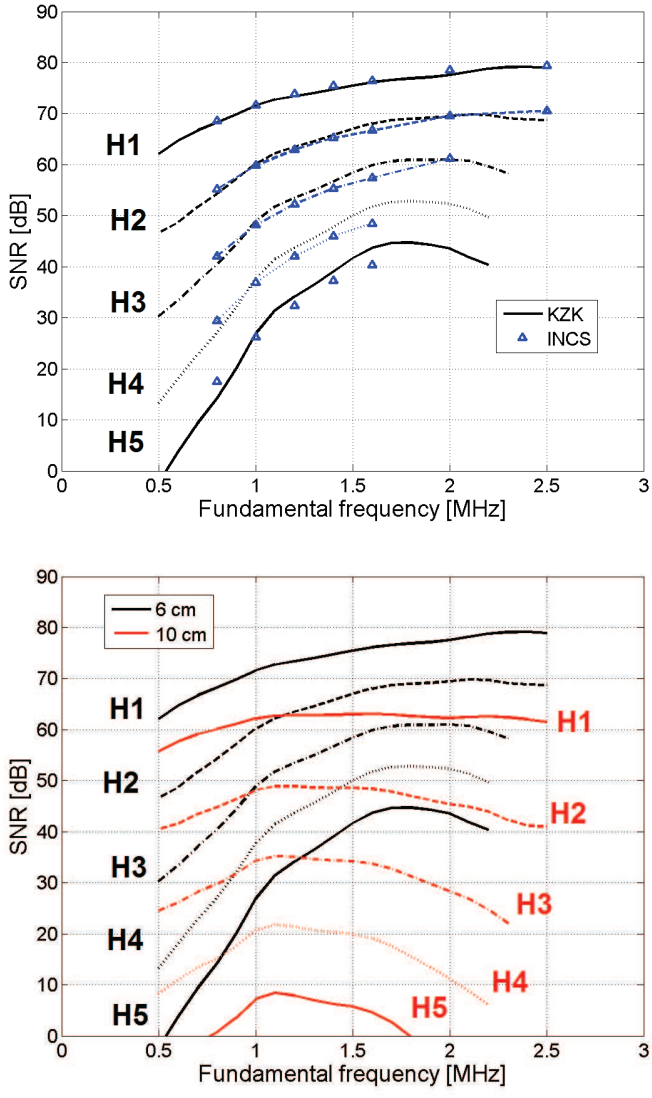

Figure 8.3: a) Comparison between the INCS method and the KZK model at 60mm away from the transducer in a virtual media having the acoustic properties of a homogeneous liver. b) Comparison of the KZK model for two depth ranges. Black lines correspond to a SNR calculated from backscaterrers located at 60 mm depth. For red lines, the backscatterred signal comes from 100 mm away from the transducer. The corresponding harmonics are indicated next to each curve.

For an imaging depth of 10 cm the SNR for each harmonic is given in Fig. 8.3b. Two effects can be seen when comparing these results with those obtained at a 6 cm imaging depth. First, the level of the curve is lower over the whole frequency band and secondly the maximum of the curves shifts towards lower frequencies. Since the focus of all the harmonics are at or around 6 cm both phenomena can be explained by the increased propagation path and consequently the increased attenuation. The fundamental has an SNR of 62 dB and is flat for frequencies above 1 MHz, so for fundamental imaging the preferred frequency is 2.5 MHz or higher. The harmonics show all a maximum around 1.2 MHz. H2 and H3 have a SNR above 30 dB, while the SNR of H4 is still above 20 dB. For the fifth harmonic the level is further decreased at less than 10 dB above the noise level.

In diagnostic ultrasound the transmission frequency used depends on the application and by that on the scanning depth. If the scanning depth increases, the transmission frequency is lower. In Fig. 8.4 intensity plots show the SNR levels in dB as a function of the transmitting frequency and scanning depth. From the figure it can be seen that for the fundamental the most optimal frequency at or higher than 2.5 MHz is for a scanning depth of 6 cm, but for 12 cm the highest SNR is at 1 MHz. For the third harmonic and a scanning depth of for example 12 cm a transmission frequency of 1 MHz result in an SNR of more than 25 dB (light blue), but is close to 0 dB for a transmitting frequency of 2 MHz (dark blue). The fourth and fifth harmonics only have an acceptable SNR at scanning depths smaller than 8 cm.

8.5.2 Topology optimization

The investigated topologies of the array transducer are plotted in the first column of Fig. 8.5. The transmitting elements are colored black, while the receiving elements are colored gray. The transmitting elements always transmit at the fundamental frequency (1.2 MHz). In the middle column the transmit-receive beam profiles for the fundamental frequency are shown. In this case the transmit elements are also used in reception. The right column in Fig. 8.5 shows the convolution of the transmit ultrasound field at the fundamental frequency and the receive ultrasound field at the second harmonic frequency. The steering angle is 35°. Of importance are the main beam size and the off-beam energy, mostly reflected in the side lobes and grating lobes.

Two subarray topology

The two-subarray topology is shown in Fig. 8.5a. The transmitting elements are on one side of the array (black color), while the receiving elements are on the other side (gray color). The middle panel shows the convolved transmit - receive beam at the fundamental frequency. The fundamental beam width at focus is 8.7 mm and the second harmonic beam width is 4.4mm. Notice that the convolved transmit (fundamental)-receive (second harmonic) beam is curved. This effect becomes stronger when looking at higher

harmonics beams.

Three subarray topology

The three-subarray topology is detailed in Fig. 8.5b. The transmitting part is in the center and the two receive parts are located on each side of the transmit array. The fundamental transmit-receive beam is displayed in the middle panel, while the convolved fundamental transmit and second harmonic receive beam is displayed on the right. The fundamental beam is much wider (11.2 mm) than the previous configuration as a result of the smaller aperture. The second harmonic beam on the right measures 7.3 mm at focus. However, at the location of the focal point, the beam splits and has a very high level of side lobes (up to -2dB relative to its center).

Mixed topology

The mixed or interleaved topologies of the array are further shown in Figs. 8.5c, d and e. The interleaving ratio varies from one transmit element for each receiving element (denominated as 1/2, see Fig. 8.5c), up to a ratio of one transmit element for every seven array elements (denominated as 1/8, see Fig. 8.5d).
For the 1/2 configuration there are no grating lobes visible for the fundamental beam and consequently also the second harmonic beam is free of grating lobes. This changes for the 1/4 configuration in Fig. 8.5d. There is a clear grating lobe in the fundamental beam plot located at about -35°. In the second harmonic beam profile the grating lobe level is greatly diminished and just above the noise level. For the 1/8 configuration in Fig. 8.5e there are two grating lobes, one at -35° and the other one at zero degrees. The one at 0° is only -10 dB below the main beam intensity. For the second harmonic beam the grating lobe is still there, but the level is now $\sim$-20 dB. The main beam in the mixed topologies is more or less independent of the interleaving ratio, since the aperture remains the same. The beam width at 6 cm is 7.8 mm.
Table 8.1 summarizes the results of the grating lobe level of the fundamental and second harmonic as discussed above and includes an extension for the third - fifth harmonic components. According to Cobbold [2007] an imaging system should have a grating lobe to main lobe level of less than -40 dB. From Table 8.1 it can be read that for the fundamental mode the maximum interleaving ratio of the transmit-receive elements is 1/2. For the second harmonic the maximum ratio is 1/4, while for the third harmonic a ratio of 1/7 still provides a grating lobe to main lobe level below -40 dB. For the fourth and fifth harmonics the grating lobe levels stay below -40 dB in all configurations.

Table 8.1: Grating lobes and SNR simulations of mixed topologies

f_0	Pitch	Nbr. of receivers	SNR fundamental	SNR H2	SNR H3	SNR H4	SNR H5
[MHz]	-	-	[dB]	[dB]	[dB]	[dB]	[dB]
1.2	1/2	44	74	63	52	42	32
	1/3	59	23	56	83	107	130
	1/4	66	15	41	59	76	92
	1/5	70	13	36	50	64	77
	1/6	73	11	32	46	57	69
	1/7	75	9	30	42	53	62
	1/8	77	8	27	37	47	55

Table 8.2: Remaining dynamic range

f_0	Pitch	Nbr. of receivers	SNR fundamental	SNR H2	SNR H3	SNR H4	SNR H5
[MHz]	-	-	[dB]	[dB]	[dB]	[dB]	[dB]
1.2	1/2	44	74	63	52	42	32
	1/3	59	23	56	55	45	35
	1/4	66	15	41	56	46	36
	1/5	70	13	36	50	46	36
	1/6	73	11	32	46	46	37
	1/7	75	9	30	42	47	37
	1/8	77	8	27	37	47	37

8.6 Discussion

8.6.1 Transmission frequency optimization

The results presented in this paper allow for validation of the findings on the optimal transmission frequency for second harmonic imaging but also for prediction of the same parameter for imaging based on higher harmonics. Kasprzak et al. [1999] investigated experimentally the optimal transmission frequency for second harmonic imaging. Their methodology consisted of comparing the quality of the images produced by several commercial echographic systems on the frequency range of 1.6 - 1.8 MHz and 2.1 - 2.4 MHz. Kasprzak et al. [1999] found that a relatively low 1.6 - 1.8 MHz transmission frequency is necessary to visualize the whole heart including the parts furthest away from the transducer. We translate the qualitative criteria used by Kasprzak et al. [1999] into an explicit demand for the dynamic range at the maximum imaging depth depending on the transmit frequency. In the case of echocardiography we analyze our results at 12 - 15 cm requiring a 30 - 40 dB dynamic range at this distance. Indeed our simulation results confirm the initial findings of Kasprzak et al. [1999] and show that the optimal transmission frequency is $\sim$1.7 MHz for second harmonic echocardiography (see Fig. 8.4) - this provides an SNR of 32 dB at 13 cm. The optimal transmission frequency for the selective imaging of the third harmonic is 1.0 - 1.2 MHz (see Fig. 8.4). However, with a third harmonic SNR of $\sim$22 dB at 13 cm it is below the 30 dB dynamic range criterion. Both the fourth and fifth harmonics would not provide sufficient dynamic range at 13 - 15 cm for the selective imaging using either. As the third harmonic contains the most energy of the components in the superharmonic band, the optimal transmission frequency for superharmonic echocardiography is concluded to be 1.0 - 1.2 MHz (see Fig. 8.4). Although the fourth and fifth harmonics are below the noise floor at 14 - 15 cm, they still contribute to the superharmonic image at shallower depths. The optimal transmission frequency found for SHI is in agreement with the 1.0 MHz reported by van Neer et al. [2010].

The maximum imaging depth for imaging of the kidneys, the gallbladder or the abdominal aorta is at 9 - 10 cm lower than that for echocardiography. Therefore, the optimal transmission frequency for second harmonic imaging is at $\sim$2.5 MHz also higher (see Fig. 8.4). For third harmonic imaging the optimal transmission frequency becomes $\sim$1.7 - 1.9 MHz. For imaging based on the fourth harmonic the optimal transmission frequency is $\sim$1.6 MHz, but the harmonic level remains below the required 30 dB dynamic range threshold with an SNR of 22 dB at 10 cm (see Fig. 8.4). The optimal transmission frequency for SHI is $\sim$1.8 MHz, since the third harmonic component contains the most energy of the components in the superharmonic band. Both the fourth and fifth harmonics are above the noise floor and contribute to the superharmonic image.

The simulations reported here were performed for a homogeneous medium using the material properties reported for liver. However, the human body has a heterogeneous structure with considerable variation in tissue material properties and interfaces in between different tissue types, where the acoustic impedances vary strongly. For example

in the case of echocardiography, most of the propagation medium consists of blood and cardiac tissue. Although the range of reported B/A and attenuation values for cardiac tissue are similar to those reported for liver, the attenuation values reported for blood are four times lower than that of liver tissue at similar B/A values [Duck, 1990]. Therefore, the SNR levels reported here should be interpreted as a worst case scenario.
Also, the element geometry used for the simulations was based on the geometry reported for a transducer intended for echocardiography. In this modality the height and width of the transducer is limited by the space between the ribs. However, in abdominal imaging there is no such constraint and the element dimensions and number of elements can be increased. This would increase SNR but the reported trends would remain similar.

8.6.2 Topology optimization

The convolved transmit(fundamental)-receive(harmonic) beam is curved in the case of the two-groups topology. To use this topology the electronic delays used in transmission to steer the beam have to be adapted. For large steering angles the effective steering is lower than expected relative to the origin of the aperture, as at these angles the contribution of the farthest elements to the focal point is overestimated. This misplaces the effective backscattered signal at an incorrect position in space. Next to that the spatial sampling of the B-mode image would be nonuniform requiring extra postprocessing to correct for the location of peculiar point spread functions. The three group topology does not have the aforementioned problems, but the convolved transmit-receive beam is wide. At the limit of the large group topology is the interleaved topology. Its convolved transmit-receive beam is the most narrow and well defined. Therefore, the fully interleaved design is preferred over topologies consisting of a lower amount of groups.
The mixed topologies combine the well defined beams of the interleaved design with an increase in surface area dedicated for receiving. The dynamic range of an ultrasound system is limited by the grating lobe to main lobe ratio and the maximum SNR, where the lower of the two is the main determinant. Cobbold [2007] states that the grating lobe pressure should be 40 dB below the pressure in the main beam. Focusing on the third harmonic, our simulations show that the 1/7 configuration provides the maximum number of receive elements while still providing a grating lobe level less than -40 dB compared to the main beam (see Table 8.1). For the fourth and fifth harmonics all configurations provide sufficiently low grating lobe levels. As the third harmonic has the highest intensity overall of the superharmonics (third to fifth harmonics), the 1/7 configuration is optimal for superharmonic echocardiography.
The optimal 1/7 configuration uses 75 elements for reception, compared to the 44 elements used in reception by the interleaved (1/2) configuration reported by Bouakaz et al. [2004] and van Neer et al. [2010]. The increased number of receive elements improves the total SNR by $\sim$5 dB, because of the reception of an increased amount of backscattered energy and the reduction of the effective noise level after beamforming. Although a 5 dB improvement in SNR may seem like a modest improvement, it is an SNR improvement over the entire imaging depth.

The main assumption here is that the voltage over the transducer clamps - or the transmit efficiency of the transmit elements - can be increased sufficiently to compensate for the reduced number of transmit elements. van Neer et al. [2010] reported reaching an MI of 1.9 by exciting their 1/2 transducer using signals 60 V in amplitude. Thus to reach the same peak pressures using the 1/7 configuration the amplifier output should be increased to 200 V. This voltage level should pose no problem to the integrity of the piezomaterial used by van Neer et al. [2010] in their array design, as the piezomaterial is with a $\sim$1 MHz resonance frequency sufficiently thick.
Although the pressure at focus will be within regulatory limits, the pressure near the element surface of the optimal 1/7 configuration will exceed it. The generated pressure would fall rapidly further along the axial dimension, because of the small size of the elements in the lateral dimension. Thus the issue could be solved by placing a thin slab of low loss material with an acoustic impedance close to that of tissue between the patient and the transducer.

8.7 Conclusion

The optimal transmission frequency for superharmonic echocardiography was found to be 1.0 - 1.2 MHz. For superharmonic abdominal imaging this frequency was found to be 1.7 - 1.9 MHz. For second harmonic echocardiography the optimal transmission frequency of 1.8 MHz reported in literature was corroborated and for second harmonic abdominal imaging a frequency of 2.5 MHz was found. The optimal topology for superharmonic echocardiography was the mixed transducer configuration with 1 transmit element per 6 receive elements. This configuration improves the SNR by $\sim$5 dB compared to the interleaved (1/2) design reported by Bouakaz et al. [2004] and van Neer et al. [2010].

8.8 Acknowledgments

This work was supported by the Dutch Technology Foundation (STW) and by the Dutch National Computing Facilities Foundation (NCF).

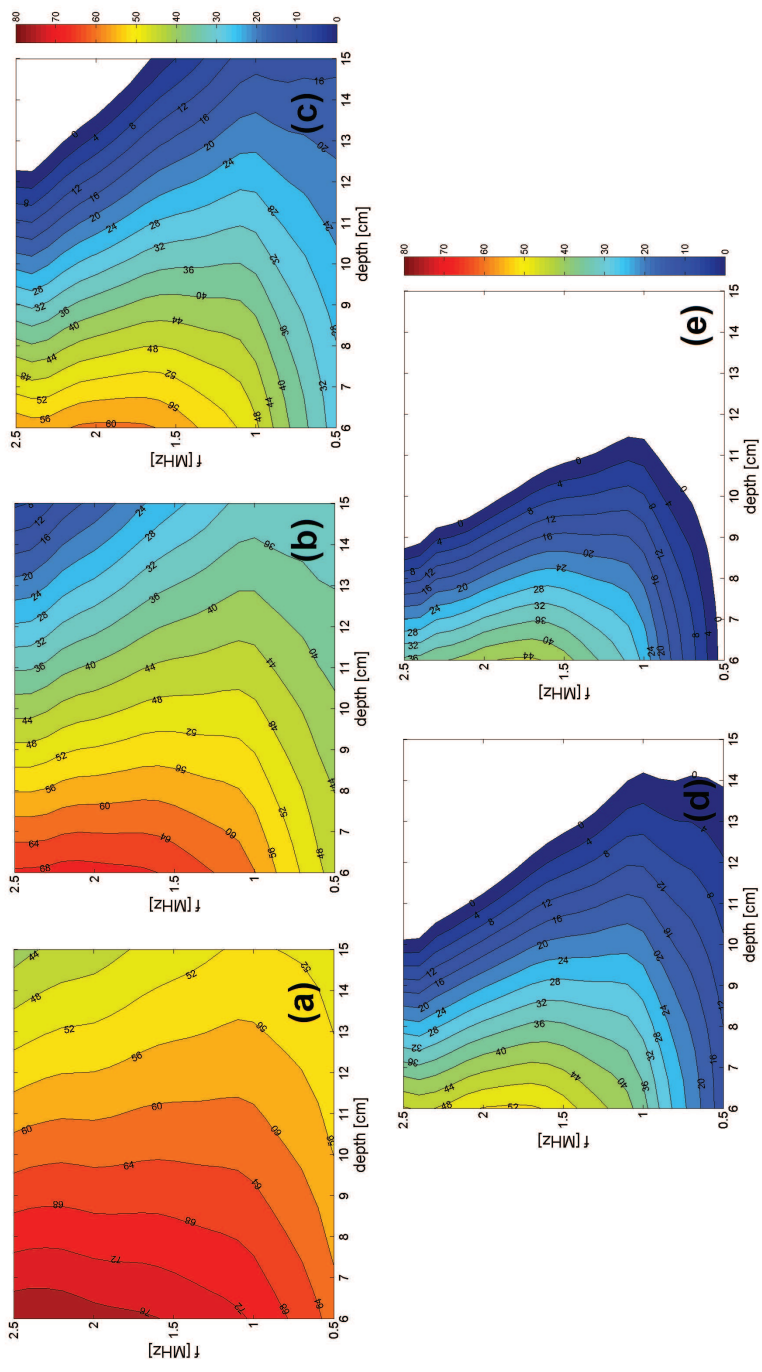

Figure 8.4: Representation of the harmonic SNR depending on the depth. Panel H1 shows the fundamental frequency, panel H2 details the second harmonic, panel H3 displays the third harmonic, panel H4 shows the fourth harmonic and panel H5 details the fifth harmonic. The color scale gives the level of the SNR and ranges from 80 dB (dark red) till 0 dB (dark blue)

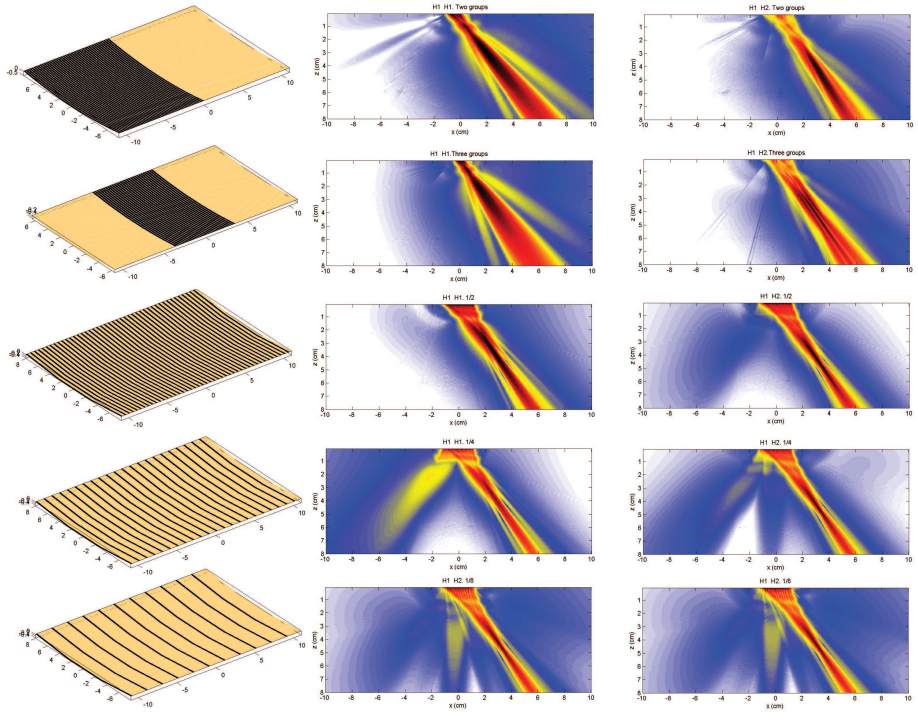

Figure 8.5: a) Two group topology. b) Three group topology. c) Interleaved 1/2 topology. d) Interleaved 1/4 topology. e) Interleaved 1/8 topology. The black elements are used in transmission, the gray elements are used in reception. The middle column shows the convolved fundamental transmit - receive beam using the darkly colored aperture only. The right column shows the convolved fundamental - second harmonic beams using the complete aperture.

Table 8.3: Simulation input parameters

Simulation type	Element length [mm]	Element width [mm]	Nbr. of elements	c_0 [m/s]	ρ_0 [kg/m^3]	Kerf [mm]	Steering angle [°]	Pulse length	Absorption (α_0) [Np.m^{-1}.MHz^{-b}]	Absorption (b)	Scattering (μ_a) [cm^{-1}.Sr^{-1}.MHz$^{\mu_b}$]	Scattering (μ_b)	β
Frequency (SNR calculation)	16	0.2	44	1580	1050	0.05	0	3	5.2	1.05	$2.7.10^{-4}$	1.2	4.4
Topology (INCS - main beam)	16	0.2	varies	1580	1050	0.05	-	3	5.2	1.05	-	-	4.4
Topology (Field II - grating lobe)	16	0.2	varies	1490	1000	0.05	35	3	0	-	-	-	3.5
Topology (Burgers - grating lobe)	16	0.2	varies	1580	1050	0.05	-	3	5.2	1.05	-	-	4.4

CHAPTER 9

Dual pulse method for super harmonic imaging

9.1 Introduction

The idea of using the nonlinear properties of the medium to generate harmonics of the incident ultrasound field dates back to the work of Kompfner and Lemons [1976] on acoustic microscopy. The relevance of this phenomenon in the context of medical applications was later shown by Muir and Carstensen [1980] and experimentally validated by Starritt et al. [1986]. These two discoveries spawned the new era of harmonic imaging in medical ultrasound. To date this technique has become the standard for studying the nonlinear behavior of ultrasound contrast agents (UCAs). From a medical point of view it allows to detect areas of perfused or non-perfused tissue and, hence, to assess the function of anatomic organs. Until recently however, the quantitative analysis was limited to the second harmonic only.

A few years ago a new method for tissue and UCA imaging was proposed by Bouakaz et al. [2002a]. It was based on the selective imaging of the combined harmonics (from the third up to the fifth) and was dubbed superharmonic imaging (SHI). SHI inherits the benefits of second harmonic imaging, but further improves the spatial resolution and reduces the level of the sidelobes. The experimental comparison of the B-mode scans of the bladder cavity, obtained with second and superharmonic imaging, were the first images produced with this method [Bouakaz and de Jong, 2003]. The inner fluid-filled cavity appeared not only more hypoenhanced, but the speckle size became thinner. Moreover,

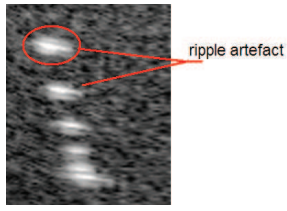

Figure 9.1: evidence of ripple artifact from super harmonic image on a wire phantom

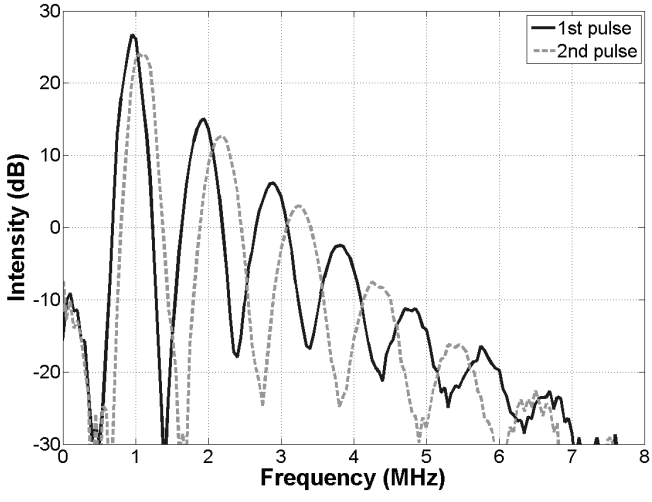

Figure 9.2: The concept of the dual pulse frequency compounding method for SHI.

the simulation results showed that the energy content of the second and superharmonic components are similar in the far-field [Bouakaz and de Jong, 2003, Ma et al., 2006].

If the transmitted pulse would have a single cycle length, the demodulation of the signal received over the superharmonic band would dramatically improve the axial resolution 9.3. The choice to combine the third to fifth harmonics was made to integrate the energy over a large frequency band to gain in terms of amplitude of the received pulse compared to a single harmonic. Another viewpoint is to consider the fourth harmonic as the center of this band of interest. The band of the neighboring harmonics is then used to enlarge the receiver frequency band and thus to increase the axial resolution.

Contemporary transducers made of PZT piezoceramics have up to 80% -6 dB bandwidth with good transmit efficiency, but the transmission system bandwidth is often

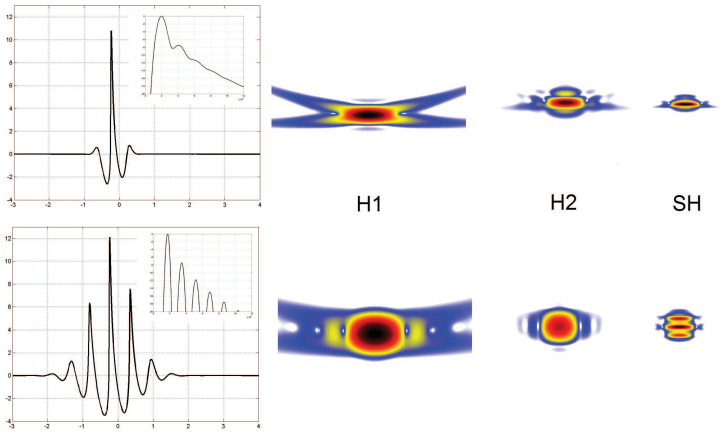

Figure 9.3: PSF comparison for 1 cycle and 3 cycles transmission

lower due to electrical tuning. If a pulse with low bandwidth propagates nonlinearly in a medium such as water or tissue, the resulting distorted pulse will show distinct troughs in its frequency spectrum 9.2. Demodulation on such a multiple frequency component signal leads to specific artefacts visible as ripples in the envelope 9.1.
We propose a solution consisting of transmitting two pulses with the second pulse of slightly different frequency. The sum of these two pulses in the time domain produces a smooth frequency spectrum and the ripple artifacts are minimized. In the time domain, the sum of the two distorted pulses and the wideband filtering around the fourth harmonic is analogous to destructive interference on the ripples of the superharmonic signal. This effect sharpens the superharmonic point spread function (PSF). The PSF used here combines the initial electrical excitation (the pulsing scheme), the transmit transfer function and the spatial impulse response with the effects of nonlinear propagation and postprocessing. Firstly, a method to calculate the optimal frequency of the second pulse based on nonlinear wave propagation is described. Secondly, the performance of the dual pulse method will be explored using KZK simulations and experiments with a single element transducer. Finally this method made to improve the super harmonic PSF will be applied to phased array transducer specially built for super harmonic imaging.

9.2 Theory

First of all, some assumptions are made in order to simplify calculations. The initial pressure at the transducer surface is assumed to be an ideal gaussian apodised burst as defined in eq. 9.1.

$$p(0,\tau) = p_0 e^{\left[-\left(\frac{\omega_0 \tau}{n_c \pi}\right)^2\right]} e^{i(\omega_0 \tau + \varphi)}, \tag{9.1}$$

In time domain, the expression of the acoustic signal distorted during its propagation in a non linear medium takes the form

$$p(z,\tau) = p_0 \sum_{n=1}^{\infty} B_n(z) e^{\left[-n\left(\frac{\omega_0 \tau}{n_c \pi}\right)^2\right]} e^{i(n\omega_0\tau + \varphi_n)}, \tag{9.2}$$

with

p_0 the initial pressure

n the number of harmonics

n_c the number of cycles. The number of cycles is directly linked to the transducer bandwidth. Lets consider Δf the -3 dB band of the transducer, $n_c = f_0/\Delta f$

τ the time

ω_0 the angular frequency of the fundamental

φ_n the phase term associated to its respective harmonic n

B_n the amplitude of the the n^{th} harmonic component

z the axial distance

Using distributions (from Schwartz [1965]) for $\omega \in [0; +\infty[$ (9.2) can be written in the frequency domain as

$$p(z,\omega) = p_0\sqrt{2\pi} \sum_{n=1}^{\infty} \frac{B_n}{\sqrt{2\mu_n}} e^{\left[-\frac{(\omega - n\omega_0)^2}{4\mu_n}\right]}, \tag{9.3}$$

with ω the angular frequency and $\mu_n = n\left(\frac{\omega_0}{n_c \pi}\right)^2$.

the expression of this signal on the band of interest $[3f_0 - \frac{\Delta f}{2}; 5f0 + \frac{\Delta f}{2}]$ reaches

$$p_{SH}(z,\omega) = p_0\sqrt{\pi}\frac{n_c \pi}{\omega_0}\left[\frac{B_3}{\sqrt{3}} e^{-\frac{\left(\frac{\omega}{\omega_0} - 3\right)^2 \left(\frac{\pi n_c}{2}\right)^2}{3}} + \frac{B_4}{\sqrt{4}} e^{-\frac{\left(\frac{\omega}{\omega_0} - 4\right)^2 \left(\frac{\pi n_c}{2}\right)^2}{4}}\right]. \tag{9.4}$$

To find the frequency of the minimum between the third and fourth harmonic we need to solve $\frac{dp_{SH}(z,\omega)}{d\omega} = 0$ around $\omega = 3.5\omega_0$. To this end (9.4) is developed in a Taylor series

around $\omega = 3.5\omega_0$. A second order Taylor series provides sufficient accuracy (a third order expansion improves the accuracy by only 0.05%) and leads to

$$\frac{\omega_{min}}{\omega_0} = \frac{\frac{B_3}{6\sqrt{3}} e^{\frac{-(n_c\pi)^2}{48}} - \frac{B_4}{8\sqrt{4}} e^{\frac{-(n_c\pi)^2}{64}}}{\left[\frac{(n_c\pi)^2}{24} - 1\right] \frac{B_3}{3\sqrt{3}} e^{\frac{-(n_c\pi)^2}{48}} + \left[\frac{(n_c\pi)^2}{32} - 1\right] \frac{B_4}{4\sqrt{4}} e^{\frac{-n_c\pi}{64}}} + 3.5, \tag{9.5}$$

with ω_{min} the angular frequency of the minimum between the 3^{rd} and 4^{th} harmonics.

The optimum frequency shift is then given by $\omega_2 - \omega_0 = \frac{\omega_{min} - 3\omega_0}{3}$.
Initially, B_n was considered using a modified version of the Fubini solution [Matte et al., 2008a]. Those calculation were quick and useful for the understanding but accounting for strong approximations. Solving numerically the KZK equation (Lee and Hamilton [1995]) leads to more realistic values for the term B_n and φ_n. Also, for more accuracy, the transducer frequency response was incorporated. Its expression was simplified as

$$T(f) = e^{-2\pi\left(\frac{f-f_0}{Q\ f_0}\right)^2}, \tag{9.6}$$

and the expression of the phase at the transducer surface

$$\varphi_0(f) = -\arctan\left(\frac{f - f_0}{f_0}\right), \tag{9.7}$$

with f the frequency, $Q = \frac{\Delta f}{f_0}$ the mechanical quality factor, and f_0 the resonance frequency.

9.3 Materials and Methods

9.3.1 Numerical simulations

The influence of this two pulse method on the point spread function was studied using KZK simulation. The KZK equation was solved using a custom made program written in C and Matlab. The simulations defined an axi-symmetric transducer of 13 mm diameter transmitting a Gaussian burst of tunable frequency. Because of the discrepancies between previous simulations and experiments Matte et al. [2008a], van Neer et al. [2009a] the frequency response of the transducer was incorporated in the simulation. To do so, the phase and amplitude of the initial pressure at the transducer surface was set for each frequency step according to the simulated frequency response of the transducer 9.6 9.7.

9.3.2 Experimental setup

The experimental setup consisted of a water-filled tank, which featured a hydrophone (diameter 0.2 mm, Precision Acoustics, Dorchester, UK) mounted in an xyz-system. A

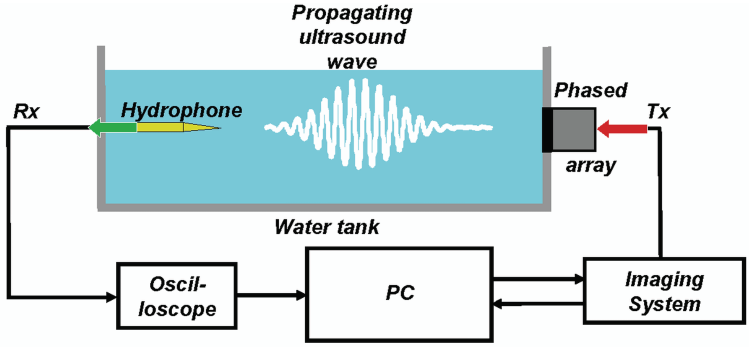

Figure 9.4: The experimental setup.

custom made dual frequency transducer (Oldelft ultrasound, Delft, the Netherlands) was attached to the tank's sidewall. The elements of the low frequency subarray were excited by Gaussian apodized sine bursts of varying frequency with an amplitude of 120 V_{pp}. The excitation signals were produced by a multi channel programmable ultrasound system (OPEN system, Lecoeur Electronique, Chuelles, France, first reported in [Vignon et al., 2005]). The signals received by the hydrophone were digitized by an oscilloscope (9400A, Lecroy, Geneva, Switzerland) with a sampling frequency of 100 MHz and transferred to a computer for further processing. The experimental setup is shown in Fig 9.4. The frequency of the transmitted pulse was swept between 0.89 and 1.3 MHz.

9.3.3 Simulation of echographic images

A virtual phantom was simulated by multiplying matrices associated to echogeneocity map by a matrix containing random values. The resulting virtual phantom is displayed fig. 9.5. The convolution of this scattering matrix with the measured RF signal of several harmonics PSF gives the simulated scattered signal 9.5. This simulation of echographic images was first described by Walker and Trahey [1998]. This simulation disregards the

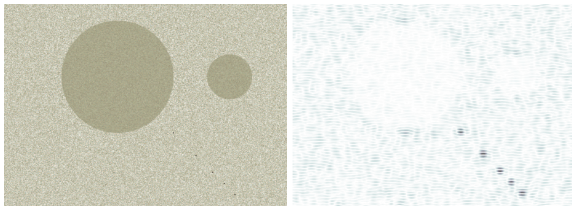

Figure 9.5: Right : Scattering map of the virtual phantom. Left : simulated second harmonic scattered signal

evolution of the PSF along the beam as well as the attenuation or non linearity that affect

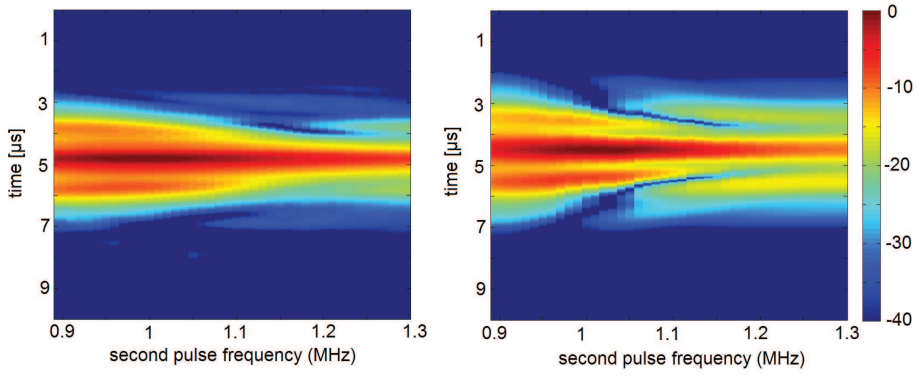

Figure 9.6: The axial intensity profiles (vertical axis) versus the frequency of the second pulse (horizontal axis) for a 3-cycle transmission. The intensity is color coded using a dynamic range of 40 dB. The frequency of the first pulse was fixed at 0.89 MHz. Left : experiment, Right : simulation

the pulse during propagation. It is an idealistic simulation in order to foresee what would be achievable in the best configuration.

9.4 Results

The energy intensity in the axial dimension versus the frequency of the second pulse is shown on Fig 9.6 for a 3 cycles apodized gaussian burst. The frequency of the first pulse was 0.89 MHz. In this case the optimal frequency of the second pulse was 1.15 MHz. This result in the summed pulse corresponds to the best improvement of the PSF, meaning that the ripple are best canceled at this frequency.

Experimentally, a trade off implies an optimum pulse length with the amount of transmitted energy. This effect is cause by the finite bandwidth of the transducer. That has a direct impact on the quality of the super harmonic point spread function. This compromise was studied by Van Neer et al. [2010]. The optimal dual pulse PSF was found to be 0.87 MHz and 1.12 MHz with this phased array transducer. In this configuration, the peak intensities of the second and third harmonics and superharmonic component were -30 dB, -38 dB and -34 dB respectively. A comparison between the third harmonic PSF and the optimal dual pulse SHI PSF is shown in Fig. 9.7. The dual pulse SHI lateral beam widths at -6 dB and -20 dB were 1.8 mm and 3.4 mm respectively, whereas for the third harmonic these were 2.2 mm and 3.4 mm respectively. The axial beam widths at -6 dB and -20 dB were 0.8 mm and 3.4 mm respectively for dual pulse SHI and 2.5 mm and 5.3 mm for the third harmonic (Fig. 9.7).

Simulated echographic images provide insight to what can be expected experimen-

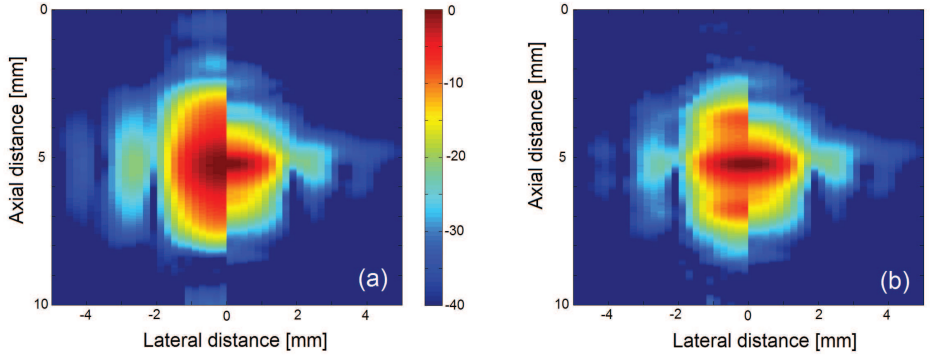

Figure 9.7: (a) Experimental comparison of a third harmonic PSF (left), and a dual pulse PSF (right).
(b) Experimental comparison of a single pulse super harmonic PSF (left), and a dual pulse super harmonic PSF (right)

tally (fig. 9.8). The image made with one pulse superharmonic has a fuzzy aspect. Not only reflection on hard scatterers exhibits this ripply behavior, but the background speckle is also disturbed by this effect. The improvement compared to the second harmonic image is visible bu not optimal. The image corresponding to the dual pulse method is a good improvement on the other images. The grain of the dual pulse superharmonic image is finner, the hard scatterers are better resolved and the contrast with the hypoechoic regions is enhanced.

9.5 Discussion and conclusion

The optimal frequency shift between first and second pulse varied between 0.25 and 0.27 MHz. Those numbers are somewhat is higher than the theoretically predicted value of 0.15 MHz reported here. This can be attributed to the transfer functions of both transducer and system, that were not seriously taken into account. More likely, is that simulation where performed assuming an axi-symmetric transducer, which differs greatly from the experimental protocol. The investigation on this technique with axi-symmetric transducer was initiated by Matte et al. [2008a] but the transducer frequency response was not modeled. One step has been overlooked.
Considering the resolution, the lateral beam widths of the optimal dual pulse signal are 1.2 times smaller at the -6 dB level and equal at the -20 dB level compared to the third harmonic. The axial beam widths of the optimal dual pulse signal are 3.1 times smaller at the -6 dB level and 1.6 times smaller at the -20 dB level compared to the third harmonic. Simulations of superharmonic dual pulse method display a significant improvement on the image quality, resolution and contrast. Those finding corroborate the results initially

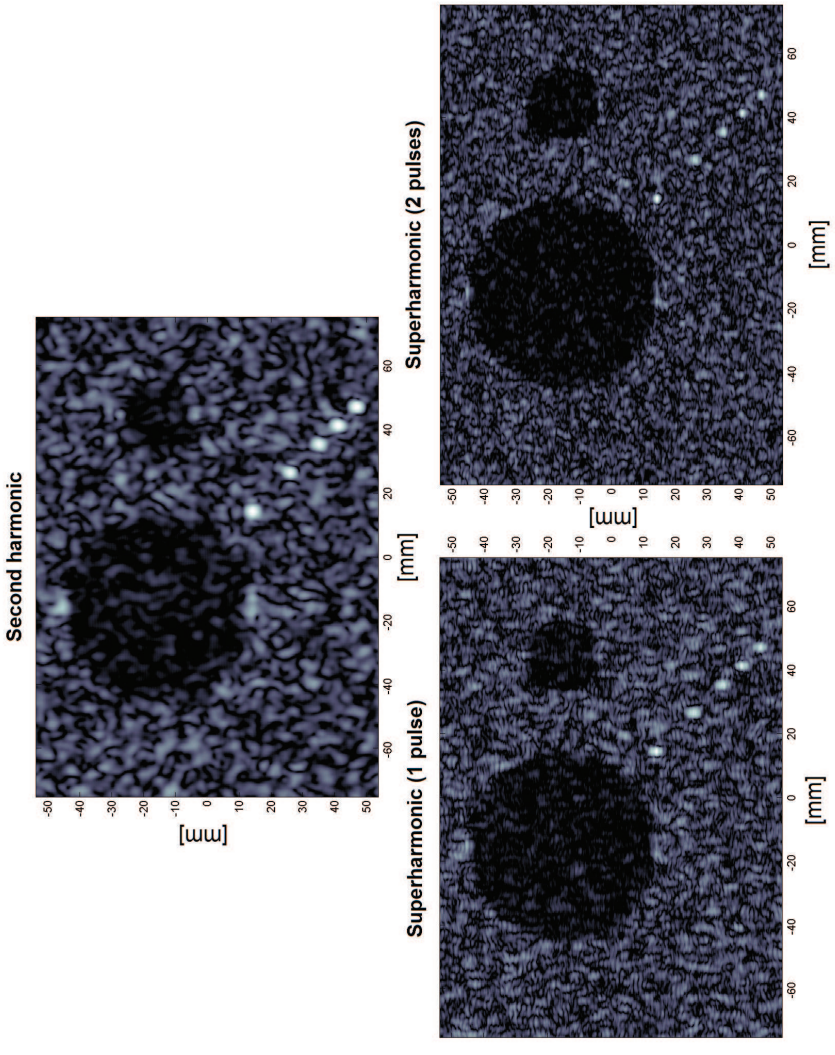

Figure 9.8: Echographic image comparison. A. Third harmonic. B. 1 pulse SHI. C 2 pulses SHI

observed by Bouakaz et al. [2002a].

CHAPTER 10

Chirp based superharmonic imaging for phased array transducers

Paul L.M.J. van Neer, Mikhail G. Danilouchkine, Guillaume M. Matte, Marco M. Voormolen, Martin D. Verweij, Nico de Jong

From proceeding ASA/NOISE-CON 2010, Baltimore

Abstract Second harmonic imaging has become the de-facto standard for commercial ultrasound systems. Super harmonic imaging (SHI), which targets a combination of the 3rd to 5th harmonics, has certain advantages in comparison to the established standard. The new technique is expected to enhance spatial resolution and, thus, the quality of echographic images. On the other hand, those images are susceptible to so-called ripple artifacts, stemming from the gaps in between harmonics in the frequency domain. The recently proposed dual-pulse frequency compounding protocol suppresses the aforementioned artifacts at the cost of a reduced frame rate [Matte et al., 2008a, van Neer et al., 2009b]. In this work, we employ the chirp protocol for SHI without sacrificing the acquisition speed and investigate its characteristics, i.e. point spread function (PSF). The chirp protocol was implemented on a superharmonic interleaved phased array probe (44 elements tuned at 1 MHz, 44 elements at 3.7 MHz), connected to a fully programmable ultrasound system. A linear chirp with a center frequency of 0.95 MHz and bandwidth of 40% was used as the excitation pulse. The RF traces were recorded at the focal plane along the lateral axis and convolved with the decoding signal to obtain the PSF's. For decoding the pressure signal in focus, computed using a KZK simulation, was used. The lateral beam width of the superharmonic chirp signal is 0.8 and

0.9 times the lateral beam width of the third harmonic at the -6 dB and -20 dB levels respectively. With regard to the axial beam width, the superharmonic chirp signal is 0.9 and 0.8 times the axial beam width of the third harmonic at the -6 dB and -20 dB levels respectively. The PSFs produced using the superharmonic chirp protocol are virtually free from ripples. The superharmonic PSFs show increased spatial resolution in comparison to the third harmonic.

10.1 Introduction

Second harmonic imaging is currently the de-facto standard in commercial echographic systems for diagnosis because of its improved resolution and contrast-to-tissue ratio. An emerging technique called superharmonic imaging (SHI) is based on a combination of multiple frequency components generated during the propagation of sound in tissue [Bouakaz et al., 2002a]. This combination of third to fifth harmonic has the potential to further enhance resolution and image quality of echographic pictures. Tissue SHI efficiently suppresses near-field artifacts, reverberations, and off-axis artifacts in addition to the enhanced lateral and axial resolution. The resulting images showed more details than those produced by second harmonic imaging [Bouakaz and de Jong, 2003].
In spite of the apparent advantages of SHI, there exists a fundamental problem associated with this method. The bandwidth of contemporary electrically tuned transducers is limited. If a pulse with limited bandwidth propagates nonlinearly in a thermoviscous medium, the resulting distorted pulse will show distinct troughs in its frequency spectrum. These troughs between the harmonics lead to ripples in the point spread function (PSF), which give rise to ghost reflections along the direction of the wave propagation in practical imaging situations.
In previous work we introduced a dual pulse method to solve the ripple issue and showed its feasibility for phased array transducers [Matte et al., 2008a, van Neer et al., 2009b]. The imaging protocol is based on the transmission of two pulses with the second pulse of slightly different frequency. The echoes produced by each transmission pulse are summed to create an image. The methodology produced good results, but it does have a few drawbacks. Firstly, it is based on transmitting two pulses per A-line and thus the maximum attainable frame rate is reduced by a factor of two - quite a compromise to make when imaging fast moving structures such as heart valves. Secondly, the total amount of energy transmitted into the tissue is limited. It was shown in previous work that an optimum exists between the method's ability to suppress the ripples and the length of the transmitted pulses [van Neer et al., 2009b]. Thus, the time-bandwidth product of the signals involved in this method is low. To improve the time-bandwidth product coded excitation could be used, which has been shown to improve the SNR by the time-bandwidth product [Misardis and Jensen, 2005b]. The improved SNR leads to an increased penetration depth. This is especially useful for higher harmonic imaging, since the signal amplitudes of the higher harmonics are generally low.

In this work we employ a chirp protocol for SHI without sacrificing the acquisition speed. Its characteristics in terms of point spread functions (PSF) are investigated. The PSF used here combines the convolution of the electrical excitation (the pulsing scheme), the transmit transfer function and the spatial impulse response with the effects of nonlinear propagation and postprocessing.

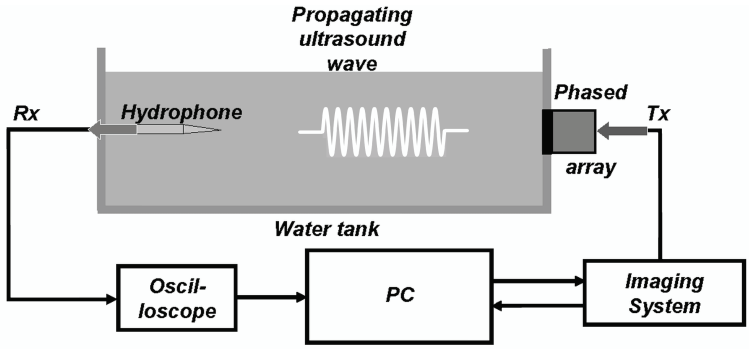

Figure 10.1: The experimental setup.

10.2 The chirp protocol

The chirp protocol is based on coded excitation. It is based on the transmission of a pulse train with certain properties (a code). In reception the pulse train is compressed using a decoding filter to obtain an image. The first report on coded excitation in medical literature dates back to 1979 [Takeuchi, 1979]. Since then a sizable volume of literature has been dedicated to imaging using coded excitation - an excellent overview is given by Misardis and Jensen [2005b,a]. Among the codes investigated were chirps [Pollakowski and Ermert, 1994], orthogonal Golay codes [Chiao and Thomas, 2000] and binary sequences [Shen and Ebbini, 1996]. Recently, coded excitation using linear chirps was also used for second harmonic imaging of ultrasound contrast agents [Borsboom et al., 2003].
The chirp protocol for SHI consists of transmitting a frequency modulated signal and receiving the third to fifth harmonic. The recorded echo is compressed using a decoding signal. Linear chirps were used because of their higher SNR gain at large imaging depths relative to pulsed excitation compared to the SNR gain reported for nonlinear chirps and Golay codes [Misardis and Jensen, 2005b]. The filtered superharmonic band of the on-axis pressure signal in focus computed with the KZK method was used for decoding.

10.3 Materials and methods

10.3.1 Experimental setup

The experimental setup consisted of a water-filled tank featuring a hydrophone (diameter 0.2 mm, Precision Acoustics, Dorchester, UK) mounted in an xyz-system. A special dual frequency transducer [van Neer et al., 2010] was mounted in the tank's sidewall. The elements of the low frequency subarray were excited by linear 0.95 MHz chirps with a -6 dB bandwidth of 40%, amplitude 24 V and length 15 μs. The excitation signals were produced by a multi channel programmable ultrasound system (OPEN system, Lecoeur

Electronique, Chuelles, France, first reported in [Vignon et al., 2005]). The signals received by the hydrophone were digitized by an oscilloscope (9400A, Lecroy, Geneva, Switzerland) with a sampling frequency of 100 MHz and transferred to a computer for further processing. The experimental setup is shown in Fig. 10.1.

10.3.2 KZK simulations

The decoding pulse was generated using simulations based on the KZK equation. The KZK equation was solved in the time domain. The nonlinearity and absorption terms were solved using the numerical methods developed by Lee [1993] [Lee and Hamilton, 1995]. The diffraction term was solved in the near-field using an implicit backward finite difference method and in the far field using an alternating direction implicit method. The first method is more effective in damping numerical oscillations and the latter method is more accurate allowing for larger step sizes [Voormolen, 2007]. The algorithm was implemented in the C and Matlab languages. The simulations were performed in full 3D. The low frequency subarray of the dual frequency array was used as the source: the subarray consisted of 44 elements with size 16 mm x 0.2 mm and pitch 0.5 mm [van Neer et al., 2010]. The subarray was modeled as a rectangular aperture of 16 x 22 mm. The transmitted pressure was scaled to take into account the kerf between the elements. Lateral and elevation foci at 6 cm were implemented to model the elevation lens and the electronic focusing. As the input for the simulations a voltage chirp similar to the one used for the experiments was used. The voltage chirp was converted to the output pressure pulse of the low frequency subarray using the transmit transfer function [van Neer et al., 2010]. The effect of the electrical impedance of the transmitter circuits was neglected as the electrical impedance the arbitrary waveform generator outputs (5 Ω) was low compared to the electrical impedance of the transducer elements (minimum magnitude of tuned impedance 100 Ω). Both the normalized chirp produced by the AWGs and the normalized chirp transmitted by the transducer are shown in Fig. 10.2.

10.4 Results

In Fig. 10.3 both the measured (dashed gray line) and the simulated (solid black line) on-axis pressure signals are shown. The data presented in the figure clearly shows the similarity between both pulses allowing for the use of the simulated signal for decoding of the experimental signals.

Fig. 10.4 shows the decoded superharmonic chirp PSF. The result presented in the figure shows a smooth and distinct peak with low compression artifacts. The obtained SNR is $\sim$35 dB.

Fig. 10.5 details the normalized axial intensities of the third and superharmonic components. The dual pulse superharmonic profile was obtained using the optimal settings as reported by Matte et al. [2008a] and van Neer et al. [2009b] and was obtained using Gaussian apodized 2.5 cycle sine bursts with amplitude 60 V. This was also the case for the single pulse superharmonic and third harmonic profiles. The superharmonic chirp

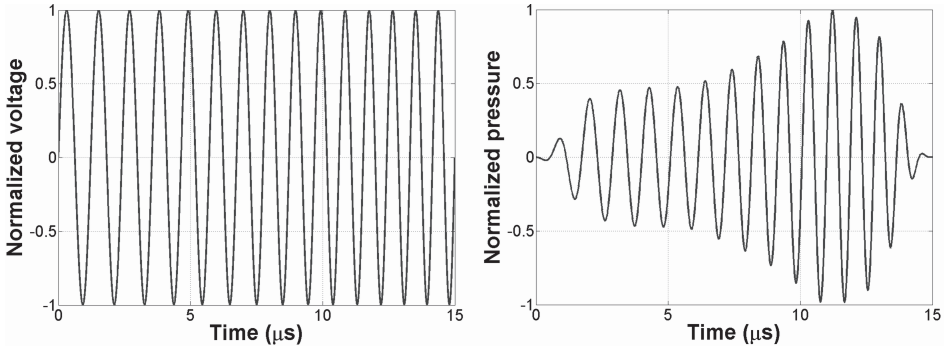

Figure 10.2: On the left the normalized chirp produced by the AWGs of the OPEN system. On the right the actual normalized chirp transmitted by the transducer, calculated using the transfer function.

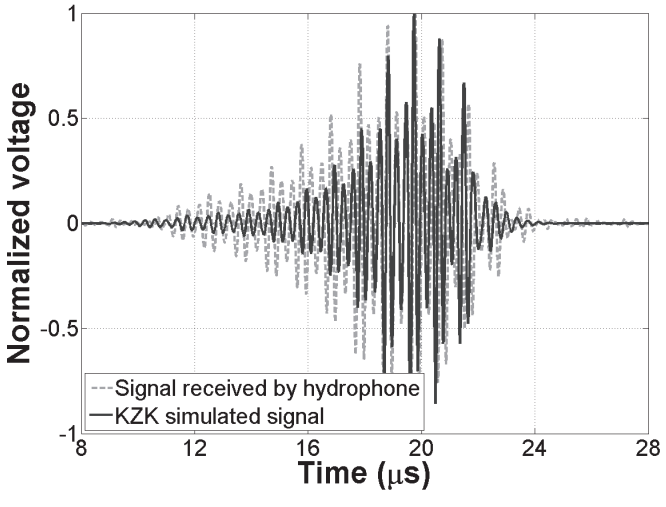

Figure 10.3: The on-axis pressure signal at focus. The dashed gray line displays the experimentally obtained data, the solid black line shows the KZK simulated signal.

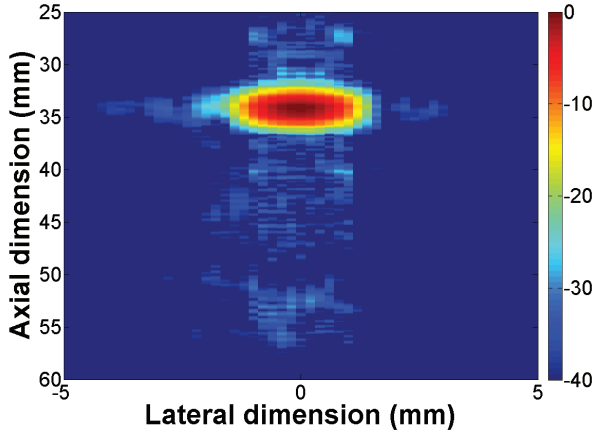

Figure 10.4: Decoded superharmonic chirp PSF. The relative intensity is color coded using a dynamic range of 40 dB. The transmitted signal was a 40% chirp with a 0.95 MHz center frequency and length 15 μs.

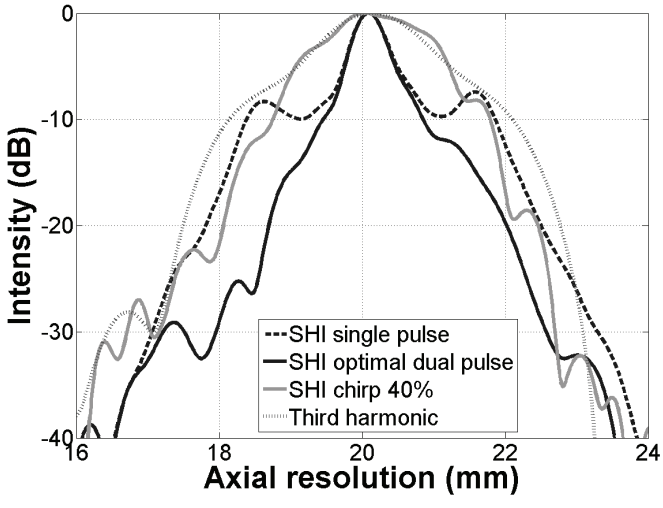

Figure 10.5: The normalized axial intensity profiles for the third harmonic and various superharmonic methods. The third harmonic, the optimal dual pulse [van Neer et al., 2009b] and single pulse superharmonic profiles are obtained using 2.5 cycle Gaussian apodized sine bursts with amplitude 60 V. The superharmonic chirp intensity profile was obtained using a 40% chirp with a 0.95 MHz center frequency and length 15 μs.

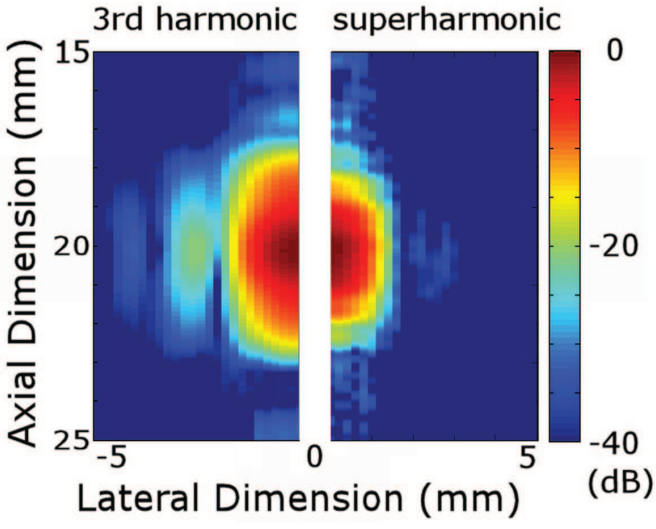

Figure 10.6: Comparison of the 3rd harmonic PSF obtained using 2.5 cycle transmissions (left panel) and the superharmonic chirp PSF (right panel). The relative intensity is color coded using a dynamic range of 40 dB. The third harmonic was obtained by exciting the transducer using a Gaussian apodized 2.5 cycle sine burst with amplitude 60 V.

profile was obtained using a 40% chirp with a 0.95 MHz center frequency and length 15 μs. From the figure, we see that the superharmonic chirp profile is reasonably smooth but does contain minor ripples. The axial lengths at the -6 dB level are 0.88 mm, 0.81 mm, 2.3 mm and 2.5 mm for the single pulse, optimal dual pulse and chirp superharmonic components and for the third harmonic component respectively. At the -20 dB level the axial lengths increase to 4.7 mm, 3.3 mm, 4.4 mm and 5.3 mm respectively.
Fig. 10.6 displays the third harmonic PSF obtained using a 2.5 cycle Gaussian apodized sine burst on the left and the superharmonic chirp PSF on the right using a dynamic range of 40 dB. The superharmonic chirp lateral beam widths at -6 dB and -20 dB were 1.8 mm and 3 mm respectively, whereas for the third harmonic these were 2.2 mm and 3.4 mm respectively. The axial beam widths at -6 dB and -20 dB were 2.3 mm and 4.4 mm respectively for dual pulse SHI and 2.5 mm and 5.3 mm for the third harmonic.

10.5 Discussion

The superharmonic PSF produced by the chirp protocol is smooth and almost completely free of ripples. However, as can be seen in Fig. 10.3, the decoding signal can still be improved - especially at the start of the signal there are significant differences between the experimentally recorded signal and the KZK simulated signal. The amplitude differences are likely caused by nonnegligible circuit effects and the phase differences are caused by

the phase transfer functions of the circuitry and the transducer.
The relative increase in the axial resolution obtained using the superharmonic chirp protocol amounts to 8% at the -6 dB level and 17% at the -20 dB level compared to the third harmonic. Whereas the relative increase in the lateral resolution obtained using the superharmonic chirp protocol is 18% and 17% at the -6 dB and -20 dB levels respectively compared to the third harmonic. If the axial resolution of the chirp superharmonic protocol is compared to the dual pulse superharmonic method reported previously [Matte et al., 2008a, van Neer et al., 2009b], we find a 65% decrease in resolution at the -6 dB level and a 25 % decrease at the -20 dB level. The lateral resolution produced by the superharmonic chirp method is equal to the lateral resolution of the dual pulse method at the -6 dB level and 12% higher at the -20 dB level. The intensity of the superharmonics is equally high (or higher) for the chirp excitation compared to the short burst excitation, but at 40% of the excitation voltage. Comparing the chirp and dual pulse protocols, there is a trade-off between the achievable resolution and the number of transmitted pulses per A-line. However, both imaging schemes produce a considerably better resolution than the third harmonic. It is expected that these resolutions will deteriorate somewhat in *in-vivo* situations, due to the imperfectness of the generated decoding signal (chirp method) and the influence of tissue attenuation (dual pulse method).

10.6 Conclusion

The PSFs produced by the superharmonic chirp protocol are virtually free from ripple artifacts and have increased spatial resolution compared to the third harmonic. However, the spatial resolution is lower compared to the dual pulse superharmonic method [van Neer et al., 2009b]. Thus there exists a trade-off between the attainable spatial resolution and the frame rate in superharmonic imaging.

Acknowledgements The financial support of the Dutch Foundation for Technical Sciences is greatly appreciated.

Part 4 : Enhancing harmonics of ultrasound contrast agents

CHAPTER 11

Multiple component second harmonic reduction signal, for reducing a broad 2^{nd} harmonic band of the propagating ultrasound wave

Mirza Pasovic, Mike Danilouchkine, Guillaume Matte, Antonius F. W. van der Steen, Olivier Basset, Nico de Jong, Christian Cachard

Published in Ultrasound in Medicine and Biology. May 2010.

Abstract Ultrasound contrast harmonic imaging and detection techniques are hampered by the harmonic distortion of the ultrasound wave due to the nonlinearities of the medium. To increase the discrimination between the tissue and ultrasound contrast agents at higher harmonics, we investigate a tissue harmonic suppression technique. The main attention of the research is the signal that is introduced at the source and is constructed out of several discrete frequency components from the second harmoinic band. Therefore, this method was coined as the multiple component second harmonic reduction signal or multiple component SHRS. By adjusting the amplitude and phase of discrete components and simultaneously propagating multiple component SHRS with the imaging signal, the nonlinear distortion of the ultrasound waveform is considerably reduced. Using the numerical simulation, the optimal parameters for multiple component SRHS were deduced. The simulations results were corroborated in the water-tank experiments and showed $40\,dB$ reduction with respect to the fundamental, covering up to $75\,\%$ of the entire second harmonic band. In the other series of experiments with the clinically used contrast agent, the uniform increase in agent-to-tissue ratio of $7.4\,dB$ over a relatively large region of imaging was observed. The use of the proposed method in the everyday clinical practice can improve discrimination between the tissue and the contrast agent in harmonic imaging.

11.1 Introduction

Ultrasound contrast agents (UCA) are small encapsulated gas-filled bubbles that enhance the backscattered echo of the ultrasound wave. Usage of UCA can be found in variety of the ultrasound medical applications like ultrasound imaging [Bouakaz et al., 2002a, Deng et al., 1998, Borsboom J, 2005, Burns, 1996, Schwarz et al., 1997], detecting the presence of the UCA [Porter et al., 1997, Ramon et al., 2005] or drug delivery [Bekeredjian et al., 2005, Ferrara et al., 2007]. The main goal of any ultrasound contrast detection or imaging technique is the discrimination between the perfused and unperfused area, which is quantitatively expressed with agent-to-tissue ratio (ATR) [de Jong et al., 2000, Bouakaz et al., 1998]

$$ATR = 20 \cdot \log\left(\frac{P_{UCA}}{P_{tis}}\right) \tag{11.1}$$

where P_{uca} and P_{tis} are the amplitude of the backscattered pressure by Ultrasound contrast agents and tissue respectively.

It is well established that UCA respond nonlinearly when exposed to ultrasound wave [de Jong et al., 1994, de Jong et al., Frinking and de Jong, Uhlendorf and C, 1994, Kameda and Matsumoto, 1999]. This opens an opportunity for detection and imaging of UCA at the higher harmonics. But UCA are not the only source of higher harmonics. Nonlinearities of the medium distort the propagating ultrasound wave so that the higher harmonics are generated from the surrounding tissue also [Hamilton et al., 1985, Hart and Hamilton, 1988, Kharin and Vince, 2004, Humphrey, 2000b]. To evaluate imaging and detection of UCA at higher harmonics, Eq.(11.1) is then changed to

$$ATR_n = 20 \cdot \log\left(\frac{P_n^{UCA}}{P_n^{tis}}\right) \tag{11.2}$$

Now P_n^{UCA} and P_n^{tis} present the amplitude of the backscattered pressure of the UCA and tissue at n-th harmonic respectively. In order to improve ATR_n, either P_n^{UCA} has to be increased or P_n^{tis} has to be reduced.

Techniques for increasing the ATR can be roughly distinguished into two categories. The first is intended at locating the contrast agents and enhancing their response upon insonification with an ultrasound wave (increasing the P_n^{UCA} in Eq. (11.2)). Kirkhorn et al. [2001] observed the loss of correlation in the backscattered echoes prior and following the micro-bubble destruction. Although this approach has been proven to be feasible, it does not allow the dynamical quantification of the up-take and wash-out of the contrast agents in perfusion protocols. The detection of the micro-bubble presence without their destruction can be achieved by means of combining harmonic and Doppler imaging techniques [Simpson et al., 1999]. A pulse-inversion scheme was applied to the conventional Doppler, followed by the dedicated harmonic post-processing. The contrast enhancement was achieved by quantifying the ratio between the linear and nonlinear scattering and further analysis of the Doppler shift of both scattering phenomena in the frequency domain. In spite of the increase in ATR, the conventional and pulse-inverted harmonic Doppler methods suffer from the decrease in the frame rate. Additionally, the flash artifacts typical for color Doppler imaging present a challenge. The same principle of pulse-inversion was applied by Shen and Li [2003] for contrast detection. However, the post-processing was performed in the temporal domain and intended to reduce the signal of the odd harmonics with simultaneous amplification of the even ones, namely the second harmonic. The same conclusion of increase of the second

harmonic generated by tissue after applying the pulse-inversion was made by Verbeek et al. [2000]. The detection of UCA can be also improved by taking into consideration the inherent property of an insonified micro-bubble to generate a so-called subharmonic response, when the spectrum of the backscattered ultrasound echos comprise frequency components at the half of the emitted [Shankar et al., 1998, Shi et al., 1999]. Yeh et al. [2008] considered a dual high-frequency difference excitation technique for contrast detection. A high-frequency wave, arising in the propagating medium as a sum of two frequency excitation bursts, contains the spectral component close to the UCA resonance frequency and is used for the excitation waveform. Its slow-varying envelope causes the consonant modulation of the micro-bubble oscillation. This scheme allows for amplification of the nonlinear scattering and attains high spatial resolution as the insonification occurs with the narrow-band high-frequency pulse.

The second group of techniques aims at the suppression of the harmonic tissue response (decreasing P_n^{tis} in Eq. (11.2)). The common feature of this category of methods is that they utilized the principle of so-called source pre-biasing. The later is based on the transmission of the additional high-frequency pulse along with the imaging one, to minimize the harmonic distortion. Those methods belong to either a passive or an active cancellation system. The example of the former is the system encountered in the work of Shen and Hsieh [2008]. The high-frequency suppression signal was induced by a so-called harmonic leakage, primarily stemming from nonlinearity of the imaging system [Shen and Li, 2001b]. The imaging protocol utilized a constancy of the phase shift between the emitted fundamental pulse and the leakage signal. The amplitude and phase of the imaging burst should be appropriately adjusted to achieve harmonic tissue suppression. Although the feasibility of this approach was demonstrated by the author, the level of suppression is suboptimal as it is impossible to generate a leakage signal with a desirable amplitude. The other methods, can be regarded as the active cancellation systems. Shen et al. [2007b,a] proposed simultaneous transmission of the fundamental and accordingly phase shifted third harmonic pulse. In this case the propagating wave contains two spectral components equal to the sum and difference of the emitted signal. The latter is used for cancellation of the tissue harmonic response. To implement such an imaging protocol in clinical practice a dedicated transducer is required. Currently, the only available that meet these requirements are the experimental probes for superharmonic imaging [Bouakaz et al., 2004]. A number of methods for active tissue harmonic cancellation is based on the computational model from Christopher and Parker [1991]. It involves pairing the linear propagation of the acoustical beam in the medium via the angular spectrum method with the additional correction for the nonlinearity, implemented as the solution to the Burgers' equation. The realistic physical phenomena of diffraction, attenuation, dispersion and finite amplitude distortion are taken into consideration within this model during forward and/or backward advancing of the emitted waveform. The main difference between these methods lies in the way how the source pre-biasing signal is computed. Krishnan et al. [1997, 1998] used a nonlinear scheme to predict the waveform in the focus, filtered out the second harmonic and linearly propagated it back to the surface of the transducer. The obtained signal was further inverted and mixed with

the imaging pulse to define the source pre-biasing signal. Christopher [1999] utilized nonlinear propagation scheme in both directions. The computed fundamental and second harmonic components on the surface of the probe defined the imaging pulse. In a recent work, Krishnan and Thomenius [2008] disregarded the nonlinear effect during the forward propagation as opposed to the Christopher's approach. The results reported in these contributions showed a great promise in the harmonic tissue suppression as they provided total control over the parameters of the imaging protocol and, thus, maximize the level of suppression. The disadvantage is, however, that the reduction of the tissue harmonic is achieved over a narrow band of the second harmonic. Recently, Couture et al. [2008] proposed a pulse-inversion protocol in combination with the time reversal approach. It is based on the principle of temporal invariance of the nonlinear wave equation as shown by Tanter et al. [2000]. The source pre-biasing signal is determined by time reversing the waveform reflected from an ideal scatter at a given depth. The backscattered echoes, after emission of time reversed signal and its inverted counterpart, are summed in the post-processing stage to achieve the tissue harmonic image with reduced second harmonic component. The inherent weakness of this method originates from the fact that the time-reversed signal is obtained from a certain imaging depth, resulting in a shallow depth of final reduction. Additionally, the practical implementation of this technique required transmission of long pulses, which eventually degrades the axial image resolution.

In this paper we propose a method that belongs to the active cancellation system for tissue harmonic suppression. Contrarily to the previously published studies, the source pre-biasing signal is constructed out of the discrete spectral components from the second harmonic band. Therefore, the method was dubbed as multiple component second harmonic reduction signal (multiple component SHRS). To achieve the optimal level of harmonic reduction both phase and amplitude of the discrete components should be properly adjusted. Using computer simulation and experiments we show that a broad-banded reduction can be achieved with our methods. Moreover, the axial depth reduction of the second harmonic compares favorably to the ones of the previous authors. The manuscript is organized as follows. The second section describes the method, simulation tools and experimental set-up. The results of simulations and measurements are presented in the third part of the paper. The last section is devoted to the discussion and comparison of the obtained results with ones published previously by the other authors.

11.2 Materials and methods

For the purpose of the method presentation, a continuous wave (CW) is regarded. At the surface of the transducer ($z = 0$), such a wave p, with amplitude pressure P_0 and frequency f_0, is defined as.

$$p(t, z = 0) = P_0 \cdot \sin(2\pi \cdot f_0 \cdot t) \tag{11.3}$$

During propagation in a nonlinear medium, p generates higher harmonics [Hamilton and Blackstock, 1998, Blackstock, 2000], such that at the focal distance $z = d$, ultrasound

wave can be presented as the sum of the harmonics

$$p(t, z = d) = \sum_{n=1}^{\infty} P_n \cdot \sin(n \cdot 2\pi f_0 \cdot t + \Phi_n) \tag{11.4}$$

where n corresponds to a particular harmonic, P_n is the pressure amplitude of the n-th harmonic and $\Phi_n = n \cdot 2\pi f_0 \Delta t_n$ is the phase of the n-th harmonic, defined from the time delay Δt_n between fundamental and n-th harmonic at zero crossing. In practical applications however, a pulse wave (PW) is transmitted. Such a signal exhibits an amplitude spectrum with energy inside a frequency band around f_0. After the nonlinear propagation the ultrasound pulse suffers harmonic distortion. The amplitude spectrum of the distorted signal is given on Fig.11.1. Notice that each harmonic is not defined by a single frequency with amplitude P_n, but by a frequency band B_n with a spectral energy E_n which is related to the surface under the curve. Local maximums on the Fig.11.1 correspond to the harmonic frequencies of the ultrasound pulse and a band of a particular harmonic (B_n) is defined as the frequency interval with amplitude $20dB$ lower than the local maximum. This threshold was chosen out of the following practical consideration. The achievable dynamic range of the ultrasound images is determined by the level of the fundamental in the main and grating lobes, and equals to $40\,dB$ [Cobbold, 2007]. The amplitude of the second harmonic is usually $20dB$ lower than the fundamental. Thus, suppression beyond $20\,dB$ of the second harmonic, levels the signal from this band with the lower boundary of the achievable dynamic range. The same criteria was considered in earlier published work of [Shen and Li, 2001a].

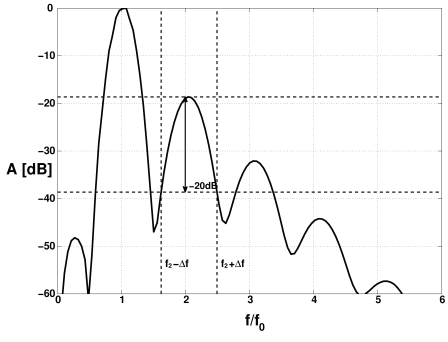

Figure 11.1: Amplitude spectrum of a finite duration signal after propagating in a medium. Note that the second harmonic band is defined by all the frequency components with amplitude $20\,dB$ lower than maximum component of the second harmonic

To reduce a broad second harmonic band the second harmonic reduction signal (SHRS), introduced at the source ($z = 0$) is composed of multiple components. A SHRS con-

structed with $2 \times m + 1$ components is defined by Eq.(11.5)

$$p_{SHRS}(t, z = 0) = P^*_{SHRS} \cdot \sum_{k=-m}^{m} \Pi^*_k \cdot \sin(2\pi(2f_0 + k \cdot \Delta f)t + \Phi^*_{SHRS}) \quad (11.5)$$

where $*$ indicates parameters whose values can be controlled. Each frequency component is separated by Δf and has a same phase Φ^*_{SHRS}. A normalized, dimensionless weighting function Π^*, is used to control the amplitude of the particular frequency component. By changing Π^* the transmitted energy of the multiple component SHRS (E_{SHRS}) is influenced. In the case when $m = 0$, single component SHRS is transmitted as proposed by previous authors [Krishnan et al., 1997, 1998, Christopher, 1999].

The imaging pulse and the multiple component SHRS simultaneously propagate in the medium and interact arround the focal zone. For the reduction of the second harmonic on a broader band B_2 at $z = d$, the following conditions have to be satisfied

$$\Phi_{SHRS} = \Phi_2 + \pi \quad (11.6)$$

$$E_{SHRS} = E_2 \quad (11.7)$$

$$P_{SHRS} = P_2 \quad (11.8)$$

Eq.(11.6) dictates the condition of the phase. From trigonometry it is well known that two signals cancel each other only if they are in perfect opposite phase. If this is not the case, the reduction is not optimal or even worse, the two signals can actually add and further increase the amplitude. To prevent such a scenario, Eq.(11.6) makes sure that in the region of interest the two signals oppose each other. Second condition (Eq.(11.7)) is added to control the applied weighting function Π^*. Energy E_{SHRS} emitted by the limited number of frequencies in the multiple component SHRS must be distributed throughout B_2, to affect a large second harmonic band. But, since Π^* is normalized and dimensionless, a third condition is added. Eq. (11.8) guarantees that the amplitude of the multiple component SHRS and second harmonic generated by the tissue are the same. If the P_{SHRS} is too large or too small the second harmonic is not optimally cancelled. Since P_2, Φ_2 and E_2 result from the propagation of ultrasound wave and depend on the investigated medium, the only possibility for successful reduction is to determine the values of P^*_{SHRS}, Φ^*_{SHRS} and Π^*, such that at $z = d$ all conditions (Eq.(11.6)-Eq.(11.8)) are met.

Calculation of the phase Φ^*_{SHRS}

To calculate the phase of the second harmonic generated by the tissue (Φ_2), quasi linear approximation was used [Dursun et al., Chen, 2007, Landsberger and Hamilton, 2001]. The second harmonic field was then estimated through the quasi-linear approximation of the nonlinear wave equation. This approach was implemented, since then there is no need to perform forward or backward propagation of the emitted signal. The ASM method slightly over estimates the amplitude of the second harmonic, while gives an accurate estimation of Φ_2. Phase of multiple components SHRS (Φ_{SHRS}) was then obtained by Eq.(11.6).

Calculation of weighting function Π^*

Angular spectrum method also provides information on the band of the generated second harmonic. Landsberger and Hamilton [2001] pointed out that through quasi-linear approximation the generation of the second harmonic can be viewed as the auto convolution of the emitted fundamental field in frequency domain. Broadening of the amplitude spectrum of the second harmonic is then well predicted and should be taken into consideration when calculating Π^*

$$\Pi^* = \frac{\underline{P}_0(f) \circledast \underline{P}_0(f)}{\max(\underline{P}_0(f) \circledast \underline{P}_0(f))} \tag{11.9}$$

where $\circledast$ denotes convolution and $\underline{P}_0$ denotes the frequency spectrum of the emitted pulse. The denominator is used to normalize the weighting function Π^*.

Calculation of amplitude P^*_{SHRS}

Various authors [Lee and Hamilton, 1995, Zemp et al., 2003, Yang and Cleveland, 2005], have shown that in the focal spot the pressure is amplified by the linear gain factor

$$G = \frac{f_0 \cdot w \cdot h}{c_0 \cdot d} \tag{11.10}$$

where w is the width and h is the height of the ultrasound transducer. To calculate P^*_{SHRS}, amplitude of the second harmonic P_2 generated during nonlinear propagation, must be divided by linear gain factor of the corresponding k-th frequency of the multiple component SHRS.

$$P^*_{SHRS} = \frac{P_2}{G(f_{SHRS_k})} \tag{11.11}$$

Effectively, the pressure amplitude of the second harmonic was scaled down by the linear gain factor. This assumption is valid, as the level of the second harmonic is approximately $20\,dB$ lower with respect to the fundamental. The similar approach was used by Krishnan et al. [1998], when the second harmonic signal in focus was filtered out and linearly backpropagated to the surface of the transducer.

It is also important to take into account the effect of the attenuation of the medium. Generally, the higher harmonics are more attenuated than the lower. In water, attenuation rises with the square of the frequency. This means that with doubling the frequency of the transmitted signal, the attenuation of the medium is 4 times higher. In biological tissue the relation is usually more linear. Since frequencies of the multiple component SHRS, are roughly twice that of the fundamental, they are also more attenuated. To compensate for the attenuation of the medium, the frequency power law presented by Szabo [1994] was used. The author presented a method, where any relation between the transmitted frequency and the attenuation of the medium can be modeled. By doing so, it is quite easy to estimate the attenuation coefficient of the particular component of SHRS. Including

Eq.(11.10) and Eq.(11.11) in Eq.(11.5) gives the final form of multiple component SHRS

$$P_{SHRS_k} = P_2 \sum_{k=-m}^{m} \frac{At(2f_0 + k\Delta f)}{G(2f_0 + k\Delta f)} \Pi_k^* \cdot \sin(2\pi(2f_0 + k \cdot \Delta f)t + \Phi_{SHRS}^*) \quad (11.12)$$

where $At(2f_0 + k\Delta f))$ is the attenuation of particular k-th component, calculated as proposed by Szabo [1994].

11.2.1 Simulation implementation

The simulation of ultrasound propagation is based on the KZK equation [Zabolotskaya and Khokhlov, Kuznetsov, 1970] for rectangular transducer

$$\frac{\partial p}{\partial z} = \frac{c_0}{2} \int_{-\infty}^{t'} \Big(\frac{\partial^2 p}{\partial x^2} + \frac{\partial^2 p}{\partial y^2} \Big) dt + \frac{D}{2c_0^3} \frac{\partial^2 p}{\partial t'^2} + \frac{\beta}{2\rho_0 c_0^3} \frac{\partial p^2}{\partial t'} \quad (11.13)$$

where p is the pressure, t' is the delayed time coordinate, x is the lateral coordinate, y is the elevation coordinate and z axial distance. Diffusivity of the medium is defined by D, c_0 is the speed of sound, ρ_0 is the density of the medium and β is the nonlinearity parameter of the medium. Eq.(11.13) accounts for the absorption and nonlinearity of the medium and the diffraction effect due to the finite size of the transducer. A finite difference method, proposed by Voormolen [2007] was implemented as a solution of Eq.(11.13). The defined geometry of the ultrasound probe used in simulation, was that of a focused phase array (FPA) probe with 64 elements whose height and width were $12.5\,mm$ and $230\,\mu m$ respectively. The spacing between the elements was $k_{erf} = 80\,\mu m$. The excitation was configured such that odd elements transmitted the imaging pulse p_0 ($f_0 = 1.5\,MHz$, $P_0 = 500\,kPa$, number of cycles $N_{cyc} = 3$) while even elements emitted the SHRS signal. The signals were propagated through the medium with parameters set to match those of water (density of water $\rho = 998.2kg/m^3$, nonlinear parameter $\beta = 3.5$, speed of sound $c_0 = 1483m.s^{-1}$).

11.2.2 Experimental set-up

The simulation results were corroborated in the water-tank experiments. An ultrasound scanner (OPEN System, LeCoeur Electronique, Chuelles, France Vignon et al. [2005]), which offers the possibility to program an arbitrary excitation signal (frequency, phase, amplitude, envelope) of each element separately, was used to drive a cardiac ultrasound transducer (Vingmed 2.5 FPA, KG100001,General Electric Co., OH, USA, 64 elements, height 12.5 mm, width of element $230\,\mu$ m and $k_{erf} = 80\,\mu$m). The transducer was mounted on the side of a water-filled tank. Using a xyz-system, a needle tip hydrophone (0.2 mm in diameter from Precision Acoustic, Dorchester, UK) was manoeuvred to the focal spot ($z = 70$ mm). The hydrophone was connected to the LeCroy oscilloscope (9400A, Lecroy, Geneva, Switzerland). The acquired time traces were sampled with the sampling frequency $f_s = 100$ MHz and stored on a computer for further processing.

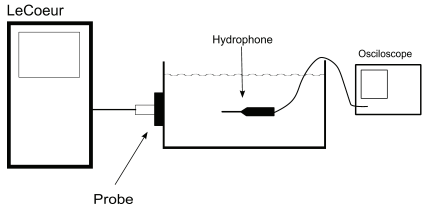

Figure 11.2: Experimental setup used in measurements with hydrophone

The transmit efficacy of the phased array transducer as well as the nonlinearity of the electronics may play an essential role in the practical implementation of the multiple component SHRS. Prior to experiments, the transmit transfer function of the probe was determined using a calibrated hydrophone in a similar way as described in van Neer et al. [2007]. The measurements showed that the used ultrasound transducer had the center frequency at $f_c = 2.5\,MHz$ in accordance with the probe specification and an $80\,\%$ band width at $-10\,dB$. Knowing this function, the excitation frequency of the imaging pulse and its second harmonic frequencies were placed slightly asymmetrically with respect to the center frequency of the transducer. By doing so the maximal transmit efficacy of the highest spectral component of the reduction signal was achieved. The fundamental frequency was then equal to $1.5\,MHz$, while the second harmonic amounted to $3.0\,MHz$. Appearance of the higher harmonics in the acoustic wave not only occurs during propagation in medium, but also can be induced by nonlinearities of the piezoelectric materials, used in the manufacturing of the transducer elements, and the harmonic distortion of the amplifiers in the imaging equipment.For the excitation voltages in the frequency range used in the experiments, the nonlinearity of the piezoelectric materials can be neglected. The harmonic distortion of the amplifiers of LeCoeur OPEN System was also investigated. The testing showed that those distortions can be disregarded. The same conclusion was drawn by Couture et al. [2008], who used the similar imaging system in their experiments.

The performance of multiple component SHRS was further tested on a specially designed set-up, adapted for the ultrasound contrast imaging. A tissue mimicking phantom was designed as presented by Teirlinck et al. [1998]. The phantom consisted of $11\,\%$ glycerol, $3\,\%$ agar and $2\,\%$ of aluminium powder Al_2O_3 with grain size $0.3\,\mu m$ and $3\,\mu m$ as scatterers ($1\,\%$ each). The remaining $84\,\%$ of the phantom comprised of degassed water. The mixture was carefully boiled in an oven until the surface started raising. After that, it was poured into a square shaped mold so that the substance could cool to the room temperature. During the cooling process, great caution was taken to assure the phantom of being homogeneous. Once at the room temperature it was cut in two pieces. Since during the preparation the homogeneity of phantom was not compromised, it can

be presumed that the two parts had same characteristics. In next step, the two parts were placed at the bottom of a water tank, separated by $2\,cm$. This was done so that the UCA (Definity©), diluted to the concentration of 10^5 micro-bubbles$/ml$, could be easily administrated. During the acquisition of the ultrasound images, the solution with UCA was constantly stirred to maintain a uniform distribution of the micro-bubbles (Fig. 11.3).

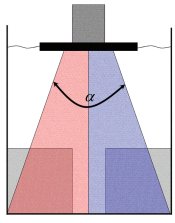

Figure 11.3: The measuring procedure implemented for performing ultrasound contrast harmonic imaging. On top was ultrasound transducer whose surface was only slightly submerged in the water. The red area presents the region where imaging signal and multiple component SHRS were transmitted together, while blue area was scanned only with imaging signal. The two gray squares present the tissue mimicking phantoms, separated by $2\,cm$. Ultrasound contrast agents were added to the water, having the concentration of 10^5 micro-bubbles$/mL$

The aforementioned acquisition equipment and phased array transducer were used in the pulse-echo mode to collect imaging data in the contrast experiment. Each acquired frame consisted of 60 lines, sweeping the scanning angle of $\alpha = 60°$. The acquisition equipment allowed acquiring a frame where 30 lines had imaging signal and multiple component SHRS in excitation and 30 lines with only imaging signal. This procedure was implemented so that the conditions during the acquisition were identical when there is no reduction signal and when multiple component SHRS was part of the excitation (Fig. 11.3). The acquired echoes were processed in Matlab© using a digital bandpass filter. A 3^{rd} order Butterworth filter, with cutoff frequencies $f_{c1} = 2.5\,MHz$ and $f_{c2} = 3.5\,MHz$, was chosen.

11.3 Results

11.3.1 Simulation results

In order to get a deeper insight into the 2^{nd} harmonic reduction with the transmission of the multiple component SHRS, first the impact of the reduction with a single frequency component SHRS ($m = 0$ in Eq.(11.5)) was estimated. Imaging signal and single component SHRS were propagated until the focal distance $z = 70$ mm. Three sets of simulations were conducted, with single component SHRS frequency set to $f_{SHRS} = 2.8$ MHz then changed to $f_{SHRS} = 3.0$ MHz and finally to $f_{SHRS} = 3.2$ MHz.

Fig. 11.4 presents the amplitude spectrum of p_0 without SHRS (dashed line) and with the single component SHRS (full line). By defining the energy E_2 as the surface under the curve of the amplitude spectrum, it can be noted that by emitting 3.0 MHz as a single component SHRS, E_2 was lowered by 13 dB. Furthermore, the successful reduction of the second harmonic was considered only the frequency band where the amplitude spectrum was reduced by 20 dB of the maximum component inside the second harmonic band (below horizontal dash-dotted line). Then, From Fig.11.4 it can be concluded that the reduction of the second harmonic was attained around the corresponding emitted component in a narrow-banded range.

To achieve a broader spectral suppression of the second harmonic generated during propagation, the SHRS must be constructed out of multiple frequency components inside the second harmonic band. Since a single discrete frequency component resulted in the reduction of $15 - 20\,\%$ of the band, at most 7 components are needed to yield the reduction of the second harmonic over the entire band. In the experiments described hereafter, the frequency range for the multiple component SHRS were chosen between $2.7\,MHz$ and $3.3\,MHz$ with the frequency distance between each component $\Delta f = 0.1\,MHz$. The amplitude and phase of multiple component SHRS were calculated as described in Method and Materials section.

Fig. 11.5 shows p_0 at the focal distance without the reduction signal (dashed line) and with multiple component SHRS (full line). The positive and negative amplitude peaks were more similar since in this case the harmonic distortion of the propagating pulse was reduced. Comparison of the amplitude spectrums in Fig. 11.4 and on Fig. 11.5 clearly shows that a larger second harmonic band was influenced when a multiple component SHRS was used for reduction. Successful reduction covered $65\,\%$ of the second harmonic band. Some frequency components (above 3.0 MHz) did not fall below the defined reduction level. However, they were further reduced by 8 dB compared to Fig. 11.4b. With the transmission of multiple component SHRS, energy of the second harmonic band was reduced by 23 dB.

Fig. 11.6a presents the axial beam profile of the second harmonic amplitude in absolute values. When no reduction signal was added to p_0 (dashed line), the nonlinearity of the tissue cause the 2^{nd} harmonic to increase with the propagation distance. After propagating $3\,cm$, the 2^{nd} harmonic sharply increased and reached its maximum (78 kPa) at the focal distance. After the focal point, the 2^{nd} harmonic gradually fell. When multiple component SHRS was part of excitation (full line), in the near field the 2^{nd} harmonic was higher (12 kPa) than when no reduction signal was emitted. Indeed, the multiple component SHRS introduced the 2^{nd} harmonic frequency in the medium from the beginning of the propagation until the focal zone where the reduction was effective. By transmitting the multiple component SHRS together with p_0, it can be observed that the 2^{nd} harmonic was almost below $20\,kPa$ over the whole axial profile and even below $10\,kPa$ in the focal area. Fig. 11.6b shows the 2^{nd} harmonic normalized to the fundamental, according to axial distance z. The reduction was efficient on a large axial length. Fig.11.6b reveals that the reduction was maintained in a range of $10\,dB$ above maximal reduction (23 dB) on an axial distance of 4.1 cm around focal spot.

11.3.2 Measurement results

A set of experimental measurements was carried out to measure the reduction of the 2^{nd} harmonic with single component SHRS. Fig. 11.7a compares the amplitude spectrum of the signal at the focal distance, collected by the hydrophone, without the reduction signal (dashed line) and with single component SHRS (full line).

When single component SHRS frequency was $2.8\,MHz$ (Fig.11.7a), a narrow band around 2.8 MHz is affected, while other components of 2^{nd} harmonic band were almost unchanged. By transmitting 3.0 MHz as a single component SHRS (Fig.11.7b), only a part of the second harmonic band was successfully reduced (by $> 20\,dB$), while other components where less influenced. In the case when single component SHRS was 3.2 MHz (Fig.11.7c), again only a narrow band around the transmitted SHRS frequency was reduced.

Then multiple component SHRS was constructed as described previously. On Fig. 11.8 is the time trace and the amplitude spectrum of the imaging signal without reduction signal (dashed line) and with multiple component SHRS (full line) at $z = 70\,mm$. In later case, the energy of the second harmonic was decreased. As a consequence, harmonic distortion of the signal was reduced. This can be noticed on the time trace (Fig.11.8a) as the negative and positive peak pressures of the signal were more symmetric, which was not true when no reduction signal was transmitted. Reduction of the second harmonic with multiple component SHRS can be more obviously appreciated in the frequency domain (Fig.11.8b). Successful reduction of the second harmonic with multiple component SHRS was achieved on $75\,\%$ of the second harmonic band.

Axial profile of the second harmonic without and with multiple component SHRS was also measured (Fig. 11.9). This was done by moving the hydrophone along the axial axis in step of 0.5 mm, with the nearest point to the transducer set to 2 cm. At each measurement point, 30 time traces were collected and averaged. The dashed line corresponds to the second harmonic of p_0 without SHRS and full line corresponds to the situation when imaging signal and multiple component SHRS were transmitted simultaneously. Imaging signal alone caused the 2^{nd} harmonic to start raising fast after 3 cm. It peaked ($\approx$72 kPa) at 6 cm and after that kept falling with increasing distance. When multiple component SHRS was added to imaging signal, on the axial range between 3 cm and 10 cm the 2^{nd} harmonic was reduced to 20 kPa and in the focal spot (between 6 cm and 8 cm) even below 10 kPa. Fig.11.9b shows the second harmonic normalized to the fundamental. At the focal spot the multiple component SHRS reduced the second harmonic by 23 dB. The axial range where the multiple component SHRS sustained 10 dB of the maximum reduction corresponds to about 5 cm. The results acquired during experimental measurements with hydrophone, have confirmed the results predicted with simulation.

11.3.3 Ultrasound contrast harmonic imaging

Fig. 11.10 presents an acquired B-mode ultrasound contrast harmonic image, with dynamic range set to 35 dB. Region defined by red and blue window of size $2 \times 2\,cm$

correspond to the tissue mimicking phantoms, while green window presents the region containing the UCA. When there was no SHRS in the excitation (blue box on Fig.11.10 denoted with letter C), more backscattered signal from the tissue can be noticed, compared to the red box, where multiple component SHRS was added to the imaging pulse. Consequently, red box area appears darker compared to the area surrounded by blue box. Since the two phantoms were exactly the same in composition, the reduced second harmonic was a direct consequence of multiple component SHRS.

As a quantitative evaluation of the improvement obtained with multiple component SHRS, ATR_2 was calculated. All together 120 frames were acquired. By reducing the second harmonic with multiple component SHRS, the overall improvement of ATR_2 was $7.4 \pm 0.06\,dB$.

11.4 Discussion

There exists no consensus among the published works with respect on how to quantify the performance of the suppression methods. In the current study, two criteria were adopted. The first one is the axial depth of suppression. It seems that most of the authors adopt the idea of the intensity drop of the second harmonic, after the application of the suppression method. Krishnan and Thomenius [2008] firstly introduced a quantitative criterion and required an arbitrary minimization of $25\,dB$ with respect to the fundamental along the axial length of at least $4\,cm$. The second criterion to quantify the harmonic suppression method, is to consider the percentage of the second harmonic band that is being reduced. It was applied in the work of Krishnan et al. [1998] and in a more recent work of Couture et al. [2008] without any quantification. In the present study, the successful suppression is considered only if the spectral content at a particular frequency drops beyond $20\,dB$ with respect to the generated second harmonic without applying SHRS or by approximately $40\,dB$ with respect to the fundamental. These criteria are going to be used for discussion and further comparison of ours and previously reported results.

The axial depth of the suppression is a rather important parameter, that indirectly characterizes the applicability of the methods in the clinical practice. Most of the authors [Krishnan et al., 1998, Christopher, 1999, Couture et al., 2008] noticed the prominent level of second harmonic suppression is achieved in the local vicinity (from few millimeters up to one centimeter) of the focal point. The efficacy of the reduction methods was less pronounced outside this region. Krishnan and Thomenius [2008] established and succeeded in reducing the tissue harmonic level by $25\,dB$ with respect to fundamental over the length of $4\,cm$. Adhering to their idea, our results have demonstrated that the axial suppression depth increased by a factor of 2 and amounted to $8\,cm$. Hence, our method compares favorably with the previously published results.

The percentage of the suppressed band plays an equally significant role. Indeed, the harmonic response of the micro-bubbles, as well as harmonic generation of the tissue is not restricted to a single frequency component. In the work of Krishnan et al. [1998] the theoretical possibility of a broad-band tissue harmonic reduction was demonstrated

in the simulations. The experimental results were rather modest. The second harmonic reduction occurred in the narrow-band frequency range of $200\,kHz$ (or $12-15\,\%$ of the entire band) below the level of $40\,dB$ with respect to the fundamental. Couture et al. [2008] clearly demonstrated that their method had a better performance in this respect. The rough level of suppression between $37\,dB$ and $41\,dB$ for the entire band was presented. However, relatively long pulses were used for imaging and, thus, the bandwidth of the suppression was primarily determined by the band of the imaging pulse rather than the one of the transducer. Our strategy employs a reduction signal, composed out of the discrete components from the entire second harmonic band. In the current study we clearly showed that the broad-band suppression of approximately $75\,\%$ is feasible in the experimental conditions.

To achieve optimal tissue harmonic suppression with the presented method, it is equally important to choose the right number of the discrete components for SHRS. In the current study we adhere to the empirical considerations. Both, simulation and experimental results have demonstrated that source pre-biasing with a single component yielded suppression of the $15-20\,\%$ of frequency band around the corresponding component. Since a 3-cycle apodized sinus burst was used, the maximal band was primarily determined by the transmit transfer function of the transducer at the established level of suppression. Hence, to achieve the suppression of the entire second harmonic band, one would require at least 7 spectral components. A larger number of components would not have a tremendous effect on the suppression of the second harmonic. In general this choice depends on the length of the imaging pulse and is limited by transducer characteristics. For short bursts, the bandwidth of the transducer will be the contributing factor, while for longer imaging pulses, the narrower band should be suppressed and, thus, the number of components can be less. In ending, the number of the components for different pulse lengths can be detected during the probe calibration and further used in the clinical protocol.

Another physical phenomena that can influence the choice for the number of components in the reduction signal, is the dispersion of the medium. Wear [2000] showed that dispersion can prolong the transmitted pulse, hence alter the spectral content of the generated second harmonic. Since a longer signal has a narrower band, a fewer number of components of SHRS would be needed for the reduction in a highly dispersive medium. In our study a worst case scenario was considered (second harmonic generated with maximum bandwidth) by neglecting the dispersion. This is a permissible assumption, since the dispersion is usually weak. This has been proven in the simulations and experimental measurements conducted in water tank. Also, the ultrasound imaging performed on a tissue mimicking phantom suggests that the effect of the dispersion can be neglected.

In this and earlier studies it was demonstrated that the tissue harmonic suppression can used for enhancement of the ATR. The previously published results by Couture et al. [2008], reported a $10\,dB$ increase in ATR. Nevertheless, it is not clear from the paper how the value of this parameter was computed. As we have presented an improvement of ATR over a certain area, an adequate comparison in terms of average statistics between two techniques seems to be more relevant. The regression analysis of the intensity curves with

and without contrast in Fig.12(c) from the manuscript of Couture et al. [2008], revealed the average ATR improvement of $7.5 - 7.8\,dB$ in the region anterior to the vessel. The area of this region was equal to $0.4 \times 0.64\,cm$ assuming the isotropic spatial resolution. Taking into consideration the aforementioned arguments, the results reported in Couture et al. [2008] appeared only slightly better in the area of optimal suppression, while our statistics is calculated over a 16-times larger region. One of the possible explanations of the aforementioned difference can be the attributed transducer used in the experiment in spite of the fact the imaging equipment was the same. Although these two methods are strikingly different from the methodical point of view, the experimental results for contrast enhancement turned out to be comparable.

In our experiment the multiple component SHRS protocol was implemented on the broad-band phased array transducer. The fractional bandwidth was just sufficient enough to transmit signals at fundamental and several components out of the second harmonic bands. This implementation, however, is suboptimal as the transmit efficacy of the highest second harmonic component is rather low. It would be beneficial to used a dedicated phased array probe for this purposes. One of the suitable alternatives is the properly tuned phased array for superharmonic imaging, proposed by Bouakaz et al. [2004]. The probe consists of the low and high frequency interleaved subarrays. In transmission, the imaging signal and multiple component SHRS are split such that low frequency elements transmit imaging signal, while high frequency elements emit multiple component SHRS. The other possibility is to use the cMUT technology [G et al., 2005]. Ultrasound cMUT probes have shown to have even larger than $80\,\%$ bandwidth. One drawback of cMUT probes is that they also emit a significant amount of second harmonic [Lohfink and Eccardt, 2005, Lohfink and PC, 2005] due to their nonlinear behavior. But recently Novell et al. [2009]have presented a method to decrease the amount of contaminating second harmonic. So approach proposed by Novell et al. [2009] coupled with multiple component SHRS might be a very promising idea.

Our method inherits the potential weaknesses of all source pre-biasing techniques. To achieve the optimal level of suppression the amplitude and phase of the reduction signal have to be carefully chosen. In a clinical situation, when this technique is applied for obtaining the scans of different anatomical organs, the level of tissue harmonics can vary considerably. It would be determined by the tissue properties such as nonlinearity coefficient and frequency-dependent attenuation. The phase of the emitted waveform can be a subject to aberration as it travels through the inhomogeneous layers of different biological tissue types. Christopher [1999] suggested to use a database of precomputed pre-biasing signals for ”standard” clinical application. However, the approach does not incorporate the individual anatomical aspects of a patient. A very elegant solution was proposed by Krishnan et al. [1998], who adhered to the idea of providing a full control over the amplitude to the end-users of a clinical system and correct for potential phase discrepancies by taking into account the phase transfer function of the transducer. However, the effect of phase aberration was disregarded from consideration. Christopher [1999] showed that by correcting for this phenomenon (phase aberration) the level of tissue harmonic suppression can be further optimized. Hence, our final recommendation

for the practical realization of the method would involve the manual control over both parameters, amplitude and phase of the multiple component SHRS.

11.5 Conclusion

The higher harmonics generated by the nonlinearities of the medium mask out the echoes of the ultrasound contrast agents. They are generally considered contaminant and should be suppressed. This work focused on suppression of the tissue second harmonic based on an active noise cancellation principle. The suppression signal is constructed out of multiple discrete components from the second harmonic band. Its propagation together with the imaging pulse, considerably reduces the finite-amplitude distortion of the transmitted waveform. The use of this technique in the clinical practice can improve and facilitate detection and imaging of UCA.

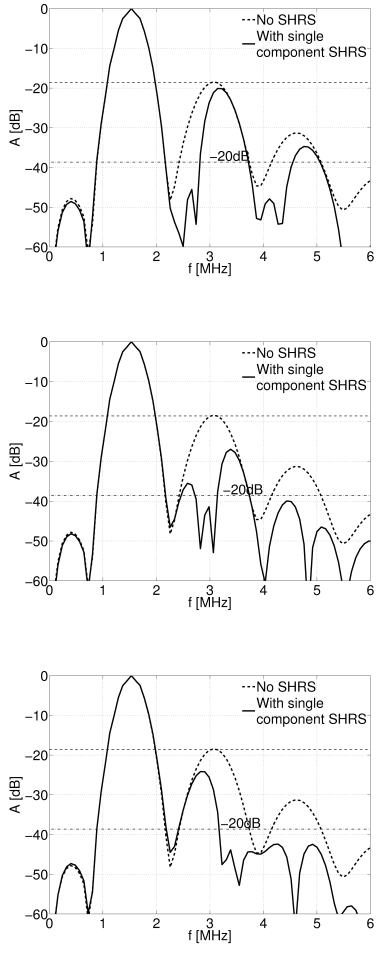

Figure 11.4: Amplitude spectrum of the imaging signal without (dotted line) and with single component SHRS (full line) at focal point after propagation in water (density $\rho = 998.2kg/m^3$, nonlinear parameter $\beta = 3.5$, speed of sound $c_0 = 1483m/s$). With transmission of $2.8\,MHz$ frequency (Fig.11.4a) only a narrow band around that component is influenced. Same observation can be made for the when $3.0\,MHz$ (Fig 11.4b) and $3.2\,MHz$ (Fig. 11.4c) where used for reduction of the second harmonic band

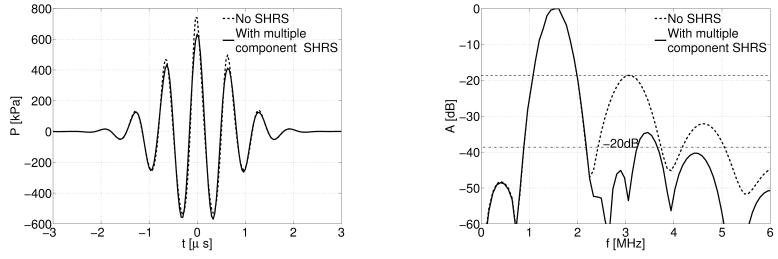

Figure 11.5: Time trace (Fig.11.5a) and the amplitude spectrum (Fig. 11.5b) of imaging signal at focal distance, when no reduction is added (dashed line) and when multiple component SHRS is part of excitation (full line)

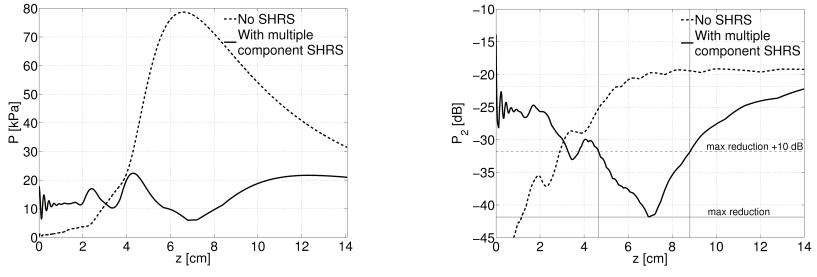

Figure 11.6: Simulated second harmonic axial profile when SHRS is not part of excitation (dashed line) and when multiple component SHRS is part of excitation (full line) in absolute values (Fig.11.6a) and normalized to the fundamental harmonic (Fig. 11.6b).

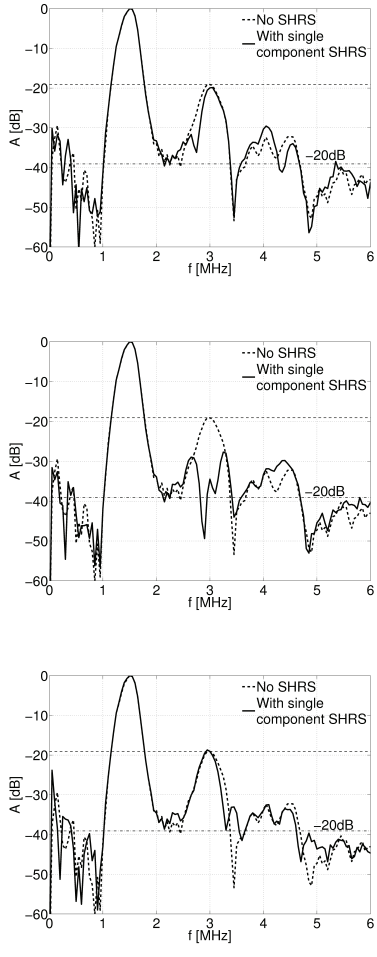

Figure 11.7: Amplitude spectrum of a signal collected by a hydrophone placed $70\,mm$ from the transducer. Dashed line is presenting amplitude spectrum of the signal when SHRS is not part of the excitation while full line is presenting amplitude spectrum when SHRS is part of excitation. Three sets of experiments were conducted with frequency of single component SHRS being $2.8\,MHz$ (Fig.11.7a) then $3.0\,MHz$ (Fig.11.7b) $3.2\,MHz$ (Fig.11.7c). Notice how in all cases only a narrow band of the second harmonic is affected.

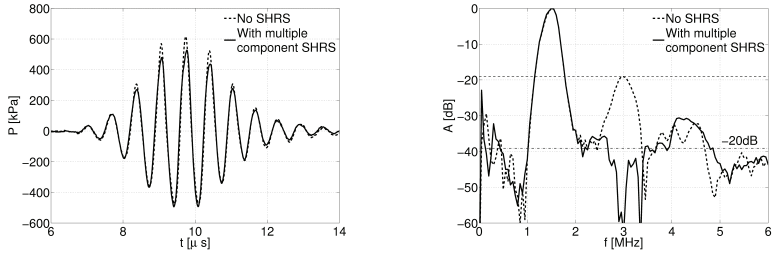

Figure 11.8: Measured time trace (Fig.11.8a) and the amplitude spectrum (Fig. 11.8b) of the imaging signal without SHRS (dashed line) and with multiple component SHRS (full line) added in transmission, collected by the hydrophone $70\,mm$ from transducer.

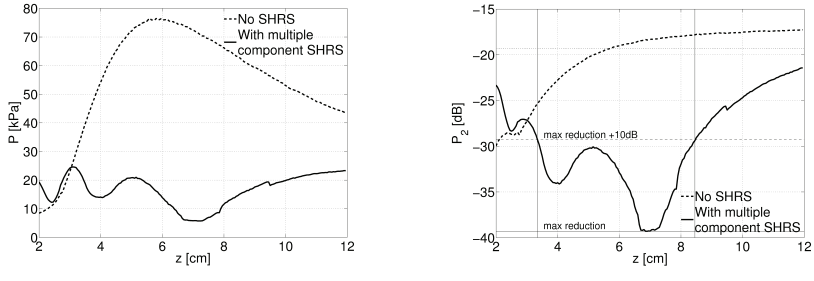

Figure 11.9: Measured axial profile of the 2^{nd} harmonic in absolute value (Fig.11.9a) and normalized to the fundamental (Fig.11.9b), when multiple component SHRS is not part of excitation (dashed line)and when SHRS is part of excitation (full line).

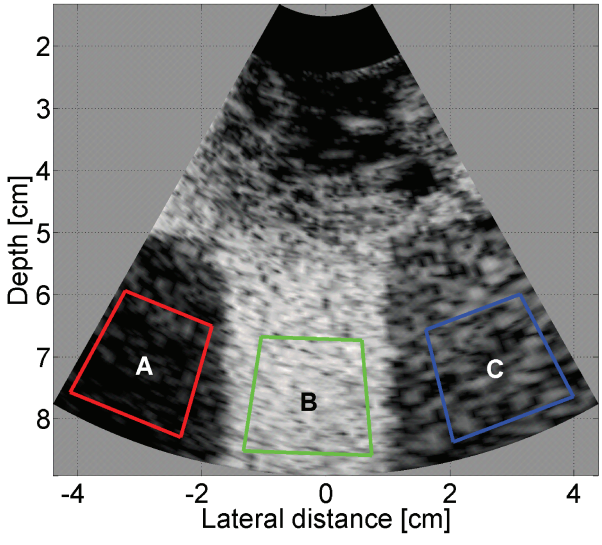

Figure 11.10: An acquired ultrasound contrast harmonic image. The red and blue windows (A and C) present the area of tissue mimicking phantom used for calculation of ATR, while area limited with green window is the water perfused with UCA

CHAPTER 12

Improved ultrasound contrast agent detection in a clinical setting

Marcia Emmer, Guillaume Matte, Paul van Neer, Annemieke van Wamel, and Nico de Jong

IEEE Ultrasonics Symposium, 2007, 2235-2238

Abstract Optical studies have shown threshold behaviour of phospholipid-coated contrast agent microbubbles. Below the acoustic pressure threshold, phospholipid-coated microbubbles oscillate significantly less than above the threshold. For microbubbles smaller than 3.0 μm diameter, pressure-dependent scattering was measured, which is believed to be the result of threshold behaviour. The aim of this study is to investigate if threshold behaviour is useful to enhance the contrast in power modulation images. For levovist and BR14 suspensions (filtered and native), a programmable ultrasound system recorded power modulation images at 2 MHz and acoustic pressures between 25 and 250 kPa. Results were compared to intensities recorded with a commercial ultrasound system. An inverse relationship between the pressure-dependency of the scattering and microbubble size was observed. Threshold behaviour enhances the contrast in power modulation images. Using a suspension with microbubbles smaller than 2.0 μm, at 2 MHz transmit frequency and an acoustic pressure of 250 kPa, the CTR value was 33 dB, which is 13 dB higher compared to a native BR14 suspension.

12.1 Introduction

High-speed optical recordings of individual microbubbles revealed threshold behaviour for phospholipid-coated microbubbles with sizes smaller than 5.0 μm in diameter [Emmer et al., 2007a]. In these recordings, the onset of microbubble vibration was investigated. Although, current descriptions of microbubble behaviour predict a linear relationship between relative expansion of off-resonance encapsulated microbubbles and low acoustic pressures, this was not found for microbubbles smaller than 5.0 μm diameter. For these microbubbles, acoustic pressure had to increase above threshold values ranging from 30 to 120 kPa for the individual microbubbles before their response was proportional to the acoustic pressure applied. These observations may be explained by size-dependent mechanical properties of the phospholipid shells.

The effects of threshold behaviour are also observed acoustically [Emmer et al., 2006, 2007b]. In contrast to the "free" microbubble Levovist, phospholipid-coated microbubbles show pressure-dependent attenuation. It is believed that threshold behaviour is typical for phospholipid-coated contrast agents and that it explains the pressure-dependency of the contrast agents attenuation. At low acoustic pressures, only a selection of microbubbles oscillates significantly and absorbs acoustic energy. When the acoustic pressure is increased, the pressure threshold of more microbubbles is exceeded leading to an increased attenuation.

Threshold behaviour is related to size. The scattering as a function of acoustic pressure of mechanically filtered microbubble suspensions has been studied [Emmer et al., 2007b,c]. Suspensions without microbubbles larger than 3.0 μm diameter showed pressure-dependent scattering, which is different from the pressure-independent scattering of a native suspension. For filters with other pore sizes, this has not been investigated yet.

The occurrence of threshold behaviour is useful for an imaging technique such as power modulation imaging. This technique operates by sending two pulses into the body, which are equal in shape, but have different amplitudes. Based on the scaling property of linearity, the linear responses of tissue and bubbles can be cancelled to obtain the harmonic echoes of the bubbles alone. When only small bubbles are used, the presence of threshold behaviour could be exploited to enhance the contrast between tissue and bubbles.

The aim of this study is to investigate if threshold behaviour enhances the contrast in power modulation images. Secondly, the influence of microbubble size on the pressure-dependency of scattering was studied. For this purpose, a programmable ultrasound system was used. Recorded intensities are compared to intensities recorded with a commercial ultrasound system.

12.2 Materials and methods

A water tank was filled with degassed water (Fig 12.1). At the bottom of the tank an acoustic absorbing pad was placed to reduce the influence of reflections. On this pad

a tissue-mimicking phantom was placed. The phantom was prepared by adding 5 g of agar powder (Boom, Meppel, The Netherlands) and 0.5 g of scatterers (Carborundum No. 600, Cats, Hoogvliet, The Netherlands) to 250 ml deionised water. A ring stand and clamp held the 2.5 MHz phased array transducer, which was connected to a commercial ultrasound system (GE/VingMed System 5, Horton, Norway) or a 128 channels programmable ultrasound system (OPEN system, Lecoeur Electronique, Chuelles, France). The focal distance was 5.0 cm.

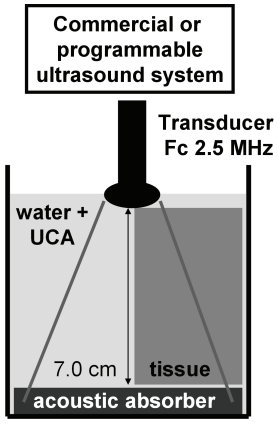

Figure 12.1: Experimental setup to record the scattering of contrast agent suspensions (UCA) and a tissue mimicking phantom.

Different suspensions of contrast agent were added to the water tank. The phospholipid-coated contrast agent BR14 (Bracco Research SA, Geneva, Switzerland) was compared to the "free" contrast agent Levovist® (Schering AG, Berlin, Germany). BR14 was applied unmodified (native) and mechanically filtered by gravity drainage through a porous polycarbonate membrane with 2.0, 3.0 or 5.0 μm pore size (GE Osmonics Inc., Minnetonka, MN). Concentrations of the suspensions are given in Table 12.1.

On each contrast agent suspension, a series of recordings with both ultrasound systems was performed. A magnetic stirrer refreshed the microbubbles in the scanning plane between frames. The commercial ultrasound system was set at a frequency of 2.0 MHz and recorded subsequent B-mode images at powers from -30 to -10 dB at a repetition rate of approximately 1 s. The programmable ultrasound system transmitted pulses composed by unipolar square wave transmitters. Voltages from 5 to 20 V were applied. The system was programmed to operate in a power modulation mode at 2.0 MHz. The first pulse was fired at full power and the second pulse at half power. The time between two pulses was 1.4 ms. For each pulse, RF data was recorded. After subtraction of the scaled half power RF lines from the full power RF lines, the power modulation images resulted. They could be imaged real-time at a frame rate of 5 Hz. A 0.2 mm PVDF needle hydrophone (Precision Acoustics Ltd., Dorchester, UK) verified that the applied powers

corresponded to peak negative pressures ranging from 25 to 250 kPa.

To determine the scatter intensity as a function of acoustic pressure, a region of interest in both the tissue mimicking phantom and the contrast agent suspension was defined. The recorded B-mode images consisted of 258x59 pixels, which corresponded after conversion to a sector scan to a field of view of 8x8 cm. The ROI size was 70x15 pixels. For the programmable ultrasound system, RF data resulted from the recordings, 62 lines divided into 2100 sample points, also corresponding to an image of 8x8 cm. The average amplitude of an ROI of 264x11 sample points was determined.

Table 12.1: Concentrations of the contrast agent suspensions

		BR14			Levovist
	Native	$< 2\ \mu$m	$< 3\ \mu$m	$< 5\ \mu$m	
Concentration [μl/l]	25	250	250	100	250

12.3 Results

For the programmable ultrasound system, the repeatability of the pulses was tested. At the same angle, 4 RF lines were acquired, alternately at half and full power. Figure 12.2 shows RF lines recorded at 250 kPa (full power) and 125 kPa (half power) for the native BR14 suspension. No significant differences between the RF lines recorded at low power, neither between the RF lines recorded at high power are observed. It is however observed that between low and high power the shape of the RF lines changes, which also appears from the frequency domain.

The scales of the scatter intensities recorded by the commercial and programmable ultrasound systems are not the same (Fig 12.3 and 12.4). The commercial ultrasound system recorded the B-mode images 8-bit log-compressed. When transferring this into a linear scale, relatively more weight is given to the brighter intensities, see also Emmer et al. [2007c]. For the programmable ultrasound system, the RF data was recorded in a 12-bit linear scale.

Comparing Fig 12.3 and 12.4, similar results are however observed. The scattering of both the tissue mimicking phantom and Levovist was pressure-independent, which is different from the BR14 suspensions. The native suspension increased 50% from 25 to 250 kPa, but this becomes strikingly more when the average microbubble size of the suspension applied decreases. The suspension with only microbubble sizes smaller than 2.0 μm in diameter increased the most, 560% from 25 to 250 kPa. For this suspension below 90 kPa, the intensities were however below noise level, so for a higher concentration, this difference will be even higher.

To investigate the intensities of the power modulation images, it must be accounted for that the scatter intensity largely depends on microbubble size. For a good compari-

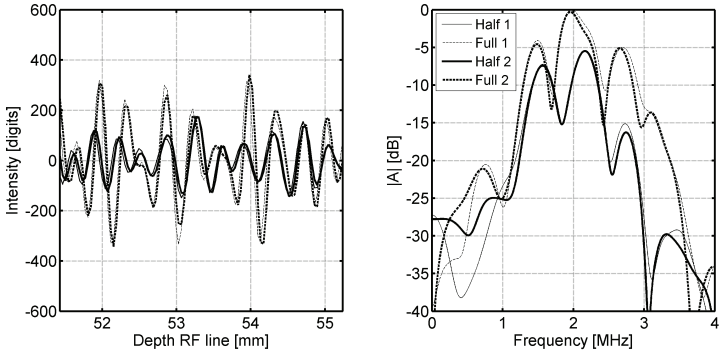

Figure 12.2: RF lines recorded at 250 kPa (full power) and 125 kPa (half power) for the native BR14 suspension. At the same angle, four RF lines were acquired, alternately at half and full power.

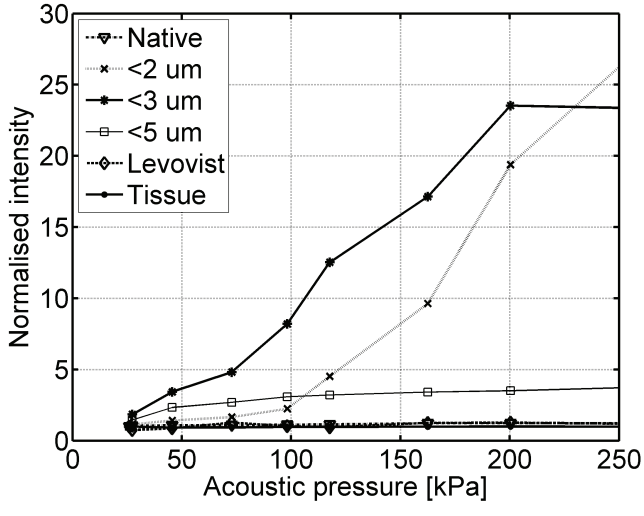

Figure 12.3: Normalised average pixel intensity as a function of acoustic pressure recorded with the commercial ultrasound system.

son, the intensities were compensated for concentration differences by normalising the intensities to the native BR14 intensity recorded at 90 kPa. The normalisation factor was determined by dividing the intensity of the contrast agent suspension at 90 kPa by the intensity of the native BR14 suspension at 90 kPa (Table 12.2). This acoustic pressure

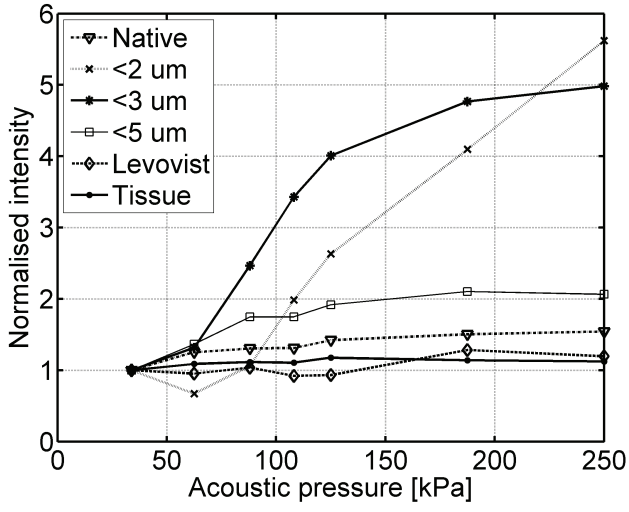

Figure 12.4: Normalised average amplitude intensity of the RF data as a function of acoustic pressure recorded with the programmable ultrasound system.

Table 12.2: Normalisation factor for each suspension

		BR14			Levovist
	Native	$< 2\ \mu$m	$< 3\ \mu$m	$< 5\ \mu$m	
Factor	1	4.5	1.8	1	3

was chosen, because it was the first acoustic pressure where all contrast agent intensities were above the noise level (20 digits).

In the power modulation images recorded by the programmable ultrasound system, the signal from the tissue mimicking phantom was cancelled well (Fig 12.5). A CTR of 20 dB resulted from a power modulation image of native BR14 suspension at 250 kPa. For the filtered suspensions, including the factors of Table 12.2, higher CTR values were observed. For the suspension with microbubble sizes smaller than 2.0 μm in diameter the CTR was 33 dB.

Figure 12.6 shows the intensities of the power modulation images at all acoustic pressures applied (including the factors of Table 12.2). The intensity of the tissue mimicking phantom is at least a factor 2 lower than the intensities of the contrast agent suspensions. Moreover the intensity of tissue in the power modulation image was not pressure-dependent, which is in great contrast to the contrast agent suspensions. The intensities of all contrast agent suspensions were pressure-dependent, but also in the intensities of the

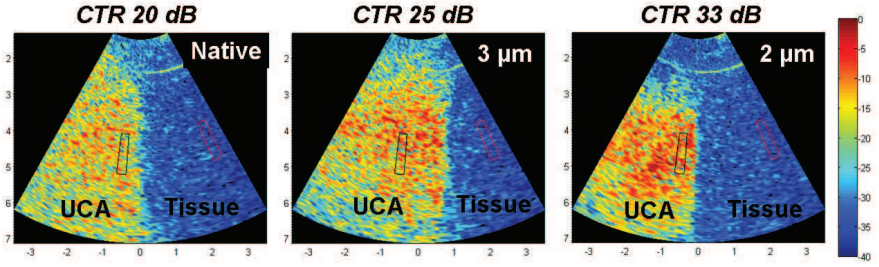

Figure 12.5: Power modulation images of phospholipid-coated contrast agent suspensions (native and filtered, pore size 2.0 and 3.0 μm).

power modulation images it is observed that the filtered suspensions were most pressure-dependent.

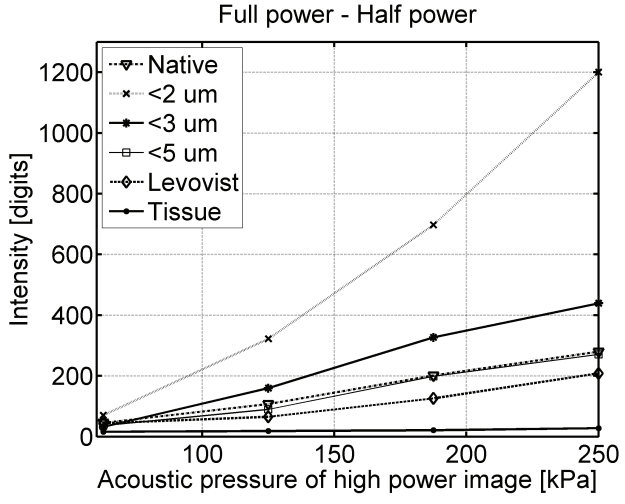

Figure 12.6: Average intensity of the power modulation images. For the power modulation image, the scaled half power RF lines were subtracted from the full power RF lines.

12.4 Discussion

For a phospholipid-coated microbubble suspension with microbubble sizes smaller than 3.0 μm, previous studies [Emmer et al., 2007b] showed strong pressure-dependent scattering. In this study, also filter pore sizes of 2.0 and 5.0 were applied, which showed that

there is an inverse relationship between microbubble size and the slope of the scattering response as a function of acoustic pressure (Fig 12.3 and 12.4). It is hypothesised that pressure-dependent scattering is explained by threshold behaviour. At low acoustic pressures, only a selection of microbubbles oscillates significantly and scatters acoustic energy. When the acoustic pressure is increased, the pressure threshold of more microbubbles is exceeded leading to an increased scattering. Threshold behaviour is typical for phospholipid-coated contrast agents, accordingly no pressure-dependent scattering was found for the "free" contrast agent Levovist.

Figure 12.3 and 12.4 show the effects of threshold behaviour on the scatter intensity as a function of the acoustic pressure. In a power modulation image, not only the amplitude of the signals is important, also the phase of the signals. Amplitude and phase changes between signals may have various causes. In Fig 12.2, no significant differences for RF lines acquired at the same power were observed, which means that the microbubbles did not move and were not significantly destroyed. Between two powers, the signals did however differ. Part of these differences may be explained by threshold behaviour, but in Fig 12.6, also for the native BR14 and Levovist suspensions some pressure-dependent intensity differences are observed. These are likely the result of nonlinear oscillations of the microbubbles and the scattering of energy at the harmonic frequencies. ¿From Fig 12.6, it is however concluded that the effect of threshold behaviour is dominant. Figure 12.5 shows that 13 dB more CTR is obtained using only microbubbles smaller than 2.0 μm instead of a native suspension.

12.5 Conclusions

An inverse relationship between the pressure-dependency of the scattering and microbubble size was measured, which is believed to be an effect of threshold behaviour. This behaviour of smaller phospholipid-coated microbubbles is useful to enhance the contrast in power modulation images. Using a suspension with microbubbles smaller than 2.0 μm, at 2 MHz transmit frequency and an acoustic pressure of 250 kPa, the CTR value was 33 dB, which is 13 dB higher compared to a native BR14 suspension.

Discussion and future perspectives

In this chapter the main findings of this thesis are discussed. The first discussion topic concerns the visualization of the ultrasound harmonic beams by Schlieren imaging. Then, the performances and feasibility of tissue superharmonic imaging are summarized. A third point of discussion describes the use of contrast agents with a new method of harmonic reduction level.

Harmonic schlieren

Several ways are described to measure acoustic beam profiles at the frequencies used in medical ultrasound. The most frequently used method is purely acoustical, and involves the use of an hydrophone. The sensitive element can be as small as 0.04 mm, and is placed in the acoustic field to measure. However, such a small sensitive element must be held, and the housing of any hydrophone is at least 0.3 mm diameter. In the megahertz range, the wavelength is on the order of 1 mm or less and the size of the hydrophone tip needs to be accounted for [Goldstein et al., 1998]. As the frequency of interest increases, as it is the case for the measurement of harmonic beams, the wavelength becomes smaller (already 0.18 mm at 8 MHz). There are alternatives to this kind of invasive measurement of the sound field. Those alternatives consist in optical techniques.

The first optical method uses a LASER vibrometer. Laser vibrometer is of great value in acoustics as it permits the measurement of various phenomena, such as vibration modes of objects or surface displacement of transducers, or the measurement of the acoustic pressure distribution [Harvey and Gachagan, 2006, Wang et al., 2007, Bou Matar et al., 2000]. The main advantage of this acousto optic method is to relate the optical measurement to an absolute value of the acoustic pressure.
Schlieren imaging of sound beam is an acousto optic alternative to LASER vibrometer measurements. Like the previous method, it permits a non invasive measurement of the

acoustic pressure distribution. The ability of such a system to take a snapshot of the acoustic field is specific of Schlieren apparatus. Even if conventional Schlieren methods are not quantitative, it was demonstrated that Schlieren projections of harmonic sound beams is a first step to a quantitative measurement of acoustic pressure field. As described previously described, the pressure amplitude is related to the relative level of harmonics. In respect, harmonic Schlieren is a precious acousto-optic method having the ability to relate the optical measurement of the complete ultrasound beam to an absolute value of the pressure.

Also, the ease to place objects in the water tank and observe the resulting pressure field mirrors a deeper understanding of non linear acoustic methods. Furthermore the combination of such a method with ultrasound contrast agent provides a new investigation tool to study the non linear behavior of microbubbles.

Tissue Superharmonic imaging

The Super harmonic signal in tissue can reach the level of second harmonic. The improvement in lateral and elevation resolution are similar to the third harmonic beam main lobe. Furthermore, no side lobes are visible on a 40 dB dynamic range. The interleaved transducer developed to achieve super harmonic imaging deliver those performances for a fundamental frequency range from 0.7 MHz to 1.3 MHz (chapter 7). The study presented in chapter 8 demonstrates the feasibility of super harmonic imaging with this interleaved array configuration up to a fundamental frequency of 2 MHz. The grating lobes provoked by under sampling the space by such a sparse array have negligible level at super harmonic frequencies for tissue imaging. The benefit of the lower off axis energy brought by second harmonic imaging is also present for the super harmonic beam, with even a thinner beam in lateral and elevation direction.

The axial resolution problem involved by a limited bandwidth of the transmitting array was solved by signal processing techniques described in chapter 9 and 10. The first proposed solution consisted in a dual pulse method. The sum of two consecutive lines fired at two slightly different frequencies cancels out the ripples present in the axial point spread function. This sum is analogous to an interference phenomenon. This method was applied experimentally and improved considerably the axial point spread function without deteriorating the resolution in the other dimensions of space. By using this method, the resulting PSF nearly reaches the axial resolution implied by the transmission of an ideal fundamental short pulse. The obvious disadvantage of such a method is the reduced frame rate it involves, and some ways to fire only one pulse are investigated, such as transmitting the two pulses simultaneously on different parts of the transmitting array.

The second method which was investigated consisted in harmonic chirp compression. The reference chirp used for the correlation was simulated from the KZK equation and included the harmonic 3 to 5. After correlation, the properties of the resulting point spread function offers similar resolution characteristics as the main lobe third harmonic PSF without exhibiting the ripple artifact. However, the improvement in axial resolution is not as dramatic as expected, and is also comparable to the third harmonic axial

resolution. The energy level however is higher than the third harmonic for two reasons :

- the impulsion compression of a chirp longer than a standard short pulse provides more energy into the medium
- the super harmonic signal is integrating the energy of third, fourth and fifth harmonics

For those reasons, super harmonic using chirp compression provides a better compromise penetration/resolution than tissue second harmonic imaging.

Using those materials and methods, Super harmonic is suitable for trans-thoracic applications and trans-abdominal in clinic. Patients difficult to images can benefit from such an imaging modality. Also, it has the potential to be applied for various applications. Echocardiography was the initial target for this new imaging modality. However, its strong potential reaches out for other various applications. For example, clinician lack screening methods for prostate cancer. The current technique using a trans-rectal probe is unpleasant and an alternative could be superharmonic imaging through the bladder. Indeed, the propagation of sound through a full bladder would be beneficial to the harmonic contents of the acoustic pulse. Once the pulse reaches out the prostate region, the amount of harmonics would be much less attenuated than after the same distance in any other tissue. The available harmonic content scattering in the prostate is a valuable source of information for clinicians.

Harmonic imaging and contrast agents

The exploitation of the non linear properties of contrast agents for a better distinction between tissue and bubbles offers a large diversity of methods. Filtering second harmonic signals, or pulse inversion are standard procedures to distinguish signal from bubbles and tissues. One way to further enhance the signals coming from ultrasound contrast agents is to diminish the amount of second harmonic in the transmission beam. A method exploiting short pulse at the second harmonic frequency to bias the second harmonic beam was described chapter 11. The efficiency of this method can lead to an improvement in contrast to tissue ratio of 7.4 dB compared to conventional imaging modalities. There are several advantages of using multiple band reduction of the second harmonic. The first one is that the transmitted recomposed pulse is as short as conventional transmissions bursts. The second consists in the ease of implementing such a method for clinical application : the optimal phase/amplitude of the transmitted signal is tuned to an area of interest by minimizing the backscattered second harmonic signal when no contrast is present. The third is the ability to automate this process, consisting in minimizing the second harmonic backscattered signal.

General conclusion

With the measurement of harmonics beams using Schlieren method, new tool of investigation of non linear sound propagation has been described. The combination of

harmonic Schlieren with the method described relating a distortion measurement to the absolute value of the acoustic pressure provides a new tool to measure the absolute value of the pressure in sound beams.

Subsequently, various methods were describe to control and assess transducer performances. The implementation of trans-oesophageal phased array for newborns illustrates the importance of the control process.

The third part of this thesis is dedicated to a complete description of the solution to perform super harmonic imaging, from the piezo-material choice, to the simulation of the harmonic levels in tissue. The result of this study demonstrates the feasibility of super harmonic imaging. Signal processing techniques were also investigated to permit the improvement of super harmonic point spread function with the current interleaved array transducer. The two methods presented deliver sufficient improvement for the use of super harmonic imaging *in vivo*, for diagnostic ultrasound.

The last part of this thesis proposes methods to enhance contrast-to-tissue-ratio in two different ways. The first method suggests the enhancement of contrast-to-tissue ratio by lowering the second harmonic field generated in tissue. Experimental results show an improvement of 7 dB compared with conventional techniques. The second method suggests the use of filtered solutions of bubbles in order to favor their detection when submitted to a power modulation pulse scheme. This effect is the direct consequence of threshold behavior of ultrasound contrast agents.

References

I. Akiyama, S. Saito, and A. Ohya. Development of an ultra-broadband ultrasonic imaging system: Prototype mechanical sector device. *J. Med. Ultrasonics*, 33(2):71–76, 2006.

D.B. Andropoulus, S.A. Stayer, S.T. Bent, C.J. Campos, and C.D. Fraser. The effects of transesophageal echocardiography on hemodynamic variables in small infants undergoing cardiac surgery. *J. Cardiothorac. Vasc. Anesth.*, 14(2):133–135, 2000.

MA Averkiou, DN Roundhill, and JE Powers. A new imaging technique based on the nonlinear properties of tissues. In *Proc. IEEE Ultrasonic Symp.*, pages 1561–1566, 1997.

N.A. Ayres, W. Miller-Hance, D.A. Fyfe, J.G. Stevenson, D.J. Sahn, L.T. Young, L.L. Minich, T.R. Kimball, T. Geva, F.C. Smith, and J. Rychik. Indications and guidelines for performance of transesophageal echocardiography in the patient with pediatric acquired or congenital heart disease. *J. Am. Soc. Echocardiogr.*, 1:91–98, 2005.

R. Bekeredjian, P.A. Grayburn, and R.V. Shohet. Use of ultrasound contrast agents for gene or drug delivery in cardiovascular medicine. *journal of the american college of cardiology*, 45:329–335, 2005.

E Biagi, L Breschi, E Vannacci, and L Masotti. Stable and transient subharmonic emissions from isolated contrast agent microbubbles. *IEEE Trans. Ultrason. Ferroelect. Freq. Control*, 54(3):480–497, 2007.

D.T. Blackstock. *Fundamental of physical acoustics*. Wiley-Interscience, 2000.

R.J. Bobber. General reciprocity parameter. *J. Acoust. Soc. Am.*, 39(4):680–687, 1966.

J.M.G. Borsboom, C.T. Chin, and N. de Jong. Nonlinear coded excitation method for ultrasound contrast imaging. *Ultrasound Med. Biol.*, 29:277–284, 2003.

J.M.G. Borsboom, A. Bouakaz, and N. de Jong. Pulse subtraction time delay imaging method for ultrasound contrast agent detection. *IEEE transactions on ultrasonics, ferroelectrics, and frequency control*, 56(6):1151–1158, 2009.

Bouakaz A Versluis M de Jong N. Borsboom J, Chin CT. Harmonic chirp imaging method for ultrasound contrast agent. *IEEE Trans. Ultrason., Ferroelectr., Freq. Control.*, 52(2):241–249, 2005.

O. Bou Matar, L. Pizarro, D. Certon, J.P. Remenieras, and F. Patat. Characterization of airborne transducers by optical tomography. *Ultrasonics*, 38:787–793, 2000.

A. Bouakaz and N. de Jong. Native tissue imaging at superharmonic frequencies. *IEEE Trans. Ultrason. Ferroelectr. Freq. Control*, 50(5):496–506, 2003.

A. Bouakaz, N. de Jong, and C. Cachard. Standard properties of ultrasound contrast agents. *Ultrasound in Medicine & Biology*, 24(3):469–472, 1998.

A. Bouakaz, S. Frigstad, F.J. ten Cate, and N. de Jong. Super harmonic imaging: a new imaging technique for improved contrast detection. *Ultrasound Med. Biol.*, 28 (1):59–68, 2002a.

A. Bouakaz, S. Frigstad, FJ Ten Cate, and N. de Jong. Super harmonic imaging: a new imaging technique for improved contrast detection. *Ultrasound Med Biol*, 28(1): 59–68, 2002b.

A. Bouakaz, F.J. ten Cate, and N. de Jong. A new ultrasonic transducer for improved contrast nonlinear imaging. *Phys. Med. Biol.*, 49(16):3515–3525, 2004.

F.P. Branca, F. Bini, and F. Mariozzi. Optimum choice of acoustic properties of filling materials using optical measurement. In *Proc. IEEE Ultrasonic Symp.*, pages 1663–1665, Hawaii, USA, 2004.

G.A. Brock-Fisher, M.D. Poland, and P.G. Rafter. Means for increasing sensitivity in non linear ultrasound imaging systems. *US patent*, (5577505), 1996.

C.J. Bruce, P. OLeary, D.J. Hagler, J.B. Seward, and A.K. Cabalka. Miniaturized transesophageal echocardiography in newborn infants. *J. Am. Soc. Echocardiogr.*, 87:791–797, 2002.

P.N. Burns. Harmonic imaging with ultrasound contrast agents. *Clinical Radiology*, 51 (Suppl.1):50–55, 1996.

A. Caronti, D. Fiasca, G. Caliano, E. Cianci, and M. Pappalardo. Experimental study of acoustic coupling in cmut arrays by optical interferometry. In *Proc. IEEE Ultrasonic Symp.*, pages 1960–1964, Hawaii, USA, 2003.

A. Caronti, A. Savoia, G. Caliano, and M. Pappalardo. Acoustic coupling in capacitive microfabricated ultrasonic transducers: Modeling and experiments. *IEEE Trans. Ultrason. Ferroelectr. Freq. Control*, 52(12):2220–2234, 2005.

C.H. Chen. Ultrasonic and advanced methods for nondestructive testing and material characterization. 2007.

X. Chen and K.Q. Schwarz. Acoustic coupling from a focused transducer to a flat plat and back to the transducer. *J. Acoust. Soc. Am.*, 95(6):3049–3054, 1994.

X. Chen, K.Q. Schwarz, and K.J. Parker. Radiation pattern of a focused transducer: A numerically convergent solution. *J. Acoust. Soc. Am.*, 94(5):2979–2991, 1993.

R.Y. Chiao and L.J. Thomas. Synthetic transmit aperture imaging using orthogonal golay coded excitation. In *Proc. IEEE Ultrasonics Symp.*, pages 1677–1680, 2000.

J Chomas, P Dayton, D May, and K Ferrara. Nondestructive subharmonic imaging. *IEEE Trans. Ultrason. Ferroelect. Freq. Control*, 49(7):883–892, 2002.

P.T. Christopher and K.J. Parker. New approaches to nonlinear diffractive field propagation. *J. Acoust. Soc. Amer.*, 90(1):488–499, 1991.

T. Christopher. Source prebiasing for improved second harmonic bubble-response imaging. *IEEE Trans. Ultrason. Ferroelectr. Freq. Control*, 46(3):556–563, 1999. Journal Article United States.

R.S.C. Cobbold. *Foundations of Biomedical Ultrasound*. Oxford University Press, Inc., Oxford, New York, 2007.

L Couch. *Digital and analog communication systems*. Upper Saddle River. NJ. Prentice Hall Internationnal Editions, 1997.

O Couture, J.F. Aubry, Montaldo G, Tanter M, and Fink M. Suppression of tissue harmonics for pulse-inversion contrast imaging using time reversal. *Physics in Medicine and Biology*, 53(19):5469–5480, 2008.

P. Curie and J. Curie. Contractions et dilatations produites par des tensions électriques dans les cristaux hémièdres à faces inclinées. *Comptes rendus de l'Académie des Sciences*, 93:1137, 1881.

P. Dawson, D.O. Cosgrove, and R.G. Grainger, editors. *Textbook of Contrast Media*. Isis Medical Media Ltd., Oxford, 1999. Williams R. Microbubble dynamics. In:.

N de Jong, R Cornet, and CT. Lancée. Higher harmonics of vibrating gas-filled microspheres. part two: Measurements.

N de Jong, R Cornet, and C.T. Lancée. Higher harmonics of vibrating gas-filled microspheres. part one: Simulation. *Ultrasonics*, 32:447–453, 1994.

N de Jong, P Frinking, A Bouakaz, and F.J. ten Cate. Detection procedures of ultrasound contrast agents. *Ultrasonics*, 38:87–92, 2000.

C.X. Deng, R.H. Lizzi, F.L. Silverman, R. Ursea, and D.J. Coleman. Imaging and spectrum analysis of contrast agents in the in vivo rabbit eye using very-high-frequency ultrasound. *Ultrasound in Medicine and Biology*, 24(3):383–394, 1998.

F.A. Duck. *Physical Properties of Tissues*. Academic Press, Inc, San Diego, 1990.

S Dursun, T Varslot, T Johansen, B Angelsen, and H. Torp. Fast 3d simulation of 2nd harmonic ultrasound field from arbitrary transducer geometries. In *IEEE Ultrasonics Symposium. Sept. 2005.*, volume 4, pages 1964–1967.

A Eller and HG Flynn. Generation of subharmonic of the order one-half by bubbles in a sound field. *J. Acoust. Soc. Am.*, 46(3B):722–727, 1969.

M Emmer. *The onset of bubble vibration*. Ph.d. dissertation, Erasmus Univ. Rotterdam, 2009.

M. Emmer, D. Goertz, A. Van Wamel, M. Versluis, and N. de Jong. Threshold behavior of vibrating microbubbles. In *IEEE ultrasonic symposium*, pages 1545–1547, 2006.

M. Emmer, A. Van Wamel, D. Goertz, and N. de Jong. The onset of microbubble vibration. *Ultrasound Med. Biol.*, 33(6):947–949, 2007a.

M. Emmer, H.J. Vos, D. Goertz, A. Van Wamel, M. Versluis, and N. de Jong. Vibrating microbubbles at low acoustic pressures. In *12th Eur Symp Ultrasound contrast imaging*, page 84, 2007b.

M. Emmer, H.J. Vos, D. Goertz, A. Van Wamel, M. Versluis, and N. de Jong. Clinical relevance of pressure-dependent scattering at low acoustic pressures. *Ultrasonics*, 47 (1-4):74–77, 2007c.

G. Ferin, M. Legros, N. Felix, C. Notard, and L. Ratsimandresey. Ultra-wide bandwidth array for new imaging modalities. In *Proc. IEEE Ultrasonic Symp.*, pages 204–207, New York, USA, 2007.

K Ferrara, R Pollard, and M. Borden. Ultrasound microbubble contrast agents : Fundamentals and application to gene and drug delivery. *Annual Review of Biomedical Engineering*, 9(1):415–447, 2007.

L.L. Foldy and H. Primakoff. A general theory of passive linear electroacoustic transducers and the electroacoustic reciprocity theorem i. *J. Acoust. Soc. Am.*, 17(2):109–120, 1945.

F Forsberg, WT Shi, B Jadidian, and AA Winder. Multi-frequency harmonic arrays: Initial experience with a novel transducer concept for nonlinear contrast imaging. *Ultrasonics*, 43:79–85, 2004.

P Frinking and N. de Jong. Modeling of ultrasound contrast agents. In *IEEE Ultrasonic Symposium. October 1997*, volume 2, pages 1601–1604.

P Frinking, E Gaud, and M Arditit. Compression only behavior and subharmonic scattering of phospholipid-shell microbubbles. In *The 14'th European symposium on ultrasound contrast imaging (abstract)*, pages 80–87, Rotterdam, the Netherlands, 2009.

Caliano G, Carotenuto R, Cianci E, and et al. Design, fabrication and characterization of a capacitive micromachined ultrasonic probe for medical imaging. *IEEE Trans. Ultrason., Ferroelectr., Freq. Control*, 52(12):2259–2269, 2005.

P. Gatta. *Interferometric Characterization of Planar Vibrating Structures*. Ph.d. dissertation (italian), Universitàa Roma Tre, 2008.

R. L. Goldberg, M.J. Jurgens, D.M. Mills, C.S. Henriquez, D. Vaughan, and S.W. Smith. Modeling of piezoelectric multilayer ceramics using finite element analysis. *IEEE Trans. Ultrason. Ferroelectr. Freq. Control*, 44(6):1204–1214, 1997.

A. Goldstein, D.R. Gandhi, and W.D. O'Brien. Diffraction effects in hydrophone measurements. *IEEE Trans. Ultrason. Ferroelectr. Freq. Control*, 45(4):972–979, 1998.

J.W. Goodman. *Introduction To Fourier Optics*. McGraw-Hill Book Co., 2005. ISBN 0-07-024254-2.

J.F. Guess, C.G. Oakley, S.J. Douglas, and R.D. Morgan. Cross-talk paths in array transducers. In *Proc. IEEE Ultrasonic Symp.*, pages 1279–1282, 1995.

M.F. Hamilton and D.T. Blackstock. *Nonlinear acoustics*. Academic Press, Inc., San Diego, California, 1998.

MF Hamilton, JN Tjøtta, and S. Tjøtta. Nonlinear effects in the farfield of a directive sound source. *Ultrasonics*, 78:202–216, 1985.

T.S. Hart and M.F. Hamilton. Nonlinear effects in focused sound beams. *J. Acoust. Soc Am.*, 84(4):1488–1496, 1988.

G. Harvey and A. Gachagan. Noninvasive Field Measurement of Low-Frequency Ultrasonic Transducers Operating in Sealed Vessels. *IEEE transactions on ultrasonics, ferroelectrics, and frequency control*, 53(10):1749–1758, 2006.

J.A. Hossack and B.A. Auld. Improving the characteristics of a transducer using multiple piezoelectric layers. *IEEE Trans. Ultrason. Ferroelectr. Freq. Control*, 40(2):131–139, 1993.

J.A. Hossack, P. Mauchamp, and L. Ratsimandresy. A high bandwidth transducer optimized for harmonic imaging. In *Proc. IEEE Ultrasonic Symp.*, pages 1021–1024, San Juan, Puerto Rico, 2000.

J. Huijssen. *Modeling of Nonlinear Medical Diagnostic Ultrasound*. PhD thesis, Delft University of Technology, 2008.

J Huijssen, MD Verweij, and N de Jong. 3d time-domain modeling of nonlinear medical ultrasound with an iterative greens function method. In *proc. IEEE Ultrasonics symp..*, Vancouver, Canada, 2006.

J Huijssen, MD Verweij, and N. deJong. Comparison of an angular spectrum method and a greens function method for nonlinear propagation of pulsed acoustic fields from medical phased array transducers. In *proc. IEEE Ultrasonics symp.*, New York, USA, 2007.

J. Huijssen, M.D. Verweij, and N. de Jong. Greens function method for modeling nonlinear three-dimensional pulsed acoustic fields in diagnostic ultrasound including tissue-like attenuation. In *proc. IEEE Ultrasonics symp.*, Beijing, China, 2008.

V. F. Humphrey. Nonlinear propagation in ultrasonic fields: measurements modelling and harmonic imaging. *Ultrasonics*, 38:267–272, 2000a.

VF. Humphrey. Nonlinear propagation in ultrasonic fields : measurements, modelling and harmonic imaging. *Ultrasonics*, 38, 2000b.

J.A. Jensen. Field: A program for simulating ultrasound systems. *Paper presented at the 10th Nordic-Baltic Conference on Biomedical Imaging Published in Medical & Biological Engineering & Computing*, 34(Supplement 1 Part 1):351–353, 1996.

J.A. Jensen and N.B. Svendsen. Calculation of pressure field from arbitrarily shaped, apodized and excited ultrasound transducers. *IEEE Trans. Ultrason. Ferroelectr. Freq. Control*, 39(2):262–267, 1992.

M Kameda and Y. Matsumoto. Nonlinear oscillation of a spherical gas bubble in acoustic fields. *Acoustical Society of America*, 106, 1999.

JD Kasprzak, B Paelinck, FJ Ten Cate, WB Vletter, N De Jong, D Poldermans, A Elhendy, A Bouakaz, and Roelandt JRTC. Comparison of native and contrast-enhanced harmonic echocardiography for visualization of left ventricular endocardial border. *Amer. J. Cardiol.*, 83(2):211–217, 1999.

O. Kaya, G.M. Matte, and N. de Jong. Beam profiles visualization of ultrasound harmonics using bandpass schlieren technique. *Delft University of Technology*, 2008.

NA Kharin and GD. Vince. Moderately nonlinear ultrasound propagation in blood-mimicking fluid. *Ultrasound in Medicine & Biology*, 30, 2004.

J Kirkhorn, PJA Frinking, N de Jong, and H. Torp. Three-stage approach to ultrasound contrast detection. *IEEE Trans. Ultrason., Ferroelectr., Freq. Control.*, 48, 2001.

W.R. Klein and B. D Cook. Unified approach to ultrasonic light diffraction. *Sonics, and Ultrasonics, IEEE Transactions on*, SU-14(3):123–134, 1967.

R. Kompfner and R. A. Lemons. Nonlinear acoustic microscopy. *Applied Physics Letters*, 28(6):295–297, 1976.

T. Kondo and M. Kitatuji. Medical transducer arrays using composite materials for acoustic matching layers. In *Proc. IEEE Ultrasonic Symp.*, pages 1318–1321, Montreal, Canada, 2004.

KB Krishnan and KE Thomenius. Improved contrast ultrasound with tissue harmonic minimizing pulse. *IEEE Trans. Ultrason., Ferroelectr., Freq. Control.*, 55, 2008.

S Krishnan, JD Hamilton, and M. O'Donnell. Suppression of propagating second harmonic in non-linear imaging. In *IEEE Ultrasonics Symposium*, volume 2, 1997.

S Krishnan, JD Hamilton, and M. O'Donnell. Suppression of propagating second harmonic in ultrasound contrast imaging. *IEEE Trans. Ultrason., Ferroelectr., Freq. Control*, 45, 1998.

V. Kuznetsov. Equation of nonlinear acoustics. *Sov. Phys. Acoustics*, 16:749–768, 1970.

C. Labuda, J.L. Raymond, and C.C. Church. Reciprocity calibration of hydrophones in the megahertz frequency range. In *Proc. IEEE Ultrasonic Symp.*, pages 1595–1597, 2004.

BJ Landsberger and MF Hamilton. Second-harmonic generation in sound beams reflected from, and transmitted through, immersed elastic solids. *J. Acoust. Soc. Amer*, 109(2):488–500, 2001.

Y.S. Lee. *Numerical solution of the KZK equation for pulsed finite amplitude sound beams in thermoviscous fluids.* Phd-thesis, The University of Texas, 1993.

Y.S. Lee and M.F. Hamilton. Time-domain modeling of pulsed finite-amplitude sound beams. *J. Acoust. Soc. Am.*, 97(2):906–917, 1995.

D.A. Leedom, R. Krimholtz, and G.L. Matthaei. Equivalent circuits for transducers having arbitrary even- or odd-symmetry piezoelectric excitation. *IEEE Trans. Sonics Ultrason.*, SU-18(3):128–141, 1971.

H. Li, Y.C. Li, D. Zhou, J. Peng, H.S. Luo, and J.Y. Dai. Application of pmnpt single crystal in a 3.2 mhz phased-array ultrasonic medical imaging transducer. In *Proc. IEEE Int. Symp. App. Ferroelec.*, pages 572–574, Nara-city, Japan, 2007.

A Lohfink and PC Eccardt. Investigation of nonlinear cmut behavior. In *IEEE Ultrasonics Symposium*, volume 1, pages 585–588, 2005.

A. Lohfink and Eccardt PC. Linear and nonlinear equivalent circuit modeling of cmuts. *IEEE Trans. Ultrason., Ferroelectr., Freq. Control.*, 52(12):2163–2172, 2005.

X. Lurton, editor. *An introduction to underwater acoustics: principles and applications*. Praxis Publishing Ltd, Chichester, UK, 2002.

Q. Ma, D. Zhang, X. Gong, and Y. Ma. Investigation of superharmonic sound propagation and imaging in biological tissues in-vitro. *J. Acoust. Soc. Am.*, 119(4):2518–2523, 2006.

S. E. Masoy, O. Standal, P. Nasholm, T. F. Johansen, and B. Angelsen. Surf imaging: In-vivo demonstration of an ultrasound contrast agent detection technique. *IEEE Trans. Ultrason. Ferroelectr. Freq. Control*, 55(5):1112–1121, 2008. Evaluation Studies Journal Article Research Support, Non-U.S. Gov't United States.

G Matte, PLMJ van Neer, JMG Borsboom, MD Verweij, and N de Jong. A new frequency compounding technique for super harmonic imaging. In *IEEE Ultrasonics Symposium*, pages 357–360, Beijing, China, 2008a. IEEE.

G.M. Matte, J.M.G. Borsboom, P. van Neer, and N. de Jong. Estimating acoustic peak pressure generated by ultrasound transducers from harmonic distortion level measurement. *Ultrasound Med. Biol.*, 34(9):1528–1532, 2008b.

D.D. Mc Lennan, T.D.K NGoc, and W.G. Mayer. Measurement of harmonic profiles of a bounded ultrasonic beam in a liquid medium. *Ultrasonics*, pages 103–106, May .

R.E. McKeighen. Design guildelines for medical ultrasonic arrays. In *Proc. SPIE*, volume 3341, pages 2–18, San Diego, USA, 1998.

R.V. Milani, Y.E. Lavie, C.J. andGilliland, M.M. Cassidy, and J.A. Bernal. Overview of transesophageal echocardiography for the chest physician. *Chest*, 124:1081–1089, 2003.

D.M. Mills. Medical imaging with capacitive micromachined ultrasound transducer (cmut) arrays. In *Proc. IEEE Ultrasonic Symp.*, pages 384–390, Montreal, Canada, 2004.

T. Misardis and J.A. Jensen. Use of modulated excitation signals in medical ultrasound. part ii: design and performance for medical imaging applications. *IEEE Trans. Ultrason. Ferroelectr. Freq. Control*, 52(2):192–207, 2005a.

T. Misardis and J.A. Jensen. Use of modulated excitation signals in medical ultrasound. part i: basic concepts and expected benefits. *IEEE Trans. Ultrason. Ferroelectr. Freq. Control*, 52(2):177–191, 2005b.

R.I. Muhiudeen, W.C. Miller-Hance, and N.H. Silverman. Intraoperative transesophageal echocardiography for pediatric patients with congenital heart disease. *Anesth. Analg.*, 87:1058–1076, 1998.

T. G. Muir and E. L. Carstensen. Prediction of nonlinear acoustic effects at biomedical frequencies and intensities. *Ultrasound Med. Biol.*, 6(4):345–357, 1980.

T. Neumann and H. Ermert. Schlieren visualization of ultrasonic wave fields with high spatial resolution. *Ultrasonics*, 44:1561–1566, 2006.

A Novell, M Legros, N Felix, and A. Bouakaz. Exploitation of capacitive micromachined transducers for nonlinear ultrasound imaging. *IEEE Trans. Ultrason., Ferroelectr., Freq. Control.*, 56(12):2733–2743, 2009.

T.A. Pitts, F. Greenleaf, J. Lu, and R.R. Kinnick. Tomographic Schlieren Imaging for Measurement of Beam Pressure and Intensity. In *IEEE Ultrasonics Symposium*, 1994.

M. Pollakowski and H. Ermert. Chirp signal matching and signal power optimization in pulse-echo mode ultrasonic nondestructive testing. *IEEE Trans. Ultrason. Ferrorelect. Freq. Control*, 41(5):655–659, 1994.

TR Porter, S Li, D Kricsfeld, and RW Armbruster. Detection of myocardial perfusion in multiple echocardiographic windows with one intravenous injection of microbubbles using transient response second harmonic imaging. *J Am Coll Cardiol.*, 29(4):791–799, 1997.

E.G. Radulescu, P.A. Lewin, J. Wojcik, and A. Nowicki. Calibration of ultrasonic hydrophone probes up to 100 mhz using time gating frequency analysis and finite amplitude waves. *Ultrasonics*, 41:247–254, 2003.

M Ramon, G Jorge, and A. Salazar. Detection of nonlinearities caused by bubbles in ultrasonics signals. In *13th European Signal Processing conference*, 2005.

P. W. Rehrig, W.S. Hackenberger, and X. Jiang. Status of piezoelectric single crystal growth for medical transducer applications. In *Proc. IEEE Ultrasonic Symp.*, pages 766–769, Hawaii, USA, 2003.

S.M. Rhim and H. Jung. Piezoelectric single crystal for medical ultrasound transducer. In *Proc. IEEE Ultrasonic Symp.*, pages 300–304, New York, USA, 2007.

S.M. Rhim, H. Jung, J. S. Jun, and J.S. Hwnag. A 6.0 mhz 0.15 mm pitch phased array ultrasonic probe using pmn-pt single crystal. In *Proc. IEEE Ultrasonic Symp.*, pages 219–222, Rotterdam, the Netherlands, 2005.

W.A. Riley and W.R Klein. Piezo-Optic Coefficients of Liquids. *Journal of the acoustical society of America*, 42(6):1258–1261, 1967.

L Schwartz. *Méthodes mathématiques pour les sciences physiques*. Hermann, Paris, France, 1965.

K.Q. Schwarz, X. Chen, S. Steinmetz, and D. Phillips. Harmonic imaging with levovist. *Journal of the American Society of Echocardiography*, 10(1):1–10, 1997.

T.V. Scohy, D.A. Gommers, A.D. ten Harkel, Y. Deryck, J. McGhie, and Bogers A.J. Intraoperative evaluation of micromultiplane transesophageal echocardiographic probe in surgery for congenital heart disease. *Eur. J. Echocardiogr.*, 8:241–246, 2007.

PM Shankar, PD Krishna, and VL. Newhouse. Advantages of subharmonic over second harmonic backscatter for contrast-to-tissue echo enhancement. *Ultrasound in Medicine & Biology*, 24(3):395–399, 1998.

RS Shapiro, J Wagreich, RB Parsons, A Stancato-Pasik, Hsu-Chong Yeh, and R Lao. Tissue harmonic imaging sonography: evaluation of image quality compared with conventional sonography. *AJR*, 171:1203–1206, 1998.

H.H. Shariff, P. Bevan, R. Karshafian, R. Williams, and P.N. Burns. Radial modulation imaging: Raising the frequency for contrast imaging. In *Proc. IEEE Ultrasonic Symp.*, pages 104–107, Vancouver, Canada, 2006.

C-C Shen, Y-C Wang, and Y-C Hsieh. Third harmonic transmit phasing for tissue harmonic generation. *IEEE Trans. Ultrason. Ferroelect. Freq. Control*, 54(7):1370–1381, 2007a.

CC Shen and YC Hsieh. Optimal transmit phasing on tissue background suppression in contrast harmonic imaging. *Ultrasound in Medicine & Biology*, 34(11):1820–1831, 2008.

CC Shen and PC Li. Tissue harmonic image analysis based on spatial covariance. *IEEE Trans. Ultrason., Ferroelectr., Freq. Control.*, 48(6):1648–1656, 2001a.

C.C. Shen and P.C. Li. Harmonic leakage and image quality degradation in tissue harmonic imaging. *IEEE Trans. Ultrason., Ferroelectr., Freq. Control.*, 48(3):728–736, 2001b.

CC Shen and PC Li. Pulse-inversion-based fundamental imaging for contrast detection. *IEEE Trans. Ultrason., Ferroelectr., Freq. Control.*, 50(9):1124–1133, 2003.

CC Shen, YC Wang, and YC Hsieh. A feasibility study of tissue harmonic generation with 3f0 transmit phasing. *IEEE Ultrasonics Symposium*, pages 1748–1751, 2007b.

J. Shen and E.S. Ebbini. A new coded-excitation ultrasound imaging system - part i: basic principles. *IEEE Trans. Ultrason. Ferroelect. Freq. Control*, 43(1):131–140, 1996.

C.H. Sherman and J.L. Butler. *Transducers and arrays for underwater sound*. Springer, 2007. ISBN 978-0-387-32940-6.

S. Sherrit, H.D. Wiederick, and B.K. Mukherjee. A complete characterization of the piezoelectric dieelectric and elastic properties of motorola pzt 3203 hd including losses and dispersion. In *Proc. SPIE*, volume 3037, pages 158–169, Newport Beach, 1997.

W.T. Shi and F Forsberg. Ultrasonic characterization of the nonlinear properties of contrast microbubbles. *Ultrasound Med. Biol.*, 26(1):93–104, 2000.

WT Shi, F Forsberg, JS Raichlen, L Needleman, and BB Goldberg. Pressure dependence of subharmonic signals from contrast microbubbles. *Ultrasound in Medicine & Biology*, 25(2):275–283, 1999.

T Shiota, R Lewandowski, JE Piel, LS Smit, C Lance, and KB et al Djoa. Micromultiplane transesophageal echocardiographic probe for intraoperative study of congenital heart disease in neonates, infants, children, and adults. *Am. J. Card.*, 83:292–295, 1999.

B.A Shrope and V.L. Newhouse. Second harmonic ultrasonic blood perfusion measurement. *Ultrasound in Medicine & Biology*, 19(7):567–79, 1993.

DH Simpson, CT Chin, and PN Burns. Pulse inversion doppler: A new method for detecting nonlinear echoes from microbubble contrast agents. *IEEE Trans. Ultrason., Ferroelectr., Freq. Control.*, 46:372–382, 1999.

E. Sloth, J.M. Hasenkam, KE Sorensen, J Pendersen, KH Olsen, and O.K. et al Hansen. Pediatric multiplane transesophageal echocardiography in congenital heart disease: new possibilities with a miniturized probe. *J Am Soc Echocardiogr*, 9(2):622–628, 1996.

H. C. Starritt, F. A. Duck, A. J. Hawkins, and V. F. Humphrey. The development of harmonic distortion in pulsed finite-amplitude ultrasound passing through liver. *Physics in Medicine and Biology*, 31(12):1401–1409, 1986.

TL Szabo. Time domain wave equations for lossy media obeying a frequency power law. *J. Acoust. Soc. Amer.*, 96(1):491–500, 1994.

Y. Takeuchi. An investigation of a spread energy method for medical ultrasound systems - part one: theory and investigation. *Ultrasonics*, 17(4):175–182, 1979.

M Tanter, JL Thomas, and M. Fink. Time reversal and the inverse filter. *J. Acoust. Soc. Amer.*, 108(1):223–234, 2000.

J.C. Tardif, S.L Schwartz, M.A. Vannan, Q.L. Cao, and N.G. Pandian. Clinical usefulness of multiplane transesophageal echocardiography: comparison to biplanar imaging. *Am. Heart J.*, 128(1):156–166, 1994.

C. Teirlinck, R Bezemer, C Kollmann, and et al. Development of an example flow test object and comparison of five of these test objects, constructed in various laboratories. *Ultrasonics*, 36:653–660, 1998.

JD Thomas and DN Rubin. Tissue harmonic imaging: Why does it work? *Journal of the American Society of Echocardiography*, 11(8):803–808, 1998.

J. N. Tjotta, S. Tjotta, and E. H. Vefring. Propagation and interaction of 2 collinear finite-amplitude sound beams. *Journal of the Acoustical Society of America*, 88(6): 2859–2870, 1990. El603 Times Cited:27 Cited References Count:32.

J. N. Tjotta, S. Tjotta, and E. H. Vefring. Effects of focusing on the nonlinear-interaction between 2 collinear finite-amplitude sound beams. *Journal of the Acoustical Society of America*, 89(3):1017–1027, 1991. Fa701 Times Cited:48 Cited References Count:13.

G. E. Trahey, J. W. Allison, S. W. Smith, and O. T. von Ramm. A quantitative approach to speckle reduction via frequency compounding. *Ultrasonic Imaging*, 8:151–164, 1986.

F Tranquart, N Grenier, V Eder, and L Pourcelot. Clinical use of ultrasound tissue harmonic imaging. *Ultrasound Med. Biol.*, 25(6):889–894, 1999.

V. Uhlendorf and Hoffman C. Nonlinear acoustical response of coated microbubbles in diagnostic ultrasound. *IEEE Ultrasonic Symposium*, 2, 1994.

P. van Neer, M. Danilouchkine, G. Matte, M. Verweij, and N. de Jong. Dual pulse frequency compounded superharmonic imaging for phased array transducers. In *Proc. IEEE Ultrasonic Symp.*, Rome, Italy, 2009a.

P.L.M.J. van Neer, G. Matte, J. Sijl, J.M.G. Borsboom, and N. de Jong. Transfer functions of us transducers for harmonic imaging and bubble responses. *Ultrasonics*, 46(4):336–340, 2007.

P.L.M.J. van Neer, M.G. Danilouchkine, G.M. Matte, M.D. Verweij, and N. de Jong. Dual pulse frequency compounded super harmonic imaging for phased array transducers. In *Proc. IEEE Ultrasonic Symp.*, pages –, Rome, Italy, 2009b.

P.L.M.J. van Neer, G. Matte, M.G. Danilouchkine, C. Prins, F. van den Adel, and N. de Jong. Super harmonic imaging: development of an interleaved phased array transducer. *IEEE Trans. Ultrason. Ferroelectr. Freq. Control*, 57(2):455–468, 2010.

X. Verbeek, L. Ledoux, J. Willigers, P. Brands, and A. Hoeks. Experimental investigation of the pulse inversion technique for imaging ultrasound contrast agents. *J. Acoust. Soc. Amer.*, 107(4):22812290, 2000.

M.D. Verweij and J. Huijssen. A filtered convolution method for the computation of acoustic wave fields in very large spatiotemporal domains. *J. Acoust. Soc Am.*, 125(1): 1868–1878, 2009.

F. Vignon, J.-F. Aubry, M. Tanter, A. Margoum, M.Fink, and J.M. Lecoeur. Dual-arrays brain imaging prototype: Experimental in vitro results. In *Proc. IEEE Ultrasonic Symp.*, pages 504–507, Rotterdam, the Netherlands, 2005.

MM Voormolen. *3D Harmonic Echocardiography*. PhD thesis, Erasmus University Rotterdam, 2007.

W. F. Walker and G. E. Trahey. The application of k-space in medical ultrasound. *IEEE Transactions on Ultrasonics, Ferroelectrics and Frequency Control*, 45:541–558, 1998.

Y. Wang, J. Tyrer, P. Zhihong, and W. Shiquan. Measurement of focused ultrasonic fields using a scanning laser vibrometer. *Journal of the acoustical society of America*, 121 (5):2621–1261, 2007.

B Ward, AC Baker, and VF Humphrey. Nonlinear propagation applied to the improvement of resolution in diagnostic medical ultrasound. *J. Acoust. Soc. Am.*, 101(1): 143–154, 1996.

K. Wear. The effects of frequency-dependent attenuation and dispersion on sound speed measurements: applications in human trabecular bone. *IEEE Trans. Ultrason., Ferroelectr., Freq. Control.*, 47(1):265–273, 2000.

X. Yang and R. Cleveland. Time domain simulation of nonlinear acoustic beams generated by rectangular pistons with application to harmonic imaging. *J. Acoust. Soc. Amer.*, 117:113–123, 2005.

G. G. Yaralioglu, B. Bayram, and B.T. Khuri-Yakub. Finite element analysis of cmuts: Conventional vs. collapse operation modes. In *Proc. IEEE Ultrasonic Symp.*, pages 586–589, Vancouver, Canada, 2006.

C.K. Yeh, S.Y. Su, C.C. Shen, and M.L Li. Dual high-frequency difference excitation for contrast detection. *IEEE Trans. Ultrason., Ferroelectr., Freq. Control.*, 55(10): 2164–2176, 2008.

M. Yumoto and H. Katsuya. Transesophageal echocardiography for cardiac surgery in children. *J Cardiothorac Vasc Anesth*, 16(5):587–591, 2002.

K.Y. Yvorchuk, R.A. Sochowski, and K.L. Chan. A prospective comparison of the multiplane probe with the biplane probe in structure visualization and doppler examination during transesophageal echocardiography. *J Am Soc Echocardiogr*, 8(2):111–120, 1995.

E Zabolotskaya and R. Khokhlov. Quasi-plane waves in the nonlinear acoustics of confined beams. *Sov. Phys, Acoustics*.

C.I Zanelli and M.M. Kadri. Measurements of acoustic pressure in the non linear range in water using quantitative schlieren. In *IEEE Ultrasonics Symposium*, 1994.

R.J. Zemp, J. Tavakkoli, and R.S.C Cobbold. Modeling of nonlinear ultrasound propagation in tissue from array transducers. *J. Acoust. Soc. Amer.*, 113(1):139–152, 2003.

S. Zhou and J.A. Hossack. Investigation of digital filtering for stacked, phased ultrasound transducers. In *Proc. IEEE Ultrasonic Symp.*, pages 1201–1204, Munich, Germany, 2002.

S. Zhou, P. Reynolds, and J.A. Hossack. Improving the performance of capacitive micromachined ultrasound transducers using modified membrane and support structures. In *Proc. IEEE Ultrasonic Symp.*, pages 1925–1928, Rotterdam, the Netherlands, 2005.

M.J. Zipparo, C.G. Oakley, D.M. Mills, A.M. Dentinger, and L.S. Smith. A multirow single crystal phased array for wideband ultrasound imaging. In *Proc. IEEE Ultrasonic Symp.*, pages 1025–1029, Montreal, Cananda, 2004.

Summary

Ultrasound imaging is of daily use in the clinic for various applications. It is an inexpensive method which provides an accurate diagnoses tool under optimal conditions. However, in some cases, this method has difficulties imaging areas of interests in some cases, mostly if the acoustic path is underestimated or if the acoustic window is too narrow. For instance, with trans-thoracic applications, ribs may induce spurious reverberations which degrade the echographic image. These acoustic problems started to be circumvented with the appearance of tissue harmonic imaging in the late nineties. Conventional ultrasound imaging consists in detecting the backscattered signal along the path of the transmitted acoustic wave. Second harmonic imaging exploits part of the distortion of the incident wave to record finer details. Such improvements imply important technological progress to build more efficient and sensitive acoustic sensors on a wider frequency band. Those sensors, or transducers, are the part of the imaging system which convert an electrical signal to an acoustic wave and inversely.

The aim of this thesis is to provide new tools and methodology to measure acoustic pressure distribution, characterize transducers, and propose imaging techniques that will contribute to improving the performance of current echographic systems used in medical applications.

The first part of this thesis explores measurement methods of the acoustic pressure distribution. Building equipment for diagnosis ultrasound necessitates defining the efficiency and sensitivity of transducers. This measurement is only possible by knowing the absolute value of the pressure generated by transducers. The most common way to assess the absolute value of the pressure is described chapter 2, in which the intrinsic properties of the propagation of ultrasound in water can be exploited to measure the absolute value of the acoustic pressure. In this chapter, a method is described to extract

the absolute value of the pressure by comparing the measured harmonic distortion of an acoustic wave with simulations. The principle of the measurement method was tested using several transducers. The acoustic waves were simulated by solving the KZK non linear wave equation generated from axi-symmetrical transducers. Using this method, the acoustic pressure was determined within 20% of the calibrated hydrophone measurement.

Medical ultrasound imaging also requires strict control of the beam profiles generated by ultrasound transducers. Schlieren imaging provides a valuable tool to measure ultrasound harmonics in the Megahertz range. Chapter 3 describes how to measure harmonic beam profiles with this acousto-optic method. Good agreement was achieved between the Schlieren acquisitions and the numerical simulations obtained by solving the KZK wave equation.

The second part of this thesis focus on the characterization of ultrasound transducers. Chapter 4 is dedicated to the definition of measurement protocols that characterize transducers transfer functions through several methods. The next chapter is a comparative study of numerical simulation of surface vibrations of a phased array element with interferometer measurements in air. A good agreement was achieved between finite element model and the vibrometer measurements. This study is followed by a direct application of the transducer development. It presents the design and realization of a small trans-esophageal phased array probe for newborns. Thus a close collaboration between clinicians and transducer manufacturers leads to useful tools for cardiology.

The third part of this thesis is dedicated to ultrasound super harmonic imaging, a concept which was introduced by [Bouakaz et al., 2002b]. The target application of this study was echocardiography. According to this study, the acoustic intensity available in the third to fifth harmonics would reach similar amplitudes as the second harmonic level. Furthermore, the compromise between penetration and resolution would be again improved. The main difficulty is to build a phased array transducer with a sufficient bandwidth able to transmit with a sufficient amplitude. Also, it must detect multiple harmonics with a sufficient sensitivity. From this point, chapter 7 describes a strategy to fulfill the bandwidth requirements of such an exigent method. The proposed solution consists in separating the frequency bands of the transmitters and receivers , and alternately placing them along the array. The detailed piezomaterial selection is also depicted in this chapter. Since other possibilities exist in the topology of the array itself, the next chapter is dedicated to the optimization of the array configuration, as well as the transmitting frequency for transthoracic and abdominal applications. Images produced experimentally exhibit the consequences of an irregular point spread function. This problem was the consequence of the limited bandwidth of the transmitter. Signal processing techniques are described in chapters 9 and 10, to circumvent this problem. The first technique consists in a dual pulse method to fill the troughs present in the spectrum. The second would be to use chirp compression. Both methods permit to recover a good axial

resolution. Those two methods presents different performances.

The last part of this thesis propose methods to enhance the signal from ultrasound contrast agents. Ultrasound contrast agents consist of fluids with coated gas filled microbubbles, which are introduced in the body by an intravenous injection. Their response to ultrasound is strongly non linear. When exposed to ultrasound, the intense production of harmonics from microbubbles permits their differentiation from tissue, which behaves more linearly. Two methods are described in order to further enhance the contrast to tissue ratio. The first one, consists in reducing the second harmonic generated by the propagation of the acoustic wave through tissue, using source pre-biasing technique on a wide frequency band. Improvement of contrast to tissue ratio yields to 7.4 dB under the described experimental conditions. The second technique exploits the threshold behavior of filtered solution of microbubbles. By applying a power modulation scheme on a population of 2 μm diameter bubbles, the improvement of contrast to tissue ratio is improved by 13 dB compared to the native suspension of microbubbles.

Samenvatting

In het ziekenhuis wordt echografie dagelijks gebruikt voor verschillende doeleinden. Onder de optimale omstandigheden is het een goedkope, accurate methode voor het stellen van diagnoses. Niet te min heeft deze methode moeilijkheden met het weergeven van bepaalde locaties in het menselijk lichaam, meestal in het geval van een onderschatting van het akoestische traject of wanneer het akoestische kader te smal is. In het geval van een trans-thoraxale toepassing bijvoorbeeld kunnen de ribben een verstoorde weerkaatsing veroorzaken, met een mindere kwaliteit foto als gevolg. Deze akoestische problemen werden verholpen door de harmonische beeldvorming techniek die ontwikkeld werd in de late jaren 90. De conventionele ultrageluid beeldvoorming detecteert de weerkaatste signalen van de uitgestoten geluidsgolf. Tweede Harmonische beeldvorming onderzoekt daarnaast een deel van de verstoorde weerkaatste geluidsgolven voor het opbouwen van meer detail in de foto en doet hierdoor deels de verstoring te niet. Deze vooruitgang vereiste een verdere technologische ontwikkeling van meer efficiente en gevoelige akoestische sensoren met een ruime frequentie bandbreedte. Deze sensoren, of transducenten, zijn onderdelen van de beeldvormende systemen die elektronische signalen omzetten in akoestische golven en vise versa.

Het doel van dit proefschrift is het leveren van gereedschap en methoden voor het meten van akoestische drukdistributie, het karateriseren van transducenten, en het opperen van beeldvormende technieken die meewerken om de prestaties van de huidige echografische systemen binnen het medische werkgebied te verbeteren.

Het eerste gedeelte van dit proefschrift behandelt meet methoden van de akoestische drukdistributie. Een belangrijk onderdeel van de techische opzet voor ultrageluid beeldvoorming is het definieren van de de efficientie en gevoeligheid van de transducenten. Deze meting is alleen mogelijk doormiddel van het determineren van de absolute waarde van de akoestische druk die geleverd wordt door de transducent.

Een mogelijke determinatie van de absolute waarde van de druk wordt beschreven

in hoofdstuk 2, waarbij de intrinsieke waarde van de voortvloeiende echo in water gebruikt wordt voor het meten van de absolute waarde van de akoestische druk. Een andere methode, die ook wordt beschreven, is door het vergelijken van de gemeten harmonische verstoring van een akoestische golf door middel van simulatie. Het principe van de tweede meeting methode is getest met verscheidene transducenten. De akoestische golven werden gesimuleerd door het oplossen van de KZK-vergelijking die geproduceerd werd door de cilindrische transducenten. Door het gebruik van deze methode werd de akoestische druk gedetermineerd binnen 20% van de gekalibreerde hydrofoon meting.

Een ander cruciaal onderdeel van ultrageluid beeldvorming is de controle over het profiel van de bundel afkomstig van de ultrageluid transducenten. Schlieren Imaging is een goede manier voor het meten van ultrageluid harmonien binnen de Megahertz breedte. Hoofdstuk 3 beschrijft hoe de harmonische profielbundels te meten zijn door middel van deze akoestisch-optische methode. Goede resultaten zijn geboekt door het vergelijken van de Schlieren gegevens met de numerieke simulaties verkregen door het oplossen van de KZK golf vergelijking.

Het optimaliseren van de transducenten is een essentieel onderdeel van de ultrageluid beeldvoorming Het tweede gedeelte van dit proefschrift gaat dan ook over de karakterisering van de ultrageluid tranducenten.

In hoofdstuk 4 worden verschillende metingsprotocollen voor de transducenten responsie beschreven. In het daarop volgende hoofdstuk wordt er een vergelijkende studie gemaakt van oppervlak vibraties van de phased array element met behulp van numerieke simulatie elementen afkomstig van interferometer metingen. De studie met numerieke simulatie en de vibrometer metingen hebben geleidt tot goede resultaten. De studie wordt gevolgd door een directe toepassing van deze eerder beschreven transducent. Het laat de ontwikkeling en realisatie zien van een kleine transesophagale echografie phased array transducenten voor babies. Het is een duidelijke demonstratie dat een nauwe, succesvolle samenwerking tussen clinici en de fabrikanten van transducenten kan leiden tot gebruiksvriendelijk gereedschap voor cardiologie.

Het derde gedeelte van het proefschrift gaat over ultraguid super harmonische beeldvorming, een concept ontwkkeld door [Bouakaz et al., 2002b]. Het doel van deze studie was een toepassing binnen de echocardiologie. Volgens de bevindingen bereikt de akoestische intensiteit die beschikbaar is in de derde en vijfde harmonie dezelfde amplituden als in het tweede harmonische veld. Verder is de gecomprimeerde penetratie tegenover de resolutie opnieuw verbeterd.

Het grootste probleem is het bouwen van een phased array met genoeg bandbreedte die met voldoende amplitude kan zenden. Hij moet ook meerdere harmonien met voldoende gevoeligheid kunnen ontvangen. Vanuit dat oogpunt wordt in hoofdstuk 7 een strategie beschreven hoe aan deze veeleisende methode van de benodigde bandbreedte te voldoen. De voorgestelde oplossing bestaat uit het loskoppelen van de zenders en frequentie bandbreedte ontvangers en om ze om en om langs het pad van de P.A. te plaatsen.

De gedetaileerde Piezomateriaal selectie wordt ook weergegeven in dit hoofdstuk. Sinds er andere topologische vormen bestaan van de serie opstelling, beschrijft het volgende hoofdstuk de optimalisering van de serie configuratie en ook de verzend frequentie van trans-thoracic en abdominale toepassing. De gemaakte fotos laten soms de gevolgen zien van een onregelmatige point spread function. Dit probleem was het gevolg van de gelimiteerde bandbreedte van de zenders. Signaal behandelings technieken worden beschreven in hoofdstuk 9 en 10, om een oplossing te bieden voor dit probleem. De eerste techniek bestaat uit een dubbele puls methode om de gaten te vullen die in het spectrum ontstaan. De tweede oplossing zou de toepassing kunnen zijn van de tjilp compressie. Met beide methoden verkrijgen we een goede as-resolutie. De twee methoden laten verschillende resultaten zien.

Het laatste gedeelte van het proefschrift stelt een aantal methoden voor om de signalen van de microbelletjes te versterken. De microbelletjes bestaat uit een vloeistof met gecoate gasgevulde microbelletjes die in het lichaam worden ingebracht via een aderinjectie. De reactie van de microbelletjes op het ultrageluid is sterk niet-linear. Onder blootstelling van ultrageluid zorgt de intense productie van harmonien afkomstig van de microbelletjes voor een duidelijke onderscheiding van weefsel, dat juist meer linear reageert. Twee methoden worden hierna beschreven om het contrast tussen de microbelletjes en het weefsel verder te vergoten. De eerste bestaat uit het verminderen van de tweede harmonie afkomstig van de voortbeweging van de akoestische golf door het weefsel door het gebruik van een bron pre-biasing techniek met een brede frequentie. De verbetering van het contrast kan oplopen tot 7.4 dB onder de beschreven experimentele condities. De tweede techniek onderzoekt het drempel gedrag van de gefilterde uitkomst van de microbelletjes. Door het toepassen van een power modulation scheme op de belletjes van 2 micrometer in diameter, de verbetering van het constrast wordt verbeterd tot 13 dB in vergelijing tot de normale reactie van microbelletjes.

Dankwoord

Thanks to the efforts of the Lab of Biomedical engineering (experimentele echocardiografie) to encourage young foreign engineers to pursue their interest in biomedical research in an outstanding environment. Thanks to Nico and Ton to let me participate in this adventure.
Thanks to Paul, my direct teammate. Paul, it was fun to work with you. I enjoyed the long and sometimes emotional debates we had, to finally conclude that we were saying the same thing !
Thanks to Mike, (and Paul again) who helped me re-writting articles over and over. Structural changes, grammatical changes, typos etc.. This Dankwoord is probably a good example of what my co-authors have been through. Mike, thanks for your patience, support, help, soups and fruits.
I have great memories of the usual warm lunch fellows and the eccentric conversations on everything, including weird scientific experiments. Thanks to you guys.
From the beginning of my stay in Rotterdam : Thanks to Henri Baartmans and Klaas Bom and Egon my tutor during my master's project. Thanks to Marcia, Gijs and Robert for the music, Rik, Klazina, Miranda, Xavier the founder of the controversial french trench, Frederic, official driver of the Fietscaf. Thanks to Marie, for letting me scan her liver. Thanks to Mirza, official terror of the lab equipment, Hans 1, Esther, Hans 2, Cees, Marco. Thanks to the endless patience of Mieke. Thanks to the electronic support, Robert and Ian, fixing up the things we blow up. Thanks to the wise and experienced Charles. Also thank to Wim, Geert, Leo and the people from the 22nd floor. Thanks to Ozgur, who made a great job on this exciting project of Schlieren imaging.
Thanks to Oldelft, Christian, Frank, Ruud, Rob. Thanks to the theoretical team from TU Delft, Koos, Martin. Thanks to Paul Boontje and Yvette Roman from STW. Thanks to the university of Roma III, especially Philippe Gatta, for the interferometer measurements. Thanks to Thierry Scohy, for the TEE for newborns study. Thanks to Tanya and

Arend for the help concerning the English and Dutch writing. Thanks to the ones i forgot to thank. And sorry for the names i did not spell right. To you all, I hope we will work together again in the future.

Finally, thanks to my parents for their unconditional love and support.

About the author

Guillaume M. Matte was born in Martigues, France on the september 29, 1982. He studied Biomedical engineering at the ”Ecole Supérieure d’Ingénieurs de Luminy” (ESIL), in Marseille. His last year internship took place at the laboratory of experimental echocardiography of Erasmus Medical Center (Rotterdam, the Netherlands), where he worked to assess the safe use of harmonic measurement of the bladder volume. He obtained his Master of science degree in 2006. After his graduation he was detached by the Interuniversity Cardiology Institute of the Netherlands (ICIN, KNAW) at the Erasmus Medical Center in Rotterdam. There he joined the department of Biomedical engineering at the Thoraxcenter to pursue his PhD degree under the supervision of Nico de Jong and Ton van der Steen. His researches focused on transducer design, measurements methods and signal processing for non linear imaging techniques. He left the Netherlands in september 2008, to work on underwater acoustics at IXSEA in La Ciotat (France), as an acoustic engineer.

List of publications

Papers in preparation

G.M. Matte, P.L.M.J. van Neer, M.G. Danilouchkine, J. Huijssen, M. Verweij, N. de Jong, Parameter optimization of a super harmonic phased array transducer for transthoracic applications, submitted to IEEE transactions on UFFC.

P.L.M.J. van Neer, M.G. Danilouchkine, **G.M. Matte**, N. de Jong, Dual pulse method for super harmonic imaging, in preparation.

G.M. Matte, O. Kaya, G. van Soest, N. de Jong, Schlieren imaging of ultrasound harmonics, in preparation.

Peer-reviewed articles

P.L.M.J. van Neer, **G. Matte**, M.G. Danilouchkine, C. Prins, F. van den Adel, N. de Jong, Superharmonic imaging: development of an interleaved phased-array transducer, *IEEE Trans. Ultrason. Ferroelectr. Freq. Control*, 57(2):455-468, 2010.

T.V. Schohy, **G. Matte**, P.L.M.J. van Neer, A.F.W. van der Steen, J. McGhie, A. Bogers, N. de Jong, A new transesophageal probe for newborns, *Ultrasound Med. Biol.*, 35(10):1686-1689, 2009.

G.M. Matte, J.M.G. Borsboom, P. van Neer, N. de Jong, Estimating acoustic peak pressure generated by ultrasound transducers from harmonic distortion level measurement, *Ultrasound Med. Biol.*, 34(9):1528-1532, 2008.

P.L.M.J. van Neer, **G. Matte**, J. Sijl, J.M.G. Borsboom, N. de Jong, Transfer functions of US transducers for harmonic imaging and bubble responses, *Ultrasonics*, 46:336-340, 2007.

M. Pasovic, M. Danilouchkine, **G. M. Matte**, A. F. W. van der Steen, O. Basset, N. de Jong, C. Cachard, Multiple component second harmonic reduction signal, for reducing a broad 2^{nd} harmonic band of the propagating ultrasound wave, *Ultrasound Med. Biol.*, March 2010.

Conference proceedings

P. L. M. J. van Neer, M. G. Danilouchkine, **G. M. Matte** ,M. D. Verweij, N. de Jong, Feasibility study of superharmonic imaging using chirps, *J. Acoust. Soc. Am. Volume 127, Issue 3, pp. 1730-1730 (March 2010).*

P.L.M.J. van Neer, M.G. Danilouchkine, **G.M. Matte**, M.D. Verweij, N. de Jong, Dual pulse frequency compounded super harmonic imaging for phased array transducers, *Proc. IEEE Ultrasonics Symp., Rome, Italy*, 2009.

M. Pasovic , C. Cachard, **G. Matte**, A. Van Der Steen, N. De Jong, O. Basset Adjusting the phase of the signals transmitted from dual frequency probe for reducing second harmonic during propagation, *J. Acoust. Soc. Am., Vol. 123, No. 5, Pt. 2, May 2008* (Acoustics Paris 2008)

G.M. Matte, P.L.M.J. van Neer, J.M.G. Borsboom, M.D. Verweij, N. de Jong, A new frequency compounding technique for super harmonic imaging, *Proc. IEEE Ultrasonics Symp., Beijing, China*, 357-361, 2008.

P.L.M.J. van Neer, **G. Matte**, P. Gatta, M. Pappalardo, N. de Jong, A comparison of array element surface vibration calculated by finite element modelling and laser interferometer measurements, *Proc. IEEE Ultrasonics Symp., Beijing, China*, 788-791, 2008.

M. Pasovic, O. Basset, **G. M. Matte**, A. F.W. van der Steen, N. de Jong, C. Cachard, Influence of the transducer geometry on the phase of the signal used for reducing second harmonic during ultrasound propagation. *IEEE UFFC beijing 2008*

Pasovic M, **Matte G**, van der Steen AF, Basset O, de Jong N, Cachard C., Preliminary investigation of nonlinear dual frequency mixing technique for the estimation of the nonlinear parameter B/A., *Conf Proc IEEE Eng Med Biol Soc.*, 2007, pp 2179-82.

M. Emmer, **G. Matte**, P. van Neer, A. van Wamel, N. de Jong. Improved ultrasound contrast agent detection in a clinical setting. *Proc. IEEE Ultrasonics Symp., New York, NY, USA*, 2235-2238, 2007.

P.L.M.J. van Neer, **G. Matte**, J.M.G. Borsboom, M.D. Verweij, N. de Jong, Development of a phased array for tissue and contrast super harmonic imaging. *Proc. IEEE Ultrasonics Symp., New York, NY, USA*, 200-203, 2007.

P.L.M.J. van Neer, **G. Matte**, J. Sijl, J.M.G. Borsboom, N. de Jong, Transfer functions of US transducers for harmonic imaging and bubble responses, *Proc. International Congress on Ultrasonics, Vienna, Austria*, 2007.

Matte, G.M. Borsboom, J. Verweij, M.D. de Jong, N., Acoustic Wave Amplitude Estimation Based on Harmonic Distortion in Water *Proc. IEEE Ultrasonics Symposium, Vancouver, Canada*, 2006, pp 1718 - 1721

PhD portfolio

Name PhD Student: Guillaume Matte	PhD period: September 2006 - November 2010
Erasmus MC Dep.: Biomed. Engineering	Promotors: N. de Jong/A.F.W. van der Steen
Research School: Coeur	

Courses	Year	ECTS
Biomedical English writing and communication (NIHES)	2008	4
Medical Imaging - 1, Principles, ultrasound and magnetic resonance, (ESMP, Archamps, France)	2006	1.5

International conferences	Year	ECTS
The fifteenth European Symposium on Ultrasound Imaging (Rotterdam, the Netherlands)	2010	0.6
IEEE International Ultrasonics Symposium (Rome, Italy)	2009	0.9
The fourteenth European Symposium on Ultrasound Imaging (Rotterdam, the Netherlands)	2009	0.6
IEEE International Ultrasonics Symposium (Beijing, China)	2008	0.9

International conferences (continued)	Year	ECTS
The thirteenth European Symposium on Ultrasound Imaging (Rotterdam, the Netherlands)	2008	0.6
IEEE International Ultrasonics Symposium (New York, NY, USA)	2007	0.9
14'th New England Doppler Conference (Maastricht, the Netherlands)	2007	1.2
International Congress on Ultrasonics (Vienna, Austria)	2007	1.2
IEEE International Ultrasonics Symposium (Vancouver, Canada)	2006	0.9
The twelfth European Symposium on Ultrasound Imaging (Rotterdam, the Netherlands)	2007	0.6
The eleventh European Symposium on Ultrasound Imaging (Rotterdam, the Netherlands)	2006	0.6

Seminars and workshops	Year	ECTS
Nonlinear Acoustics and Harmonic Imaging (IEEE course, Rotterdam, the Netherlands)	2006	0.15
Medical Ultrasound Transducers (IEEE course, Rotterdam, the Netherlands)	2006	0.15
Photoacoustic Imaging and Sensing (IEEE course, New York, USA)	2007	0.15
Estimation and Imaging of Tissue Motion and Blood Velocity (IEEE course, New York, USA)	2007	0.15
Ultrasound Imaging Systems: from Principles to Implementation (IEEE course, New York, USA)	2007	0.15

Supervising activities	Year	ECTS
Master project (7 months)	2008	4.5